

F/G 1/3

N62269-78-C-0036

NL

△: 凡

The image displays a 16x16 grid of 256 small, dark, square images. These squares are arranged in a uniform pattern, suggesting a low-resolution scan of a document page. The top-left corner of the grid shows some variation, with a few squares appearing slightly lighter or darker than the others, possibly indicating the header area or a scanning artifact. The overall appearance is that of a dense, pixelated representation of a document page.

AD A103272

LEVEL



Report No.: NAC-7711

①

no tabbing

PREDICTION METHODOLOGY FOR PROPULSIVE INDUCED  
FORCES AND MOMENTS OF V/STOL AIRCRAFT  
IN TRANSITION/STOL FLIGHT

VOLUME I TECHNICAL DISCUSSION

BY

T. D. BEATTY AND S. S. KRESS

VOUGHT CORPORATION  
P. O. BOX 225907  
DALLAS, TEXAS 75222

DTIC

AUG 24 1981

H

31 JULY 1979

FINAL REPORT FOR PERIOD 29 NOVEMBER 1977 - 30 JULY 1979

APPROVED FOR PUBLIC RELEASE - DISTRIBUTION UNLIMITED

PREPARED FOR

NAVAL AIR DEVELOPMENT CENTER  
WARMINSTER, PENNSYLVANIA 18974

DTIC FILE COPY

81 8 21 03

## NOTICES

**REPORT NUMBERING SYSTEM** - The numbering of technical project reports issued by the Naval Air Development Center is arranged for specific identification purposes. Each number consists of the Center acronym, the calendar year in which the number was assigned, the sequence number of the report within the specific calendar year, and the official 2-digit correspondence code of the Command Office or the Functional Directorate responsible for the report. For example: Report No. NADC-78015-20 indicates the fifteenth Center report for the year 1978, and prepared by the Systems Directorate. The numerical codes are as follows:

CODE	OFFICE OR DIRECTORATE
00	Commander, Naval Air Development Center
01	Technical Director, Naval Air Development Center
02	Comptroller
10	Directorate Command Projects
20	Systems Directorate
30	Sensors & Avionics Technology Directorate
40	Communication & Navigation Technology Directorate
50	Software Computer Directorate
60	Aircraft & Crew Systems Technology Directorate
70	Planning Assessment Resources
80	Engineering Support Group

**PRODUCT ENDORSEMENT** - The discussion or instructions concerning commercial products herein do not constitute an endorsement by the Government nor do they convey or imply the license or right to use such products.

APPROVED BY:

Edward J. Sturm

DATE:

3-11-80

Unclassified

SECURITY CLASSIFICATION OF THIS PAGE (When Data Entered)

14 REPORT DOCUMENTATION PAGE		READ INSTRUCTIONS BEFORE COMPLETING FORM
1. REPORT NUMBER NADC 77119-30	2. GOVT ACCESSION NO. AD-A103272	3. RECIPIENT'S CATALOG NUMBER
4. TITLE (and Subtitle) Prediction Methodology for Propulsive Induced Forces and Moments in Transition/STOL Flight Volume 1. Technical Discussions		5. TYPE OF REPORT & PERIOD COVERED Final NOV 1977-JUL 1979
7. AUTHOR(s) T. D. Beatty S. S. Kress		6. PERFORMING ORG. REPORT NUMBER
9. PERFORMING ORGANIZATION NAME AND ADDRESS Vought Corporation P. O. Box 225907 Dallas, Texas 75222		8. CONTRACT OR GRANT NUMBER(s) N62269-78-C-0036
11. CONTROLLING OFFICE NAME AND ADDRESS Naval Air Development Center Warminster, PA 18974		10. PROGRAM ELEMENT, PROJECT, TASK AREA & WORK UNIT NUMBERS 12 63
14. MONITORING AGENCY NAME & ADDRESS (if different from Controlling Office)		12. REPORT DATE Jul 1979
		13. NUMBER OF PAGES 179
		15. SECURITY CLASS. (of this report) Unclassified
		13a. DECLASSIFICATION/DOWNGRADING SCHEDULE
16. DISTRIBUTION STATEMENT (of this Report)  Approved for public release. Distribution unlimited.		
17. DISTRIBUTION STATEMENT (of the abstract entered in Block 20, if different from Report)		
18. SUPPLEMENTARY NOTES		
19. KEY WORDS (Continue on reverse side if necessary and identify by block number) V/STOL Transition V/STOL Jet Effects V/STOL Inlet Effects		
20. ABSTRACT (Continue on reverse side if necessary and identify by block number)  A computerized prediction method for propulsive induced forces and moments in transition and short takeoff and landing (STOL) flight has been developed for the Naval Air Development Center (NADC). The method developed was based on the Vought V/STOL aircraft propulsive effects computer program (VAPE).  (over)		

DD FORM 1473

EDITION OF 1 NOV 68 IS OBSOLETE  
S/N 0102-LF-014-6601

Unclassified

SECURITY CLASSIFICATION OF THIS PAGE (When Data Entered)

31:170

574

Unclassified

SECURITY CLASSIFICATION OF THIS PAGE (When Data Entered)

The VAPE program is capable of evaluating:

- o Effects of relative wind about an aircraft
- o Effects of propulsive lift jet entrainment, vorticity, and flow blockage;
- o Effects of engine inlet flow on the aircraft flow field;
- o Engine inlet forces and moments including inlet separation;
- o Ground effects in the STOL region of flight.

The effects of relative wind about an aircraft with or without jets and/or inlet effects is determined by a very general three-dimensional potential flow panel method.

The effects of the propulsive lift jets are determined by one of three different jet models which have been extensively modified and/or developed at Vought.

The effects of engine inlet flow on the aircraft is determined by a NASA Lewis code for axisymmetric inlets which has been modified and automated at Vought. This method will determine the pressures on the inlet face and nacelle inlet lips. The VAPE program will then utilize these pressures to determine the forces and moments acting on the inlet. Calculations may also be done to determine when and where separation occurs on the inlet lip.

Unclassified

SECURITY CLASSIFICATION OF THIS PAGE (When Data Entered)

## FOREWORD

A study was conducted for the Naval Air Development center (NADC) by the Vought Corporation to develop a computerized methodology for predicting the propulsive induced aerodynamics of V/STOL aircraft in transition/STOL flight. The study was performed under Navy contract N62269-78-C-0036 with Mr. Campbell Henderson of NADC as contract monitor. The Vought efforts in this program were accomplished under the direction of Mr. T. D. Beatty who was the principal investigator for this contract. He was assisted on the contract by Mr. S. S. Kress. Both personnel are from the Flight Technologies Section of The Vought Corporation.

The authors are particularly indebted to Mrs. J. V. Timmons for her support in the programming of the computer code. Special acknowledgements are due to Mr. W. W. Rhoades, Mr. A. H. Ybarra, Mr. G. W. Wolfe, Jr., and Dr. F. C. Thames for their contributions.

This report consists of two volumes. The technical discussion of the methodology, verification of the techniques, and conclusions are presented in Volume I. Volume II is a rather detailed user's manual for the computer code developed.

Accession For	
NTIS GRA&I	<input checked="checked" type="checkbox"/>
DTIC TAB	<input type="checkbox"/>
Unannounced	<input type="checkbox"/>
Justification	
By	
Distribution/	
Availability Codes	
Dist	Avail and/or Special
A	

## TABLE OF CONTENTS

SECTION	TITLE	PAGE
	List of Illustrations .....	iv
	List of Symbols .....	viii
1	Summary .....	1-1
2	Introduction .....	2-1
3	V/STOL Aircraft Propulsive Effects Program (VAPE) .....	3-1
4	Potential Flow Program .....	4-1
5	Jet Methods .....	5-1
	5.1 Vought/Wooler Jet Model .....	5-2
	5.1.1 Multiple Jet Analysis .....	5-8
	5.1.2 Intermediate Ground Effect .....	5-12
	5.2 Vought/Weston Jet Model .....	5-17
	5.2.1 Formulation of the Jet Model .....	5-22
	5.2.2 Multiple Jet Analysis .....	5-26
	5.2.3 STOL Calculations .....	5-33
	5.2.4 Wake Effect Model .....	5-40
	5.3 Thames Rectangular Jet Model .....	5-41
	5.3.1 Vortex Simulation .....	5-41
	5.3.2 Source/Sink Simulation .....	5-47
	5.3.3 Model Applicability .....	5-53
6	Inlet Analysis Methods .....	6-1
	6.1 Vought/Stockman Program .....	6-1
	6.1.1 Geometry Representation .....	6-2
	6.1.2 Incompressible Potential Flow Solution .....	6-2
	6.1.3 Arbitrary Flow Condition Solution .....	6-3
	6.1.4 Boundary Layer Solution .....	6-4
	6.1.5 Iterative Loop .....	6-5
	6.1.6 Combined Potential Flow and Boundary Layer Routine .....	6-5
	6.2 Inlet Force and Moment Program .....	6-7
	6.2.1 Method of Solution .....	6-8
	6.2.2 Force Equations .....	6-9
	6.2.3 Moment Equations .....	6-13

## TABLE OF CONTENTS (Continued)

SECTION	TITLE	PAGE
	6.2.4 Program Code Capability .....	6-15
	6.2.5 Ram Force and Moment Arm Charts .....	6-16
6.3	Inlet Separation Analysis .....	6-25
	6.3.1 Inlet Design Variables .....	6-25
	6.3.2 Analysis Method .....	6-26
	6.3.3 Comparison to NASA Experimental Data .....	6-28
	6.3.4 Inlet Separation Charts .....	6-29
	6.3.5 Effect of Model Scale on Boundary Layer Separation .....	6-35
7	Experimental Verification .....	7-1
	7.1 Verification of Vought/Wooler Jet Model .....	7-6
	7.2 Verification of Vought/Weston Jet Model .....	7-11
	7.3 Verification of Force and Moment Method .....	7-15
8	Conclusion and Recommendation .....	8-1
9	References .....	9-1
10	Appendices .....	10-1
	10.1 Appendix A - Inlet Separation Charts .....	10-1
	10.2 Appendix B - Ram Drag Charts .....	10-10
	10.3 Appendix C - Scoop Inlet Experimental Data .....	10-18



## LIST OF ILLUSTRATIONS

SECTION	TITLE	PAGE
3.1	Schematic of Program Integration for VAPE .....	3-2
4.1	Typical Lifting Configuration .....	4-3
4.2	Representation of the Bound Vorticity by a Finite-Strength Vorticity Distribution Lying on the Wing Surface .....	4-4
4.3	Distribution of Bound Vorticity Strength Across the Span ....	4-5
5.1	Schematic of Formation of Contra-Rotating Vortices Created by the Jet Issuing into a Crossflow .....	5-1
5.2	Jet Exhausting Normally into the Freestream .....	5-2
5.3	Sink and Doublet Distributions .....	5-8
5.4	Plan View of Three Two Jet Configurations in Relation to the Free Stream Flow .....	5-9
5.5	Schematic of Jet Influence Determination .....	5-10
5.6	Image System for Ground Effect Ensures that the Ground is a Streamline .....	5-12
5.7	Input/Output Coordinate System .....	5-13
5-8	Intermediate Altitude Coordinate Transformation Model .....	5-16
5-9	Geometry of Vortex Models .....	5-18
5-10	Jet Exit Coordinate System Defined .....	5-20
5-11	Schematic of Relationship Between $(X_1, Z_1)$ , $(X_0, Z_0)$ and $\delta_j$ .....	5-21
5-12	Comparison of Calculated and Experimental Jet Path Centerlines, Jet Spacing = 5.0 Diameters, Jet Velocity Ratio, $R = 8$ .....	5-27
5-13	Schematic of Vortex Flow Field for Determining Area .....	5-29
5-14	Jet Velocity Decay .....	5-29
5-15	Aircraft in STOL Flight Regime .....	5-33
5-16	Schematic of Model Utilized for STOL Calculations in VAPE ...	5-37

## LIST OF ILLUSTRATIONS (Continued)

SECTION	TITLE	PAGE
5-17	Schematic of Rectangular Jet Model Formation .....	5-42
5-18	Multiple Source/Sink Lines for Blunt Nozzles .....	5-50
5-19	Multiple Source/Sink Lines for Streamwise Nozzles .....	5-52
6-1	Inlet Configurations and Input Parameters for Flow Routines .	6-2
6-2	Typical Potential Flow Routine Results .....	6-4
6-3	Typical Boundary Layer Routine Results .....	6-5
6-4	Vought Combined Potential Flow and Boundary Layer Program ...	6-6
6-5	Coordinate System for Force and Moment Calculations . ....	6-8
6-6	Force Schematic for Inlet Force and Moment Algorithm .....	6-9
6-7	Schematic of Moment Box for Inlet Integration .....	6-10
6-8	Schematic of Integrals (1) and (3) Domains .....	6-11
6-9	Coordinate Axis Definition .....	6-11
6-10	Transformation Description .....	6-12
6-11	Schematic of Moments Generated on Nacelle .....	6-13
6-12	NASA QCSEE GE2 Inlet Geometry .....	6-16
6-13	Effect of Velocity Ratio on Inlet Lift Force .....	6-18
6-14	Effect of Velocity Ratio on Inlet Streamwise Force.....	6-19
6-15	Effect of Velocity Ratio on Inlet Ram Moment Arm .....	6-20
6-16	Effect of Freestream Velocity on Inlet Forces and Moments....	6-21
7-16	Comparison of Thin Lip Inlet to QCSEE Configuration .....	6-22
6-18	Effect of Lip Shape on Inlet Force Components .....	6-23
6-19	Effect of Lip Shape on Inlet Ram Moment Arm .....	6-24
6-20	Inlet Nomenclature .....	6-25
6-21	Entry-Lip Nomenclature and Range of Geometric Variables .....	6-26

## LIST OF ILLUSTRATIONS (Continued)

SECTION	TITLE	PAGE
6-22	Comparison of Calculated Results with NASA Experimental Data .....	6-28
6-23	Representative Flight Conditions for Tilt-Nacelle VTOL Aircraft .....	6-30
6-24	Effect of Forward Speed and Inlet Contraction Ratio on Inlet Separation, $V_{\infty} = 40$ KTS .....	6-30
6-25	Effect of Forward Speed and Inlet Contraction Ratio on Inlet Separation, $V_{\infty} = 80$ KTS .....	6-31
6-26	Effect of forward Speed and Inlet Contraction Ratio on Inlet Separation, $V_{\infty} = 120$ KTS .....	6-31
6-27	Effect of Area Contraction Ratio and Throat Mach Number on Inlet Separation .....	6-32
6-28	Effect of Diameter Ratio on Inlet Separation .....	6-33
6-29	Effect of Internal Lip Shape on Inlet Separation .....	6-34
6-30	Effect of Model Scale on Inlet Separation .....	6-35
6-31	Effect of Scale on Skin Friction Coefficient, Windward Side of Inlet $M_{\infty} = .13$ , $\alpha = 41^\circ$ , $M_T = 0.28$ .....	6-36
6-32	Effect of Model Scale on Laminar Lip Separation .....	6-37
7-1	Geometry for Aircraft Configuration from Reference 7.1 .....	7-3
7-2	Geometry for Aircraft Configuration from Reference 7.2 .....	7-4
7-3	Geometry of Flat Plate Configuration .....	7-5
7-4	Comparison of Predicted Results from Vought/Wooler Jet Model to Experimental Data for Flat Plate Configuration ....	7-7
7-5	Comparison of Predicted Results from Vought/Wooler Jet Model to Experimental Data for the Configuration of Figure 7-1 .....	7-9
7-6	Comparison of Predicted Results from Vought/Wooler Jet Model to Experimental Data for the Configuration of Figure 7-1 .....	7-9

## LIST OF ILLUSTRATIONS (Continued)

SECTION	TITLE	PAGE
7-7	Comparison of Predicted Results from Vought/Wooler Jet Model to Experimental Data for the Configuration of Figure 7-2 .....	7-10
7-8	Comparison of Predicted Results from Vought/Weston Jet Model to Experimental Data for the Flat Plate Configuration of Figure 7-3 .....	7-12
7-9	Comparison of Predicted Results from Vought/Weston Jet Model to Experimental Data for the Configuration of Figure 7-1 .....	7-14
7-10	Comparison of Predicted Results from Vought/Weston Jet Model to Experimental Data for the Configuration of Figure 7-1 .....	7-14
7-11	Comparison of Predicted Ram Moment Arm to Experimental Data ..	7-16
Appendix A	Inlet Separation Charts .....	A-1
Appendix B	Force and Moment Charts .....	B-1
Appendix C	Scoop Inlet Experimental Data Charts .....	C-1

## LIST OF SYMBOLS

<u>SYMBOL</u>	<u>DEFINITION</u>
A	Constant (Eq 5.38) Cross Sectional Area
$A_R$	Nozzle Aspect Ratio
a	Constant used in equation for sink & vortex equation (See 5.12)
c	Constant (Eq 5.40)
c	Circumference (Eq 5.12)
$C_D$	Crossflow drag coefficient
$C_f$	Skin friction coefficient
$C_L$	Lift coefficient
$C_T$	Thrust coefficient
D	Ratio of minor to major axis of ellipse (Eq 5.23)
D	Diameter
d	Diameter
ds	Derivative of surface distance
$d_{o1j}$	Diameter of jet #1 at nozzle exit plane
E	Mass entrainment per unit length
$E_1, E_2, E_3$	Entrainment constants (Eq 5.4)
F	See Eq 5.15
$F_p$	Pressure force on jet element
$F_1$	Angle parameter (Eq 5.100)
h	Vortex half spacing
HIV	Vortex half spacing
HM	(See Eq 5.62)
$K_1, K_2, K_3, K_4$	Constants (Eq 5.50)
$l_1, l_2$	Eq 5.42

## LIST OF SYMBOLS (Continued)

<u>SYMBOL</u>	<u>DEFINITION</u>
$l$	Distance between jet centers (Eq 5.24)
$L/T$	Lift-to-thrust ratio
$M$	Mach number
$m$	Non-dimensional velocity (Eq 5.15)
$\dot{m}$	Mass flow
$M_y$	Moment in Y direction
$N$	Wall jet height
$N_5$	Wall jet height at 1/2 ( $U/U_{max}$ )
$Q$	Volume flux
$q$	Dynamic pressure
$q$	Sink strength density
$R$	Jet velocity ratio
$R_I$	Radius at edge of impingement region
$R_A, R_B$	Radii in wall jet analysis
$R$	Jet velocity ratio (Eq 5.87)
$r$	Radius
$S$	Area
$T_{i,j}$	Rotation matrix
$\frac{T_{i,j}}{T_{i,j}}$	Rotation Matrix
$U$	Velocity
$V$	Velocity
$XGT, YGT, ZGT$	Ground translated coordinate system
$X_s$	Separation line X coordinate

## LIST OF SYMBOLS (Continued)

<u>SYMBOL</u>	<u>DEFINITION</u>
<u>GREEK SYMBOLS</u>	
$\alpha$	Angle-of-attack - degrees
$\beta$	Diffusivity constant
$\sigma$	Density
$\Lambda$	Source strength
$\Omega$	Angle between jets
$\omega$	Vortex strength
$\Gamma$	Integrated vortex strength
$\delta$	Jet injection angle
$\delta_e$	Equivalent jet injection angle
$\delta^*$	Boundary layer displacement thickness
$\theta_A, \theta_B$	Angular position for wall jet
<u>SUBSCRIPTS</u>	
AMB	Ambient
a, b, c, d, e	Constants in vortex and sink equations (also used as superscripts)
c	Critical length (Eq 5.53)
cp	Control point
cor	Correction
D	Diameter
d	Diameter
e	Jet exit
G	Ground Plane
GT	Ground Translated Coordinate System

## LIST OF SYMBOLS (Continued)

<u>SYMBOL</u>	<u>DEFINITION</u>
IM	Impingement
Z	Intersection
J	Jet exit
J1	Jet #1
J2	Jet #2
J3	Jet #3
M	Max velocity point
MAX	Maximum
O	Jet exit
S	Sink
S	Static
T	Total
V	Vortex
VS	Vortex segment
WJ	Wall jet
WF	Wooler fixed coordinate system
X, Y, Z	Direction of velocity vector
$\infty$	Freestream

SUPERSCRIPT

*	Non-dimensional parameter
'	Derivative or modified velocity ratio (Eq 5.58)
→	Vector notation
V	Vortex
S	Sink
-	Arithmetic Average



## 1.0 SUMMARY

A computerized prediction method for propulsive induced forces and moments in transition and short takeoff and landing (STOL) flight has been developed for the Naval Air Development Center (NADC) under contract number N69969-78-C-0036. The method developed was based on the Vought V/STOL aircraft propulsive effects computer program (VAPE).

The VAPE program is capable of evaluating:

- o Effects of relative wind about an aircraft
- o Effects of propulsive lift jet entrainment, vorticity, and flow blockage
- o Effects of engine inlet flow on the aircraft flow field
- o Engine inlet forces and moments including inlet separation
- o Ground effects in the STOL region of flight

The effects of relative wind about an aircraft with or without jets and/or inlet effects is determined by a very general three-dimensional potential flow panel method.

The effects of the propulsive lift jets are determined by one of three different jet models which have been extensively modified and/or developed at Vought. Some of the major modifications made to the jet models at Vought include:

- o Intermediate height ground effects calculations
- o Calculations of the flow field near the ground in the STOL region of flight

The effects of engine inlet flow on the aircraft is determined by a NASA Lewis code for axisymmetric inlets which has been modified and automated at Vought. This method will determine the pressures on the inlet face and nacelle inlet lips. The VAPE program will then utilize these pressures to determine the forces and moments acting on the inlet. Calculations may also be done to determine when and where separation occurs on the inlet lip.

The various options of the VAPE program have been verified by comparisons between calculated and experimental values.

A computer program code was delivered to NADC and made operational on the NACD CDC 6600 computer. A users manual for this program is contained in Volume II of this report.

A set of charts of ram drag moment arm and conditions for inlet lip separation generated as design aids are contained in Appendices A and B.

## 2.0 INTRODUCTION

V/STOL concepts currently being investigated for Navy missions employ various arrangements of lift and/or lift/cruise engines. The experimental data on V/STOL configurations obtained to date indicate that sizable propulsion induced force and moment characteristics can occur in the V/STOL flight mode. The induced flow around a jet V/STOL aircraft depends upon the flight speed of the vehicle, its height above the ground, and the placement of the jets on the aircraft.

During flight of a V/STOL aircraft in the transition mode, jet induced pressures and downwash on the aircraft can cause a significant change in lift. The change tends to increase with increasing forward velocity. A nose-up pitching moment is often caused by the jet induced effects, and this moment also increases with increased speed. Downwash induced at the horizontal tail and on the wing can cause trim changes and stability problems. In addition, the low pressures which cause a nose-up pitching moment also produce a rolling moment in a sideslip or crosswind condition.

The presence of these jet induced effects poses a problem to the aircraft designer in the conceptual or preliminary design stage, since the designer must account for all these propulsive induced effects to obtain the best performance.

These propulsive induced effects have caused considerable efforts to be expended throughout the aircraft industry to develop analytical and empirical prediction methods. Most of these efforts have been concentrated into two basic categories: (1) In Ground Effect (IGE) and (2) Out of Ground Effect (OGE). Various techniques have been developed to simulate the propulsive jet and its influence upon the aircraft.

The objective of this contract effort was to develop a computational aerodynamic method for predicting the flow field about a V/STOL aircraft in the transition region of flight, i.e., the region of flight between forward conventional flight and hovering flight. A further objective was to develop an algorithm to determine the jet induced effects for an aircraft in the STOL regime, i.e., jets deflected 30 to 90 degrees, forward velocity < 80 knots. In this regime it is assumed that the jets impinge the ground and form wall jets, but no jet is reflected back onto the aircraft surface.

One other item to be addressed in order that the entire flow field about the aircraft be modelled correctly, is the inlet flow into the nacelle. Therefore an inlet analysis routine was developed which not only determines velocities to be used on the inlet face in the potential flow analysis but also gives the inlet forces and moments acting on the inlet.

The required objectives were accomplished through modifications and extensions of the Vought VAPE program.

All of the methods contained in VAPE have been extensively modified and improved at Vought. This combination of programs provides a reliable, accurate and versatile design procedure for V/STOL aircraft.

### 3.0 V/STOL AIRCRAFT PROPULSIVE EFFECTS PROGRAM (VAPE)

The Vought V/STOL aircraft propulsive effects program system is a union of six potential flow computational techniques: (1) The Hess Three Dimensional Analysis Program, (2) The Vought/Stockman Inlet Analysis Program, (3) The Vought/Wooler Jet Model, (4) The Vought/Weston Jet Model (5) The Thames Rectangular Jet Model, and (6) The Vought STOL module.

These programs are used in conjunction with geometry models to form a very general and very efficient program for determining the propulsive induced effects. A schematic of the program options and the basic program logic is presented in Figure 3-1. The configuration geometry is digitized using the geometry module with the plot and symmetry modules used to facilitate model formulation. This model is then input to the Hess potential flow program where the actual aerodynamic characteristics of the aircraft are determined.

The nacelle geometry is input to the Vought/Stockman inlet module. The inlet module determines the velocity on the inlet face needed to obtain the correct mass flow through the nacelle. These velocities are then transferred to the Hess program to be used as boundary conditions on the inlet face.

A jet model determines the induced velocities due to the jet exhaust on the panels of the model. These velocities are then converted to a normal velocity acting at the centroid of each panel to be used as boundary conditions in Hess. The Vought STOL module is used when the aircraft is near the ground. This model determines induced velocities on the ground plane produced by the wall jet formed when the jet impinges the ground. These induced velocities are input to the Hess program together with the induced velocities on the aircraft panels. The Hess solution is then executed with the above boundary conditions producing the aerodynamic forces on the aircraft which include inlet and jet exhaust effects.

Major modules of VAPE are discussed in the following text. These modules are:

- o Vought geometry module
- o Hess potential flow module
- o Vought/Stockman inlet analysis module
- o Vought/Wooler jet model
- o Vought/Weston jet model
- o Thames rectangular jet model
- o Vought inlet force and moment module
- o Vought STOL module

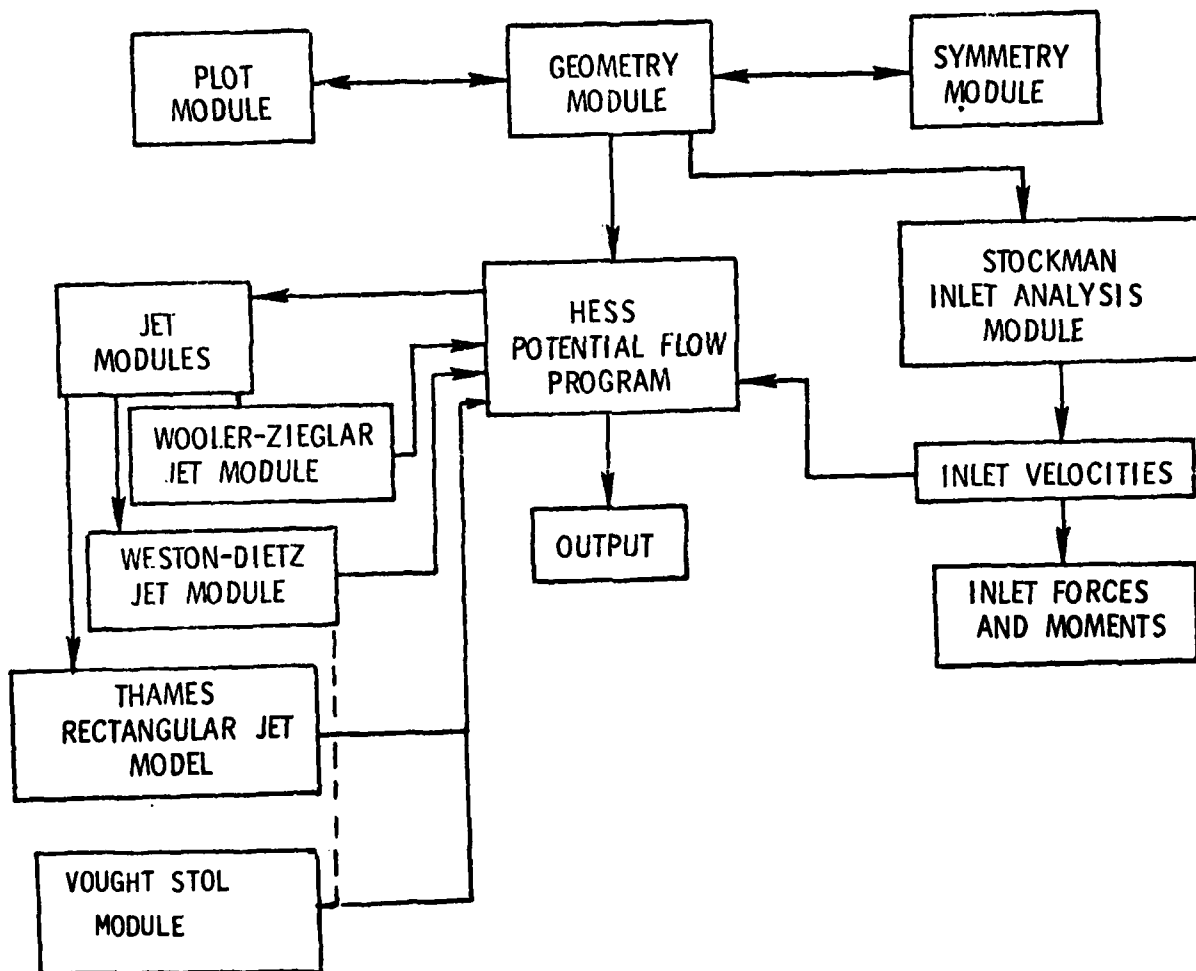


Figure 3-1. Schematic of Program Interaction for VAPE

#### 4.0 POTENTIAL FLOW METHOD

The calculation of the propulsive induced effects requires a very sophisticated three-dimensional potential flow technique due to the importance of properly modeling the fuselage geometry as discussed in reference 4-1. There are several approaches which are used to determine the potential flow field in three-dimensions, only two of which provide the proper basis for predicting the propulsive induced effects: (1) A Vortex Lattice Method and (2) A Panel Method. The first approach, Vortex Lattice Methods are relatively simple, use reasonable amounts of computer time and are easy to input. They do a very good job of predicting the flow field about some configurations. Unfortunately, there are no Vortex Lattice Methods available which have a good representation of the fuselage. Therefore, since most V/STOL configurations have fairly large nacelles and fuselages, it was decided that it would be undesirable to use a Vortex Lattice Method as the basis for a sophisticated program such as VAPE.

The second approach, Panel Methods, will calculate the flow field about arbitrary configurations including fuselages, nacelles, or lifting surfaces. Therefore, it was decided that a panel method should be used as a basis for the VAPE program. There are several Panel Methods available, but in this author's opinion, by far the best method available for this application is that of Hess, references 4-2 and 4-3. This method is currently being used throughout the industry and at several government facilities.

A complete description of the Hess Program is given in the above references, so only a description of the basic formulation taken from reference 4-3 will be presented below in order to familiarize the reader with the operation of the program.

References 4-4 and 4-5 review the long-term effort of Hess and his colleagues in the field of potential-flow calculation. Among the methods described are those for lifting two-dimensional flows and nonlifting three-dimensional flows. The latter is described in somewhat greater detail in references 4-6. The three-dimensional nonlifting method forms the basis on which is built the lifting method to be described here as well as other lifting methods, references 4-7 through 4-10. All of these methods, of all dimensionality, are "exact" in the sense that no approximations are made in the basic formulation, as is done in small-perturbation or lifting-surface theories. The basis of these methods is a distribution of source density over the surface of the body about which flow is to be computed. Application of the normal-velocity boundary condition on the surface of the body yields an integral equation for the distribution function of the source density, where the domain of integration is the body surface. Once this equation is solved for the source distribution, flow velocities both on and off the body surface can be calculated. In lifting two-dimensional cases the required circulation is produced by a surface vorticity distribution whose total strength is determined from the Kutta condition reference 4-3.

In the nonlifting program, (reference 4-5) the body is specified to the computer by a set of points which presumably lie exactly on the body surface. The input order is such that these points successively define a family of curves lying on the body surface. These curves, which have some of the features of surface coordinates, have been designated "N-lines". The points

are associated into groups of four "adjacent" points to form plane quadrilateral surface elements, the total set of which is an approximation to the body surface. Two adjacent N-lines bound a "strip" of elements which in many applications is of approximately constant width. As a logical device a number of N-lines can be associated into a "section". Often a section is simply an entire body, but separate sections are often used to represent geometrically different parts of the same body, for example, a wing and a fuselage. Also sections are used to concentrate elements in certain regions of a body.

On each element one point is selected where the normal velocity boundary condition is to be applied and where flow velocities are to be computed. This point, which is designated the control point of the element, has been defined in various ways in the past but currently is identified with the centroid of the element. Formulas have been derived that give the components of velocity induced at a general point in space by a unit value of source density on a general quadrilateral element. These formulas allow the velocities induced by the elements on each other's control points to be calculated. Equating the normal velocity induced by all elements at each control point to the negative of the normal component of the onset flow (for the case of zero total normal velocity) yields a set of linear algebraic equations for the values of source density on the elements. Once these are solved, flow velocities can be computed at the centroids and at any selected point in the flow field. For the lifting application it is important to point out that the onset flow need not be a uniform stream. Moreover, solutions for several flows may be obtained simultaneously. The onset flow affects only the right side of the linear equations for the source density not the coefficient matrix. Thus, if a direct matrix solution is employed, several onset flows may be treated in nearly the same computing time as a single onset flow.

Essentially the same scheme for surface elements is used in the lifting three-dimensional method, and use is made of the N-lines and sections to help define the bound vorticity.

Certain portions of a general aerodynamic configuration do not have well-defined trailing edges and are not normally thought of as having their own bound vorticity, e.g. a fuselage. These portions are called nonlifting portions to signify that they do not possess independent bound vorticity and that a Kutta condition is not applied to them. However, in general, the fluid exerts nonzero pressure forces on nonlifting portions due to interference pressures from other nearby portions of the configuration and due to extensions of the bound vorticity from lifting portions. Nonlifting portions are approximated by general plane quadrilateral elements in exactly the same way as in the nonlifting method of reference 4-3. In the main calculation such elements have source density but not vorticity. The organization of the input data by sections (see above) is a natural way of isolating lifting and nonlifting portions.

Portions of a general configuration that possess definite trailing edges (usually sharp corners) and contain bound vorticity are called lifting portions. The most frequently occurring application with both lifting and nonlifting portions is a wing-fuselage. Accordingly, this configuration is

used as an illustrative example in Figure 4-1. On a lifting portion the N-lines are approximately in the free-stream direction. On each N-line points are input beginning at the trailing edge, continuing around a "section curve" of the wing, returning to the trailing edge, and proceeding downstream to define the trailing vortex wake. The wake may be defined as far downstream as desired. Provision has been made to consider the last element of the wake semi-infinite so that wake definition may be terminated at any point aft of where the wake curvature in the stream direction may be neglected. The set of elements formed from points on a pair of adjacent N-lines is called a "lifting-strip" of elements. These elements are plane trapezoids whose parallel sides lie along the N-lines. The strip contains elements both on the body and in the wake. Although two adjacent N-lines are not quite parallel in general, they are nearly parallel in most cases. The centroids of the elements are used as control points. Thus, for each lifting strip the locus of control points is approximately midway between the two N-lines used to generate the strip. Elements of lifting strips have source densities whose strengths are determined to give zero (or prescribed) normal velocity at the control points.

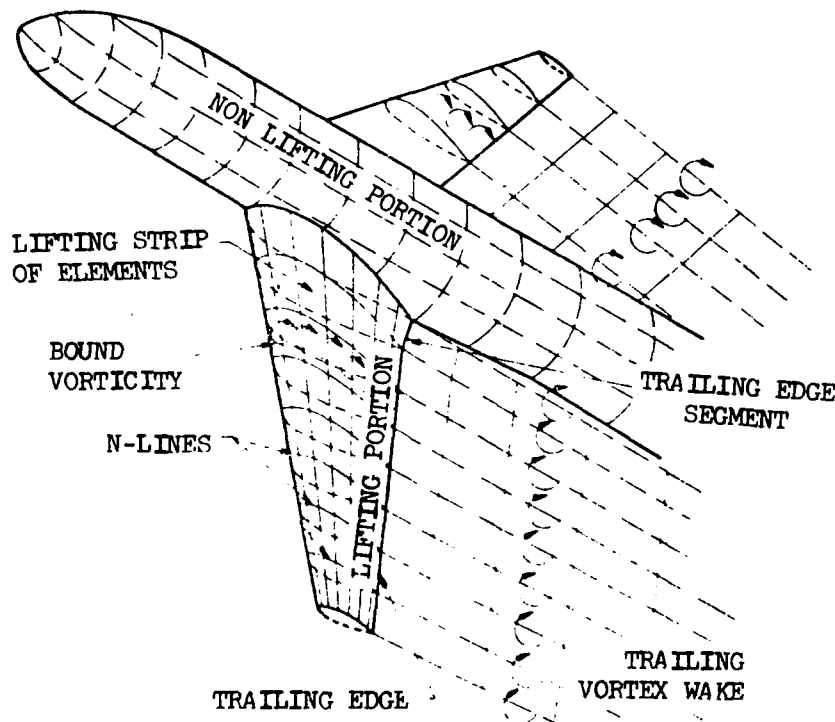


Figure 4-1. Typical Lifting Configuration

In addition to the source densities on the elements, lifting portions also possess a distribution of bound vorticity. The spanwise variation of the bound vorticity determines the distribution of the trailing vorticity, which lies along the input wake. To implement a calculation scheme, the form assumed for the bound vorticity must contain a number of adjustable parameters equal to the number of lifting strips on that lifting portion. The values of these

parameters are determined by applying a Kutta condition at the trailing-edge segment (Figure 4-1) of each lifting strip. The simplest form of the bound vorticity distribution utilizes a set of individual distributions, each of which is nonzero only on one lifting strip. The complete distribution consists of a linear combination of these individual distributions, each of which is nonzero on a different lifting strip. The combination constants of the linear combination are the required adjustable parameters. This is the type of distribution used in the present method. Other existing methods (reference 4-7 through 4-10) also use this type of distribution. The value of the parameter multiplying the distribution associated with a particular lifting strip represents the strength of the bound vorticity at the "spanwise" location of that strip. Thus, as expected, the "spanwise" variation of bound vorticity is determined by the Kutta condition. More precisely the "spanwise" variation of vorticity from one lifting strip to another is determined by the Kutta condition. The "spanwise" variation of vorticity within the small but finite span of each individual lifting strip is basically a question of the order of accuracy of a numerical integration.

The Hess method uses a finite-strength sheet of vorticity on the surface of the wing, i.e., the vorticity lies on the quadrilateral surface elements. The vorticity strength is assumed constant all around the airfoil section. Some features of this formulation are illustrated in Figure 4-2.

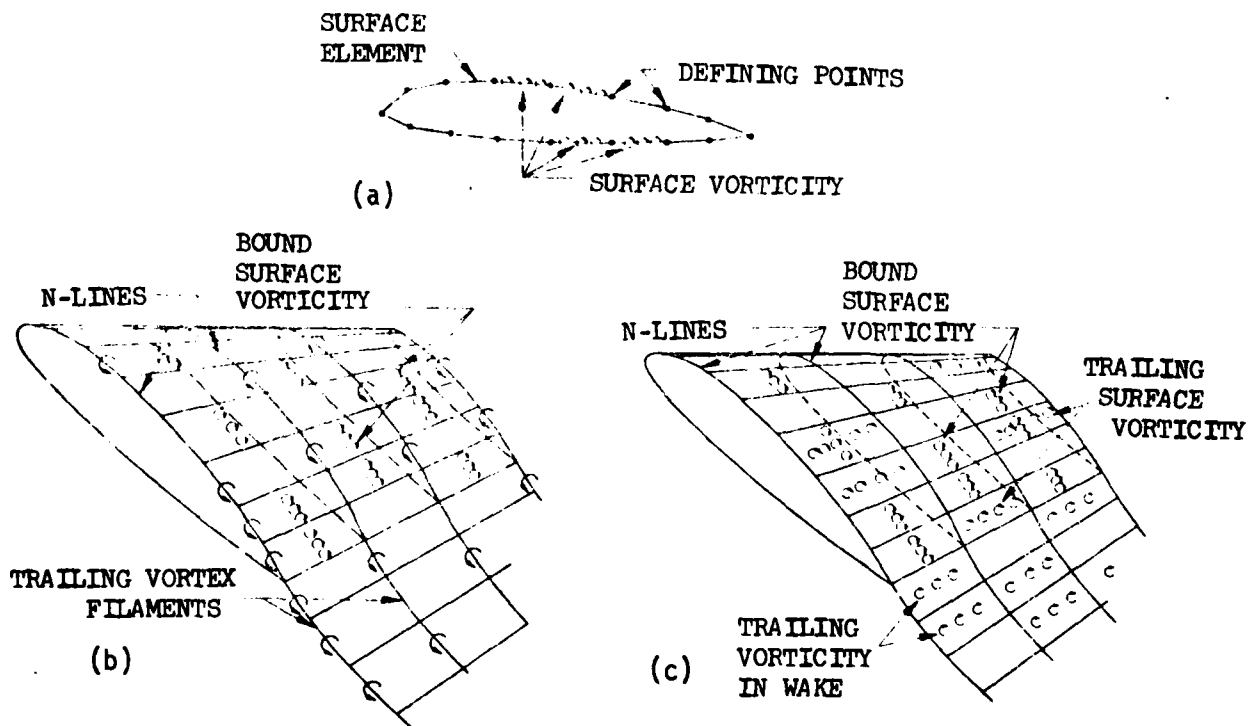


Figure 4-2. Representation of the bound vorticity by a finite-strength vorticity distribution lying on the wing surface. (a) A section curve of the wing. (b) The complete three-dimensional vorticity pattern using a step function spanwise variation. (c) The complete three-dimensional vorticity pattern using a piecewise linear spanwise variation.



The spanwise variation of vorticity in the version of Hess contained in VAPE is assumed constant over the span of each lifting strip. This form of the bound vorticity has the advantage of simplicity and does not require special handling at the end of a lifting section, e.g. a wing tip. However, it must be noted, that the trailing vorticity takes the form of concentrated vortex filaments along the N-lines. Figure 4-3 presents a schematic of the bound vorticity strength across the span of a wing using the above distribution.

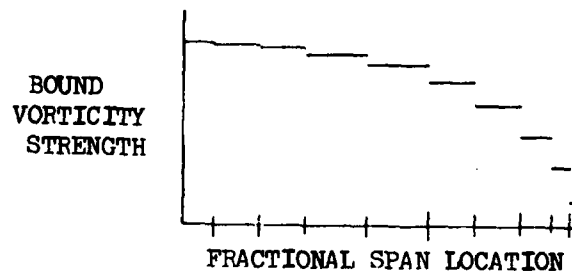


Figure 4-3. Distribution of bound vorticity strength across the span

Further description of the Hess method can be obtained from the references cited earlier.

The Hess program has been modified at Vought in order to improve computational efficiency. The input and output have been modified and the machine storage space has been reduced. In addition, the computational time has been reduced due to various changes in the program code. None of these changes however effect the basic formulation of the program. Also, the Gothert compressibility algorithm has been incorporated into the Hess program along with an option to allow flow through boundary conditions, i.e.,  $V_N$  at the control point may be different than zero on any panel. This latter option is necessary for modeling inlets and for accounting for jet induced effects.

In summary, the Hess program contained in the VAPE system is a very powerful tool for analysing V/STOL configurations with or without jets operating.

## 5.0 JET METHODS

The high velocity airstream exiting from a jet nozzle into a subsonic crosswind has a high level of momentum which enables the jet to penetrate the crossflow in essentially an inviscid fashion. At this point the jet appears to be a solid obstruction to the crossflow. However, as the jet penetrates the crossflow further, it entrains low momentum fluid. In addition, viscous effects begin to erode the momentum of the primary jet flow. As the velocity in the jet plume falls off, the jet decays in the direction of the crossflow and eventually becomes parallel to the crossflow. This flow field is shown in Figure 5-1. This interaction basically results in the jet spreading, deforming, and deflecting, while the crossflow is displaced and entrained into the jet. In addition a wake region is formed behind the jet at the jet exit.

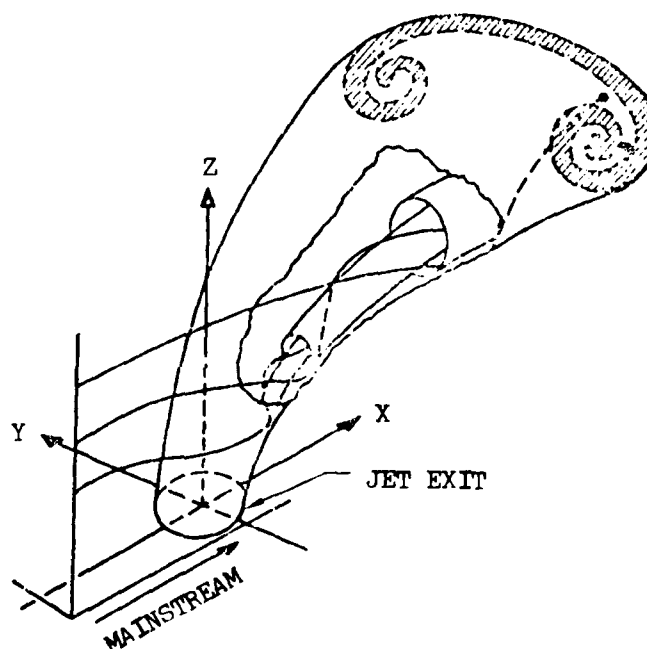


Figure 5-1. Schematic of Formation of Contra-Rotating Vortices Created by the Jet Issuing Into a Crossflow

There have been several jet models developed which are applicable to this flight regime, as described in references 5-1 through 5-4.

All of these methods predict the jet induced fields, the flow outside the jet efflux, based on some empirical information. The models have the common feature of using a potential flow representation for the jet induced flow field. They differ in how the flow effects caused by the jet are represented and in which factors (i.e., blockage, entrainment, or wake effect) received the most attention in the analysis.

Among the best of these techniques from the viewpoint of simplicity and applicability are the methods of Wooler, reference 5-5, and Fearn, Dietz, and Weston, reference 5-6 and 5-7. These jet simulation techniques along with a new method developed by Thames, reference 5-8, for rectangular jets are the methods contained in the VAPE system. The above methods and the modifications made will be discussed in the following sections.

At this point in the discussion of jets in a crossflow mention needs to be made of one of the primary parameters used to predict the jet effects on the flow field. This parameter has been used by various authors in several different methods. The parameter is the ratio of the square root of the momentum flux across the jet orifice to the momentum flux of the crossflow across an equal area. This ratio is denoted by  $R$  as shown in the following equation.

$$R = \left[ \frac{\int_{S_0} \rho_J V_J^2 d\sigma}{\rho_\infty V_\infty^2 S_0} \right]^{1/2} \quad (5.1)$$

Where  $S_0$  is the area of the jet exit. With a constant velocity  $V_J$  across the jet orifice and equal pressures in the crossflow and the jet orifice, equation 5.1 simplifies to a ratio of Mach numbers,

$$R = \frac{M_J}{M_\infty} \quad (5.2)$$

Further, if the mass densities of the jet and crossflow fluids are the same, equation 5.2 becomes a ratio of jet to crossflow velocities,

$$R = \frac{V_J}{V_\infty} \quad (5.3)$$

It is conventional to call the ratio  $R$  the effective velocity ratio, because of the last relation.

#### 5.1 VOUGHT/WOOLER JET MODEL

The version of the Wooler jet model, contained in VAPE, is basically that presented in references 5-2 and 5-5 with two modifications: (1) the method is limited to two jets per jet system, (2) an intermediate ground effects algorithm has been included. It should be noted that in VAPE more than two jets may be treated by utilizing multiple jet systems. There is no interaction assumed between systems, which is not correct, however, in practice, the results obtained are good. Woolers program is well documented in the references cited so only a review of the method will be presented in this report.

It has been stated earlier that when a jet exhausts into a crossflow it is deflected and modified by entrainment. Wooler assumed that the deflection is due partly to viscous entrainment and partly due to the force on the jet surface resulting from the pressure distribution around the jet. He also assumed that the flow is incompressible and that viscous effects other than entrainment may be neglected. This latter effect is accounted for by the following empirical expression for the mass entrainment per unit length,  $E$ , on the jet

$$E = \rho E_1 U_\infty d \cos \theta + \frac{\rho E_2 [U_j - U_\infty \sin \theta] C}{1 + E_3 \frac{U_\infty}{U_j} \cos \theta} \quad (5.4)$$

Figure 5.2 presents the coordinate system Wooler uses for his model.

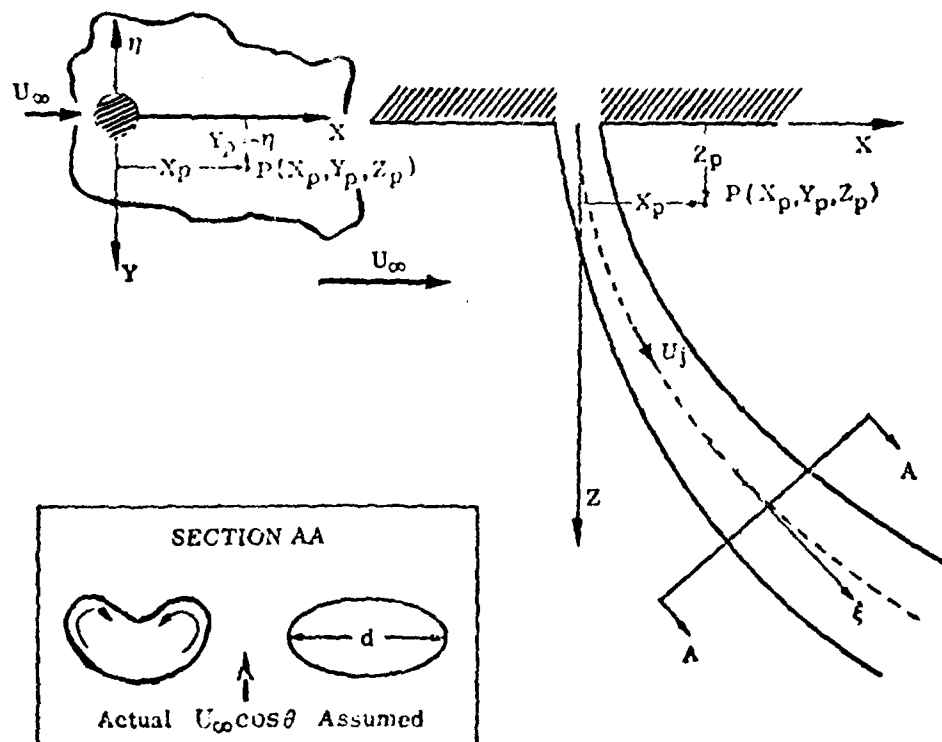


Figure 5-2. Jet Exhausting Normally Into the Freestream

The net force acting on the boundary as a result of the pressure differential around the jet is accounted for by a crossflow drag analogy. The force for a jet element of unit length is

$$F_p = \frac{1}{2} C_D \rho U_\infty^2 \cos^2 \theta dJ \quad (5.5)$$

where  $C_D$  is the crossflow drag coefficient of the jet. This force acts perpendicular to the local jet centerline direction. This force along with the mainstream momentum contribution, supplies the necessary force to produce a centripetal acceleration of the local jet mass, thus causing the jet to bend.

Considering the jet to be divided into a development region and a fully developed region, termed Region I and Region II, respectively, Wooler assumes that the cross-sectional shape of the jet envelope changes linearly from circular to elliptical in Region I and remains elliptical in Region II. The elliptical cross-section is also assumed to have a major to minor axis ratio of 4.0. The extent of Region I, is given by

$$0 \leq \frac{z}{d_0} \leq .3 \frac{U_{j0}}{U_\infty} \quad \text{REGION I} \quad (5.6)$$

$$\frac{z}{d_0} \geq .3 \frac{U_{j0}}{U_\infty} \quad \text{REGION II} \quad (5.7)$$

where  $U_{j0}$  and  $d_0$  are the jet exit velocity and diameter respectively.

The crossflow drag coefficient is allowed to vary from 1.0 at the jet exit to 1.8 at the end of Region I. Throughout Region II, the crossflow drag coefficient remains constant and, therefore, equal to 1.8.

With entrainment into and the pressures forces on the jet envelope prescribed, the jet-efflux equations of motion can be expressed as follows:

$$\text{Continuity:} \quad \rho \frac{d(A_J U_J)}{dS} = E \quad (5.8)$$

$$\text{Momentum:} \quad \rho \frac{d(A_J U_J^2)}{dS} = E U_\infty \sin \theta \quad (5.9)$$

$$\text{Force:} \quad \rho \frac{A_J U_J^2}{R} = E U_\infty \cos \theta + \frac{1}{2} \rho (U_\infty \cos \theta)^2 d_J C_D \quad (5.10)$$

where  $R$  is the radius of curvature of the jet centerline and  $A_J$  is the local jet cross sectional area. Before proceeding to a solution of the equations of motion, Wooler establishes a functional relationship between the cross sectional area  $A_J$ , the circumference  $C$  of the jet, and the jet growth.

On the basis of assumptions made earlier, the geometric characteristics  $A_J$  and  $C$  of the jet can be treated in two regions, namely Region I and Region II.

Region I: In this region, the jet has been assumed to deform from a circular to an elliptical cross section. The ratio of minor to major axis decreases linearly with  $z$  from 1 at  $z/d_{j_0} = 0$  to  $1/4$  at  $z/d_{j_0} = -0.3 \frac{U_{j_0}}{U_\infty}$ .

Therefore the expressions used in Region I for  $A_J$  and  $C$  are:

$$A_J = \frac{\pi d^2}{4} \left[ 1 - \frac{5}{2} \left( \frac{z}{d_0} \right) \left( \frac{U_\infty}{U_{j_0}} \right) \right] \quad (5.11)$$

$$C = \frac{\pi d}{\sqrt{2}} \left[ 1 + \left\{ 1 - \frac{5}{2} \left( \frac{z}{d_0} \right) \left( \frac{U_\infty}{U_{j_0}} \right) \right\}^2 \right]^{1/2} \quad (5.12)$$

Region II: In this region the jet is assumed to retain a similar cross section. Hence,  $A_J$  and  $C$  can be written as

$$A_J = \frac{\pi d_J^2}{16} \quad (5.13)$$

$$C = 2.24 d_J \quad (5.14)$$

The next step is the integration of the equations of motion. This is explained in detail in reference 5.2 so only the final form of the equations will be presented herein.

$$z^* = \frac{z}{d_0}, \quad U_J^* = \frac{U_J}{U_{j_0}}, \quad F = 1 - \frac{5}{2} \frac{z^*}{m} \quad (5.15)$$

Region 1.

$$m = \frac{U_{j_0}}{U_\infty}, \quad \frac{d}{d_0} = d^*$$

$$\frac{dU_J^*}{dz^*} = \left\{ E_1 \cos \theta + \frac{E_2 (mU_J^* - \sin \theta) \pi}{1 + E_3 \cos \theta / (U_J^* m)} \left[ \frac{1 + F^2}{2} \right]^{1/2} \right\} \left\{ \frac{\sin \theta - mU_J^*}{\frac{\pi}{4} F d^* m^2 U_J^* \cos \theta} \right\}$$

$$\frac{dd^*}{dz^*} = \left\{ \left[ E_1 \cos \theta + \frac{E_2 [mU_J^* - \sin \theta] \pi}{1 + E_3 \frac{\cos \theta}{U_J^* m}} \left| \frac{1 + F^2}{2} \right|^{\frac{1}{2}} \right] \frac{d^*}{m \cos \theta} + \frac{5}{8} (\pi d^*)^2 \frac{U_J^*}{m} - \frac{\pi}{4} d^{*2} F \frac{dU_J^*}{dz^*} \right\} \frac{2}{\pi d^* U_J^* F} \quad (5.16)$$

$$\frac{d^2 x^*}{dz^{*2}} = \left| 1 + \left( \frac{dx^*}{dz^*} \right)^2 \right|^{\frac{3}{2}} \cos \theta$$

$$X \left\{ \frac{(E_1 + \frac{C_D}{2}) \cos \theta + \frac{E_2 (mU_J^* - \sin \theta) \pi}{1 + E_3 \frac{\cos \theta}{U_J^* m}} \left| \frac{1 + F^2}{2} \right|^{\frac{1}{2}}}{m^2 (\frac{\pi}{4}) d^* U_J^{*2} F} \right\} \quad (5.17)$$

Region II

$$\frac{dU_J^*}{dz^*} = \frac{16}{\pi d^2 m^2 U_J^* \cos \theta} (\sin \theta - mU_J^*) \quad (5.18)$$

$$X \left\{ E_1 \cos \theta + \frac{2.24 E_2 (mU_J^* - \sin \theta)}{1 + E_3 \frac{\cos \theta}{U_J^* m}} \right\}$$

$$\frac{dd^*}{dz^*} = \frac{E_1 \cos \theta + \frac{2.24 E_2 (mU_J^* - \sin \theta)}{1 + E_3 \frac{\cos \theta}{U_J^* m}} - \frac{\pi}{16} m \cos \theta d^* \frac{dU_J^*}{dz^*}}{\frac{\pi}{8} m \cos \theta U_J^*} \quad (5.19)$$

$$\frac{d^2 x^*}{dz^{*2}} = \left| 1 + \left( \frac{dx^*}{dz^*} \right)^2 \right|^{\frac{3}{2}} \left\{ (E_1 + \frac{C_D}{2}) \cos \theta + \frac{2.24 E_2 (mU_J^* - \sin \theta)}{1 + E_3 \frac{\cos \theta}{U_J^* m}} \right\} \quad (5.20)$$

$$X \frac{16 \cos \theta}{\pi m^2 d^* U_J^*}$$

These equations with the additional substitution

$$\cos \theta = \frac{1}{[1 + (\frac{dx^*}{dz})^2]^{\frac{1}{2}}} \quad \& \quad \sin \theta = \frac{\frac{dx^*}{dz}}{[1 + (\frac{dx^*}{dz})^2]^{\frac{1}{2}}} \quad (5.21)$$

Constitute a set of differential equations to be solved for  $U_j^*$ ,  $d^*$ , and  $x^*$  as functions of  $z^*$  and the parameters  $E_1$ ,  $E_2$ ,  $E_3$  and  $C_D$ .

This set of first order differential equations is solved in Woolers method by means of a fourth order Adams predictor corrector method using a Runge-Kutta starting solution. The initial conditions at the jet exit are

$$z^* = 0, \quad x^* = 0, \quad U_j^* = 1 \quad \& \quad \frac{dx^*}{dz} = 0 \quad (5.22)$$

The values of  $E_1$ ,  $E_2$ , and  $E_3$  are defined as follows:

$E_1 = .45$  &  $E_3 = 30$  based on test data and related correlations  $E_2$  is allowed to vary in the development region as discussed in reference 5-2. The value of  $C_D$  is given by the following relationship

$$C_D = [-\frac{1}{D^2} + \frac{6.6}{D} + .4] \frac{1}{6} \quad (5.23)$$

where  $D$  = ratio of minor to major axis of the ellipse representing the jet.

To obtain the jet induced velocity field, Wooler assumed the entrained fluid to be represented by a uniform sink distribution placed orthogonal to the plane of the jet and the mainstream (see Figure 5-3) and a distribution of doublets with their axis perpendicular to the jet centerline to represent the so-called jet "blockage" phenomenon. The strength of the doublet distribution is obtained from two-dimensional analogy. In effect, the flow considered is that past an equivalent circular cylinder since the strength is obtained from the  $1/z$  term in the complex velocity expansion  $w(z)$  for the two-dimensional flow past an ellipse. In addition to the sink and doublet distribution, Wooler has introduced a third set of singularities which are also distributed along the calculated jet centerline. This latter is a set of point sources which are added to compensate for the invalidity of the hypothesized entrainment expression. The source strength is made proportional to the local curvature, which is justified by Wooler mainly through comparison with



experimental results. The total jet induced velocity at a point  $(x, y, z)$  in space can be obtained by integrating the effects of all singularities. The details of the calculation procedure are given in reference 5-2.

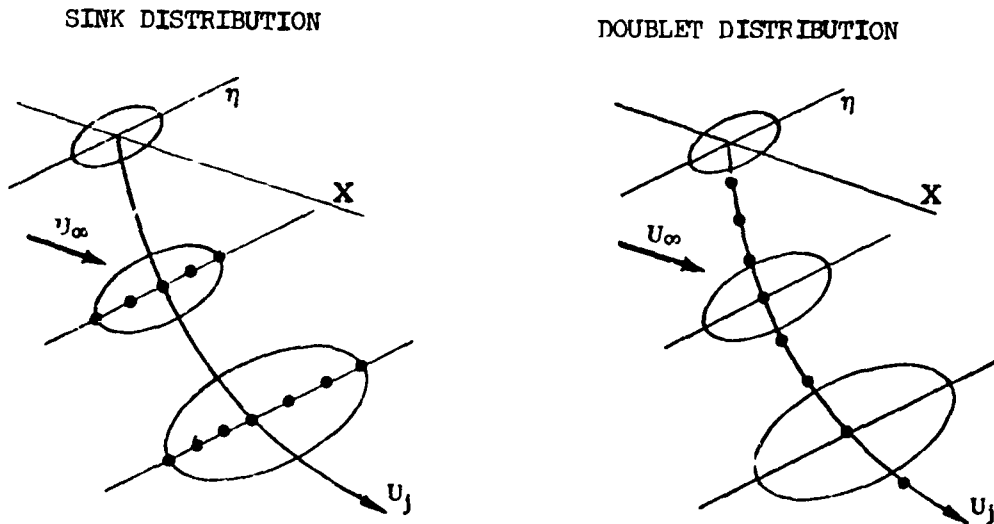


Figure 5-3. Sink and Doublet Distributions

#### 5.1.1 MULTIPLE JET ANALYSIS

The single jet analytical model can be applied to the computation of the interaction flow field due to multiple exhausting jets. A multiple jet configuration is treated as a combination of discrete jets, with each jet (including jets resulting from coalescence of jets) being replaced by its representative singularity distribution to obtain the induced velocity field. The development of the two-jet model is discussed below.

Two assumptions are made for the two jet model:

- a. The leading (or upstream) jet develops independently of the downstream jet.
- b. The downstream jet exhausts into a free stream of reduced dynamic pressure due to blockage by the upstream jet.

These assumptions are substantiated by wind tunnel tests.

Figure 5-4 shows a plan view of three two jet configurations in relation to the free stream flow. Arrangements (a) and (c) represent limiting cases. Arrangement (a) allows each jet to develop independently to the point where

growth of the jets in the direction normal to the flow causes them to intersect. Arrangement (c) places the downstream jet entirely in the zone of influence of the upstream jet. Arrangement (b) shows the downstream jet as partially in the zone of influence of the upstream jet.

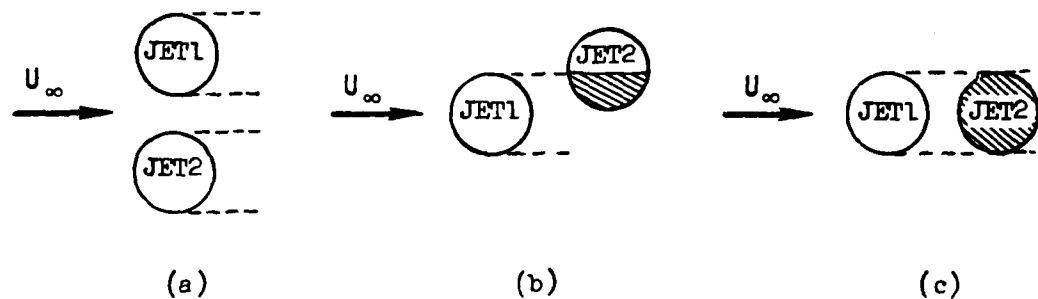


Figure 5-4. Plan View of Three Two Jet Configurations in Relation to the Free Stream Flow

Although Figure 5-4 shows the relationship of the jets in the plane of the jet exits, the determination of the degree of influence of the upstream jet (JET 1) on the downstream jet (JET 2) can be carried out for each element of JET1, as shown in the general case of Figure 5-5. Plane L is defined as the plane perpendicular to the local velocity vector ( $U_j$ ) of JET 1 at a selected point on its centerline. The intersection of plane L with JET 2 locates the cross-section of JET 2 which is affected by the jet cross-section at the selected point on the centerline of JET 1. Plane M passes through the selected centerline point of JET 1 and contains the vectors  $U_j$  and the free stream velocity vector,  $U_\infty$ . The intersection of plane M with the JET 2 cross-section in plane L is determined next. From this determination, a calculation can be made of the extent to which the selected JET 1 cross section influences the JET 2 cross section.

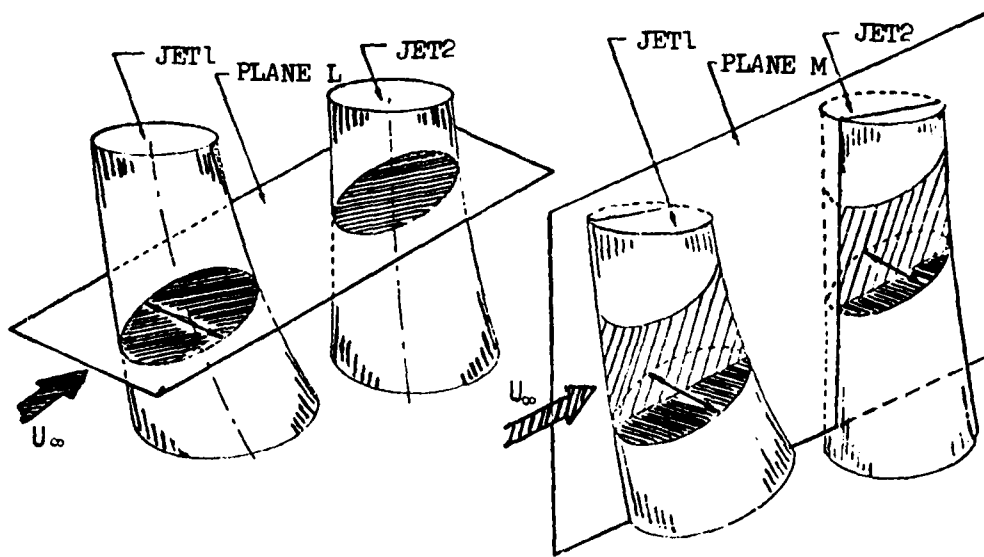


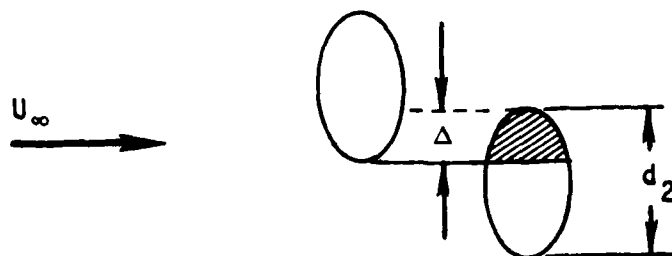
Figure 5-5. Schematic of Jet Influence Determination

The following empirical relationships can now be used to predict the dynamic pressure,  $q_e$ , which the downstream jet experiences as a result of crossflow blockage by the upstream jet. For complete overlap of JET 2 by JET 1 (Case c of Figure 5-4) experiment shows

$$q_e = \left\{ \frac{\frac{l}{d_{01J}} - 1.}{\frac{l}{d_{01J}} + .75} \right\} \sqrt{q_\infty} \quad \text{with } \left( \frac{l}{d_{01J}} > 1 \right) \quad (5.24)$$

where

$l$  is the distance between the centers of the jet cross sections, and  $d_{01J}$  is the diameter of JET 1 at the nozzle exit plane. When the two jets are not aligned, an effective crossflow dynamic pressure,  $q_B$ , which is a weighted mean of  $q_e$  given above and  $q_\infty$  is utilized. The weighting of the dynamic pressure is determined from the degree of overlap between the upstream and downstream jet elements shown in schematic form below.



$$\sqrt{q_B} = \frac{\Delta\sqrt{q_e} + (d_2 - \Delta)\sqrt{q_\infty}}{d_2} \quad (5.25)$$

Determination of the jet envelope for JET 1 proceeds in the manner described for determining the envelope for a single jet. The JET 1 computations end when an intersection of JET 1 with JET 2 has been found. Determination of the jet envelope for JET 2 proceeds at the same time as the computations for JET 1. The computation procedure is the same as that used for a single jet except the effective free stream velocity used for JET 2 is based on  $q_B$  instead of the free stream dynamic pressure.

When the intersection of the two jets is detected in the computations, initial conditions for the merged jet which results are determined from the following continuity and momentum considerations.

$$\begin{aligned} A_1 U_{J_1} + A_2 U_{J_2} &= A_3 U_{J_3} \\ (A_1 U_{J_1}) U_{J_{1x}} + (A_2 U_{J_2}) U_{J_{2x}} &= (A_3 U_{J_3}) U_{J_{3x}} \\ (A_1 U_{J_1}) U_{J_{1z}} + (A_2 U_{J_2}) U_{J_{2z}} &= (A_3 U_{J_3}) U_{J_{3z}} \\ (A_1 U_{J_1}) U_{J_{1y}} + (A_2 U_{J_2}) U_{J_{2y}} &= (A_3 U_{J_3}) U_{J_{3y}} \end{aligned} \quad (5.26)$$

where  $A_1$ ,  $A_2$ ,  $A_3$  are the cross sectional areas of JET 1, JET 2 and the resulting merged jet, respectively.  $U_{J_1}$ ,  $U_{J_2}$ ,  $U_{J_3}$  are the jet velocities of JET 1, JET 2, and the resulting merged jet, respectively.

The center of the resultant jet is taken to be the average of the coordinates of the centerlines of JET 1 and JET 2 at the intersection. Selection of the cross sectional shape of the merged jets is discussed in a subsequent paragraph. Initial conditions for the merged jet are as follows:

$$Z = Z_I, \quad X = X_I, \quad U_J = U_{J_3} \quad \& \quad \frac{dx}{dz} = \frac{U_{J_{3x}}}{U_{J_{3z}}} \quad (5.27)$$

The envelope of the coalesced jet is next determined with the method described for the determination of the envelope for a single jet.

Selection of the shape of the initial cross-section of the merged jet is dependent upon the value the jet orientation angle  $\Omega$ . This angle is defined as the enclosed angle between the freestream velocity vector and the line joining the centers of the two jet exits. For jet orientation angles less

than 20 degrees, the jet cross section is assumed to be circular. For an orientation angle of 90 degrees, the cross section is assumed to be an ellipse with a minor to major axis ratio of 1/2. No functional relationship has been established for  $20^\circ < \Omega < 90^\circ$ .

The velocities induced by a two-jet configuration can now be determined by replacing each jet (including the coalesced jet) by its representative singularity distribution. The induced velocity components due to each singularity distribution are additive at every point of interest on the airframe.

### 5.1.2 INTERMEDIATE GROUND EFFECT

The Wooler program has been modified at Vought to include ground effects at intermediate altitude. This is done by letting the ground become an image plane. The computed flow field is assumed to be reflected by the image plane so the combination of real and imaginary flow fields yields zero normal velocity components at the image plane. This approach is similar to that proposed by Wooler in reference 5-5. Following is a discussion on the modifications necessary to do this calculation:

Elementary concepts for the intermediate altitude math model are shown in Figure 5-6. As the jet approaches the ground plane, the ground plane is assumed to be an image plane. An imaginary jet can be assumed to exist below the image plane. The induced velocity flow field is composed of the contributions due to the real jet and the imaginary jet. For the simple case shown in Figure 5-6, induced velocity components in the axial and vertical directions are  $u$  and  $v$  for the real jet; and  $u'$  and  $v'$  for the imaginary jet at the control point cp. Since the directions of  $v$  and  $v'$  are opposite, the sum of  $v$  and  $v'$  will be zero for control points on the ground plane (image plane).

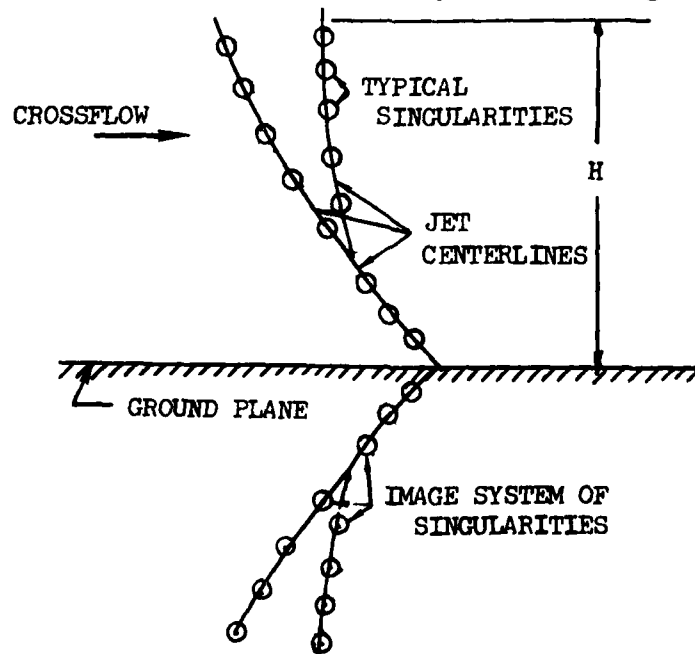


Figure 5-6 Image System for Ground Effect Ensures that the Ground is A Streamline

The Vought-Wooler-Ziegler intermediate altitude math model uses a system of imaginary control points instead of an imaginary jet. The induced velocity components at the control point (cp) due to the jet are  $u$  and  $v$ . The induced velocity components at the imaginary control point (cp') due to the jet are  $u'$  and  $v'$ . The velocity components at the real control point and at the imaginary control point are summed (i.e., add  $u'$  to  $u$  and subtract  $v'$  from  $v$ ) to obtain the combined solution.

The models used in the preceding discussions have been simplified by assuming the orientation parallel to the ground plane and treating only the  $x$  and  $y$  components of velocity. However, the basic concepts apply to any arbitrary orientation and to all three orthogonal velocity components. These relationships will be developed after a discussion of the coordinate systems used is given.

The Vought-Wooler-Ziegler jet flow field math model computer program input/output coordinate system is shown in Figure 5-7, and is denoted as XYZ. Basically, the X-direction is the direction of the aircraft tail, the Y-direction is along the right wing, and the Z-direction is up. The right hand sketch refers to the coordinate system used for locating the jet exhaust center and the relative direction of approach (onset) velocity vector,  $U_\infty$ . The left hand sketch shows the jet exhaust velocity vector ( $\vec{V}_J$ ) orientation. This coordinate system is used to input the jet location and the locations of the control points (cp) at which induced velocities are needed.

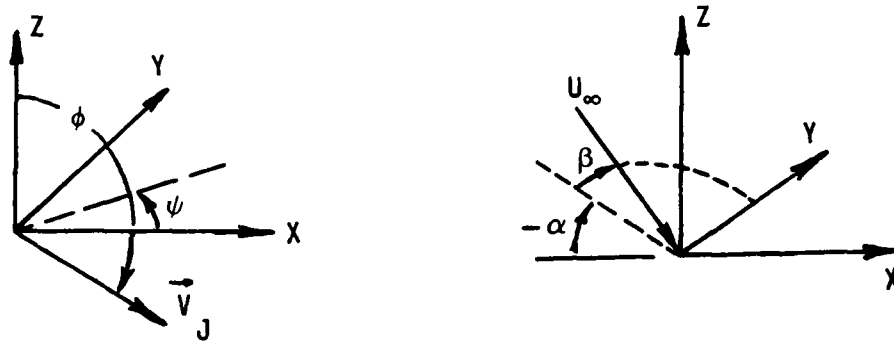


Figure 5-7. Input/Output Coordinate System

Internal to the computer program, the math model solution is obtained in a coordinate system called the Wooler fixed (WF) coordinate system. The relationship between the WF and input/output coordinate systems is listed below.

(5.28)

$$X_{WF} = X \quad Y_{WF} = Z \quad Z_{WF} = -Y$$

The intermediate altitude jet flow field math model is based on a coordinate system which is parallel to the ground plane. This coordinate system, see Figure 5-8, is the ground translated (GT) coordinate system. The XGT-ZGT plane of the GT coordinate system is parallel to the ground plane.

The jet induced velocity components at the real control point and at the imaginary control point must be expressed in the GT coordinate system so that they can be combined to yield the net velocity components.

The transformations between the Wooler fixed (WF) to the ground translated (GT) coordinate systems are based on the orientation angles shown in Figure 5-8.

The Wooler fixed coordinate system (airplane) is rotated through three angles

- Yaw angle,  $\psi$  (SIGMA)
- Pitch angle,  $\theta$  (THETA)
- Roll angle,  $\phi$  (FEE)

from the XGT, YGT, ZGT coordinate system. The XGT, YGT, ZGT. Coordinate system is assumed parallel to the ground plane, XG, YG, ZG.

The lift jet geometry and induced velocities are computed in the Wooler fixed (WF) coordinate system. Therefore, the induced velocity components must be computed at the real control point (cp) and at the imaginary control point (cp') in the WF coordinate system. The results are then transformed to the GT-system, combined, and transformed back to the WF-system.

The lift jet math model determines the induced velocity components at any arbitrary control point (cp) in terms of the WF coordinate system. To find the induced velocity components at the imaginary control point (cp'), Figure 5-8, the WF coordinates of cp' must be used. These coordinates are found with the following transformations:

- o Transform coordinates of control point cp from WF to GT coordinate system

$$X2_{CP} = X_{WF_{CP}} \quad (5.29)$$

$$Y2_{CP} = Y_{WF_{CP}} \cos \phi + Z_{WF_{CP}} \sin \phi$$

$$Z2_{CP} = Z_{WF_{CP}} \cos \phi - Y_{WF_{CP}} \sin \phi$$

$$X1_{CP} = X2_{CP} \cos \theta + Y2_{CP} \sin \theta$$

$$Y1_{CP} = Y2_{CP} \cos \theta - X2_{CP} \sin \theta$$

$$Z1_{CP} = Z2_{CP}$$

$$XGT_{cp} = X1_{cp} \cos \psi - Z1_{cp} \sin \psi$$

$$YGT_{cp} = Y1_{cp}$$

$$ZGT_{cp} = Z1_{cp} \cos \psi + X1_{cp} \sin \psi$$

- o Find coordinate of imaginary control point cp' in the GT coordinate system

$$XGT_{cp'} = XGT_{cp} \quad (5.30)$$

$$YGT_{cp'} = -(2h + YGT_{cp})$$

$$ZGT_{cp'} = ZGT_{cp}$$

- o Transform coordinates of imaginary control point cp' from GT to WF coordinate system

$$X1_{cp'} = XGT_{cp'} \cos \psi + ZGT_{cp'} \sin \psi \quad (5.31)$$

$$Y1_{cp'} = YGT_{cp'}$$

$$Z1_{cp'} = ZGT_{cp'} \cos \psi - XGT_{cp'} \sin \psi$$

$$X2_{cp'} = X1_{cp'} \cos \theta - Y1_{cp'} \sin \theta$$

$$Y2_{cp'} = Y1_{cp'} \cos \theta + X1_{cp'} \sin \theta$$

$$Z2_{cp'} = Z1_{cp'}$$

$$XWF_{cp'} = X2_{cp'}$$

$$YWF_{cp'} = Y2_{cp'} \cos \phi - Z2_{cp'} \sin \phi$$

$$ZWF_{cp'} = Z2_{cp'} \cos \phi + Y2_{cp'} \sin \phi$$



The lift jet math model is then used to compute the induced velocity components at the imaginary control point,  $cp'$ , with coordinates  $X_{WFcp'}$ ,  $Y_{WFcp'}$ ,  $Z_{WFcp'}$ . The induced velocity components at the control point in the three orthogonal directions are denoted as  $U_{WF}$ ,  $V_{WF}$ , and  $W_{WF}$ . For the imaginary control point these velocity components are  $U'_{WF}$ ,  $V'_{WF}$ , and  $W'_{WF}$ . Both sets of velocity components must be transformed to the GT coordinate system before the components can be combined. The transformation of the velocity components can be performed by equation 5.29. After the real and imaginary velocity components are combined, the resultant components are transformed from the GT to the WF coordinate system by equation 5.31.

The intermediate altitude part of the routine is used only when the ratio of altitude to nozzle exit diameter is less than 25 and should not be used for ratios less than 5.

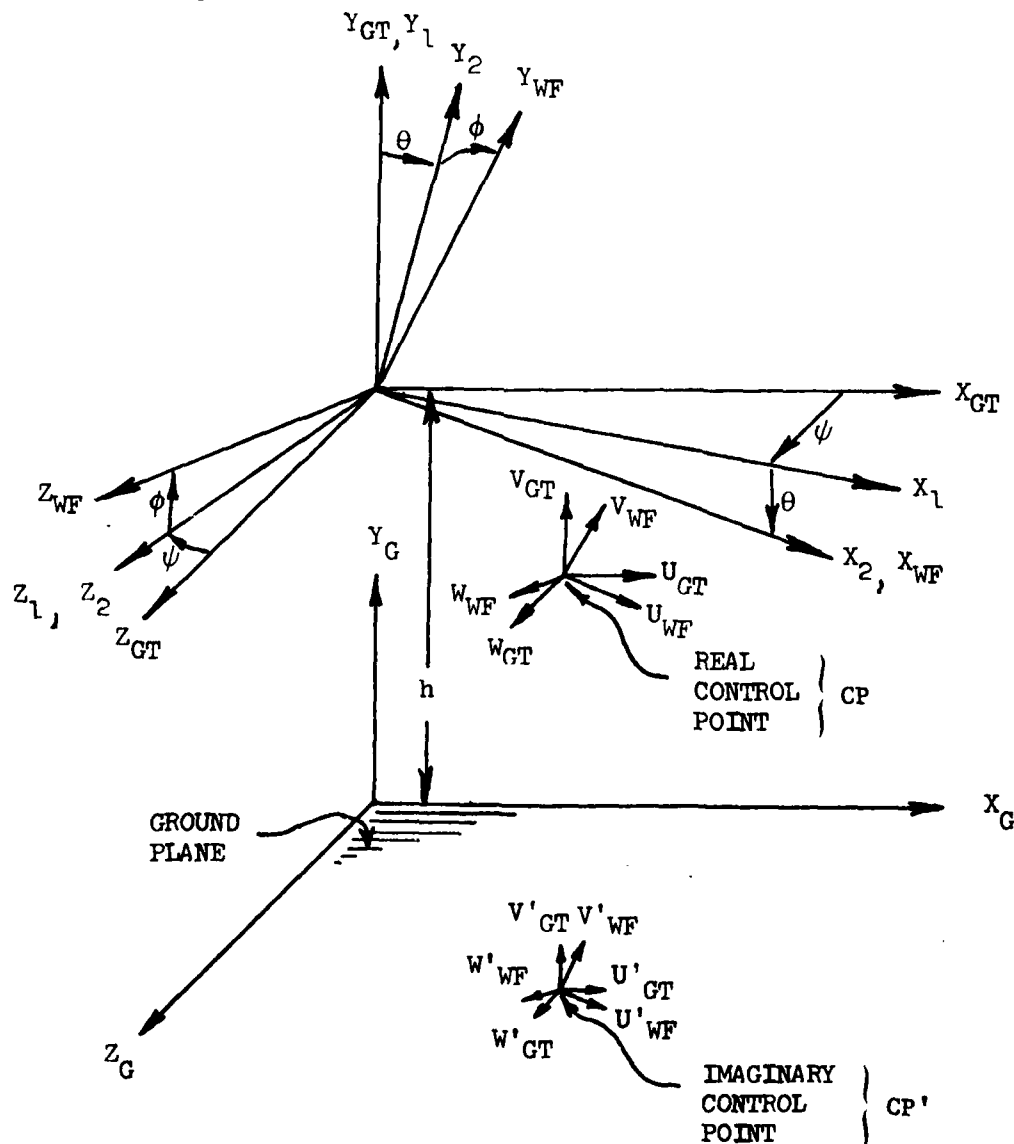


FIGURE 5.8. Intermediate Altitude Coordinate Transformation Model

## 5.2 VOUGHT/WESTON JET MODEL

As discussed earlier, the flow field produced by a jet issuing into a cross flow is dominated by two factors: (1) the jet entrainment and (2) the flow produced by a pair of contrarotating vortices formed by the shearing action between the relative wind and the jet. Woolers method discussed previously does a reasonable job of simulating the jet induced effects, but does not directly model the contrarotating vortices. Instead Wooler placed singularities which simulated the vortex pair, along the jet centerline rather than along the true vortex trajectories. In addition, Wooler's singularity strengths were obtained from assumptions concerning the growth of the jet plume rather than from an experimental description of the actual vortex pair.

Recently Fearn and Weston (reference 5.6) have obtained experimentally a very good quantitative description of the vorticity associated with a jet in a crossflow. This data was used by Seller's, reference 5.9, to formulate a mathematical model of the vortex flow. Dietz, reference 5.7, used these two results to develop a method for predicting jet induced effects on a flat plate. Dietz's method was limited to a 90 degree jet injection angle, one valve of jet velocity ratio, R, and one jet.

The method contained in Vape was developed at Vought using the above references in addition to a recent report by Fearn, reference 5.10 on jet injection angle effects. This method is applicable to various injection angles, various values of R and to multiple jets. A description of the Vought developed model is presented in the following discussion.

The method based on the above references uses the experimental data to define a diffuse vortex model which assumes that the distribution of vorticity within each of the contrarotating vortices is Gaussian in nature. The vorticity at any point is assumed to be given by

$$\omega(r_1) = \omega_0 e^{-\beta^2 r_1^2} \quad \text{and} \quad \omega(r_2) = -\omega_0 e^{-\beta^2 r_2^2}$$

where  $\omega_0$  is the maximum vorticity in the cross section, and  $\beta$  is the diffusivity of the vortices. Figure 5.9 defines the geometric parameters used.

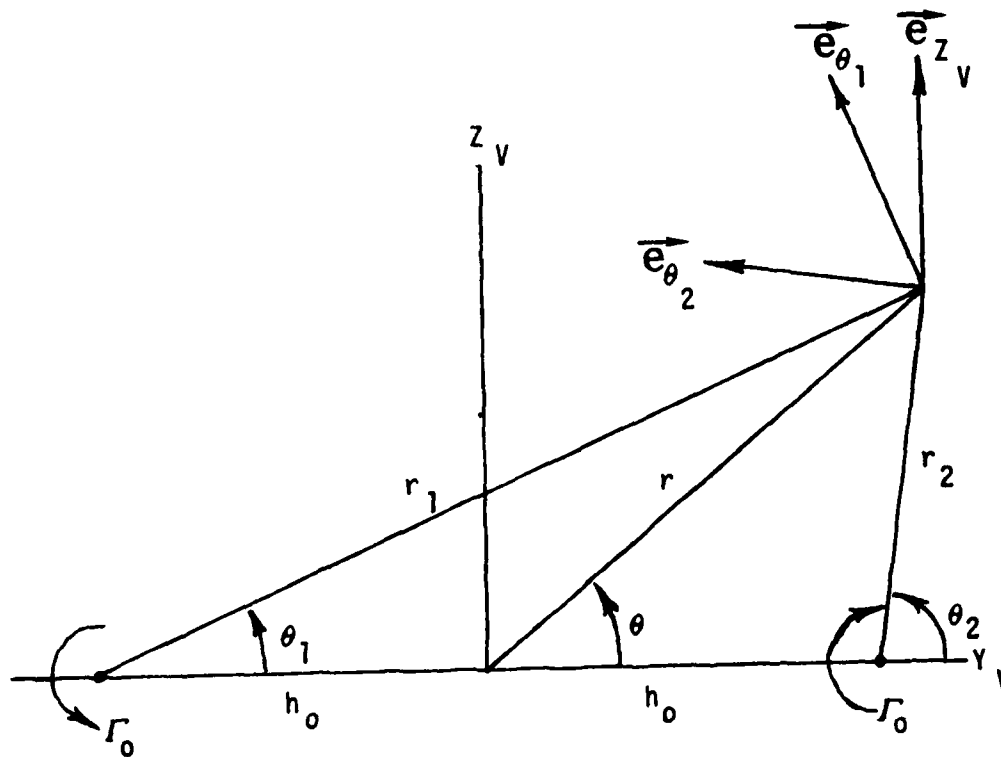


Figure 5.9 Geometry of Vortex Models

The integrated strength of each vortex distribution is defined as

$$\Gamma_0 = \int_0^{2\pi} \int_0^{\infty} \omega_0 e^{-\beta^2 r^2} r dr d\theta \quad (5.33)$$

The effective strength of each vortex is defined as the net flux of vorticity across the half plane of the cross section.

$$\Gamma = \int_{-\pi/2}^{\pi/2} \int_0^{\infty} \omega(r, \theta) r dr d\theta \quad (5.34)$$

where

$$\omega(r, \theta) = \omega_0 (e^{-\beta^2 r_1^2} - e^{-\beta^2 r_2^2}) \quad (5.35)$$

The center of vorticity (the effective half spacing),  $h$ , is defined by

$$h = \frac{1}{\Gamma} \int_{-\frac{\pi}{2}}^{\frac{\pi}{2}} \int_0^{\infty} \gamma_V \omega(r, \theta) r dr d\theta \quad (5.36)$$

Evaluation of these integrals relates the effective half spacing and strength of the vortices to the parameters of the vortex model. The resulting expressions are:

$$\Gamma = \Gamma_0 \operatorname{erf}(\beta h_0) \quad h = h_0 / [\operatorname{erf}(\beta h_0)] \quad (5.37)$$

$$\text{where} \quad \operatorname{erf}(\beta h_0) = \frac{2}{\sqrt{\pi}} \int_0^{\beta h_0} e^{-t^2} dt$$

It was observed from the test data that the vortex strength  $\Gamma_0$  was not a function of  $S/D$  but could be expressed as a linear function of  $R$ ,

$$\frac{\Gamma_0}{2DU_{\infty}} = AR \quad (5.38)$$

where  $A$  is a constant equal to .72.

The above equations represent a description of the strength and spacing of the vortex pair, but contain two parameters,  $\beta$  and  $h_0$  which must be defined for the equations to be in closed form. Sellers, reference 5.9 formulated relationships for  $\beta$  and  $h_0$  as a function of  $S/D$  and  $R$  given by:

$$\beta D = \frac{B}{\sqrt{S/D}} \quad (5.39)$$

$$\frac{h_0}{D} = C \left( 1 - e^{-\frac{S/D}{R}} \right) \quad (5.40)$$

Where  $B = 2.11$  and  $C = 2.04$

Fearn and Weston, reference 5.6, formulated relationships for the jet centerline path and the vortex curve for a 90 degree jet injection angle, in a jet exit coordinate system (defined in Figure 5.10), of the form.

$$\frac{Z}{D} = aR^b (X/D)^c \quad (5.41)$$

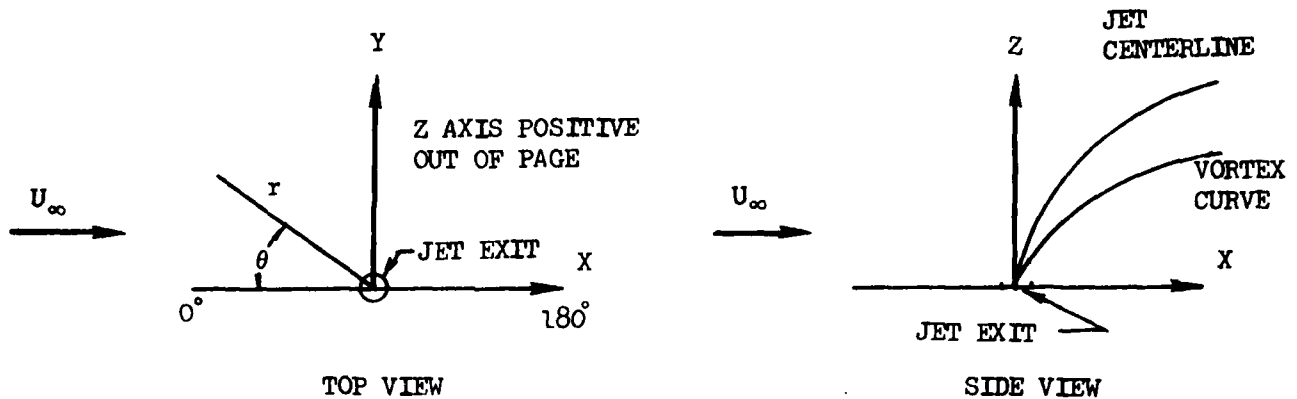


Figure 5.10 Jet Exit Coordinate System Defined

In addition, for the jet centerline only, there is a jet core region defined where the jet deflection is negligible. The length of this jet core depends on both  $R$  and  $\delta$ . For a coflowing jet the accepted value for the length of the jet core is about 7 jet diameters. For perpendicular jet injection, the jet core length decreases with decreasing jet to crossflow velocity ratio,  $R$ . Therefore a relationship was proposed that is an elliptic variation between these two values which gives for the jet core length ( $S_0$ ), the following expression.

$$S_0(R, \delta) = \frac{\ell_2(R)}{1 - (1 - \frac{\ell_2}{\ell_1}) \cos \delta} \quad (5.42)$$

where

$$\ell_2(R) = \ell_1 e^{-d^2/R^2} \quad \text{and} \quad \frac{\ell_1}{D} = 7$$

Equations 5.41 and 5.42 along with the definition of  $a$ ,  $b$ ,  $c$ ,  $d$  given in Table 5.1 provides the relationships needed to determine the jet centerline path and the vortex curve in the  $X - Z$  plane.

Table 5.1

Curve	a	b	c	d
Jet Centerline	1.2583	0.620	0.406	8.8951
Vortex Curve	0.3067	1.1513	0.4492	--

The lateral spacing,  $y$ , for the vortex curve is given by equation 5.37, (h).

Fearn, Krausche and Weston, reference 5.10, modified this equation based on further wind tunnel results, to account for injection angles other than  $90^\circ$ . The equation formulated is quite similar and is given by,

$$\frac{Z - Z_1}{D} = aR^b \left( \frac{X - X_1}{D} \right)^c \quad (5.43)$$

This curve is defined as being the same shape as the  $90^\circ$  degree injection curve but displaced from the origin of the jet exit coordinate system. Figure 5.11 shows a schematic that is applicable on both the jet centerline and the vortex curve showing the relationship between  $(X_1, Z_1)$  and  $(X_0, Z_0)$  and  $\delta_J$ . By definition,  $(X_0, Z_0)$  is the point where the tangent of the curve is the injection angle  $\delta_J$  and  $X_1, Z_1$ , is the point where the curve is perpendicular to the crossflow.

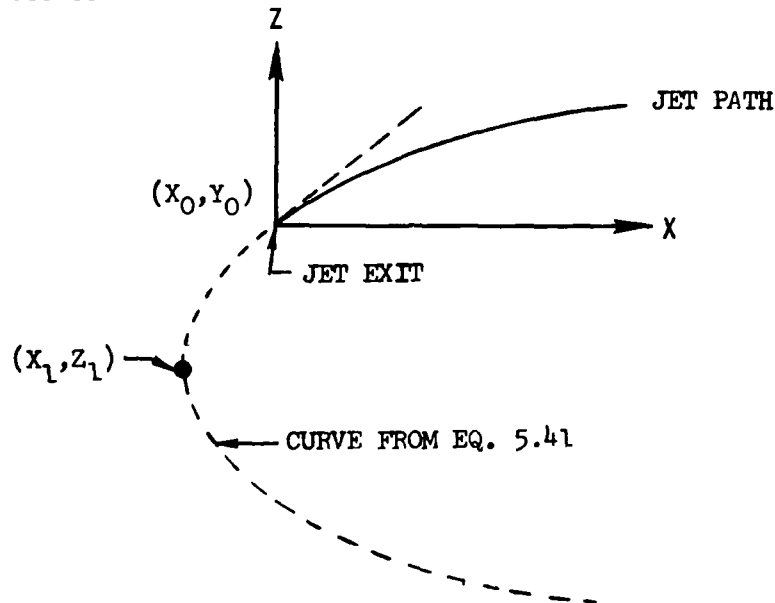


Figure 5.11. Schematic of Relationship Between  $(X_1, Z_1)$ ,  $(X_0, Z_0)$  and  $\delta_J$

## 5.2.1 FORMULATION OF THE JET MODEL

The vortices are modeled in VAPE by a distribution of finite filament vortices placed along the vortex trajectories described by equation 5.43 and 5.37. The strengths of the finite filaments are given by equation 5.37. Although the vortices are diffuse in the actual case of a jet in a crossflow, it is assumed that the velocity induced at a field point by a filament vortex will be indistinguishable from the velocity induced by a diffuse vortex, as long as the distance from the filament is large compared to the radius of the diffuse core. Since the diffuse vortices are observed to vary in strength along the vortex curve as a result of diffusion of vorticity across the symmetry plane, the strengths of the filament vortices are varied as a function of S/D in the computer model. Although this is inconsistent with Helmholtz's Laws, it should be emphasized that the filament vortices are used for analytical convenience and are modeling a diffuse vortex pair, for which there are no restrictions regarding the variation in strength along the vortex trajectories.

The distribution of filament vortices is composed of finite straight line segments. Enough vortex segments are generated such that the addition of more segments results in negligible velocity changes at the plane of the flat plate.

A distribution of line sinks is placed along the experimentally determined jet centerline, defined by equation 5.43. Although little data is available concerning entrainment by a jet in a crossflow, experimental and theoretical analyses are available for a free jet which provide a basis for estimating the amount of entrainment by a deflected jet and thereby establishing the strengths of the line sinks.

The free jet is described in terms of two regions, each characterized by different cross sectional velocity profiles (5.11). The first region, the zone of establishment, begins at the jet orifice and is idealized as a jet core, characterized by a flat velocity profile, surrounded by a turbulent fluid. The core is roughly conical in shape, and diminishes in cross sectional area along the jet centerline as a result of shear produced by the differing mean velocities of the jet and the surrounding fluid. When the core disappears (at some S/D defined as the critical length), the flow is said to be fully established, and is characterized by a velocity profile roughly Gaussian in nature.

Albertson (reference 5.11) conducted a theoretical analysis of a free jet and formulated relationships for the entrainment in the zone of establishment and in the region of established flow. Albertson found that the ratio of cross sectional jet volume flux to volume flux at the jet orifice increased in a parabolic form

$$\frac{Q}{Q_0} = 1 + 0.083\left(\frac{S}{D}\right) + 0.0128\left(\frac{S}{D}\right)^2 \quad (5.44)$$

in the zone of establishment. In the zone of established flow, the relationship is linear

$$\frac{Q}{Q_0} = 0.32 \left( \frac{S}{D} \right) \quad (5.45)$$

It is convenient to express the amount of entrainment in terms of an entrainment coefficient E

$$E = \frac{1}{Q_0} \frac{dQ}{d(S/D)} \quad (5.46)$$

Using Albertson's relationships, the entrainment coefficient may be expressed

$$E_e = .083 + .0256 \left( \frac{S}{D} \right) \quad (5.47)$$

in the zone of establishment, and

$$E = .32 \quad (5.48)$$

for established flow. The constant entrainment coefficient of 0.32 for a fully developed jet has been confirmed by Ricou and Spaulding (reference 5.12) and Saha (reference 5.13).

A free jet entrains surrounding fluid primarily through turbulent shear resulting from the difference in velocity of the jet and the surrounding fluid. The entrainment mechanism is considerably more complex in the case of a jet in a crossflow. Keffer (reference 5.14) states that a jet in a crossflow entrains surrounding fluid not only through turbulent shear, but also through the effects of free stream and vortex upwash components perpendicular to the jet trajectory. In addition, increased shear at the boundary of the jet resulting from the presence of the crossflow results in a more rapid degradation of the jet core and a decrease in the critical length.

Because of the lack of experimental data concerning entrainment by a jet in a crossflow, it is necessary to attempt to qualitatively estimate the entrainment coefficient E for use in the computer model. It is logical to assume that the entrainment coefficient E will be larger than 0.32, the value for a free jet. It is assumed that E is constant for a fully established deflected jet, based on observations of free jets.



The strength density of the line sinks is expressed in terms of the change in jet volume per unit length  $S/D$ , or

$$q = \frac{dQ}{d(S/D)} \quad (5.49)$$

Relations for  $q$  for a jet in a crossflow were found by assuming

$$\frac{Q}{Q_0} = K_1 + K_2 \left(\frac{S}{D}\right) + K_3 \left(\frac{S}{D}\right)^2 \quad (5.50)$$

for the zone of establishment, and

$$\frac{Q}{Q_0} = K_4 \left(\frac{S}{D}\right) \quad (5.51)$$

for established flow. These relations are of the same form as Albertson's equations for free jets. By definition

$$E = \frac{1}{Q_0} \frac{dQ}{d(S/D)} = K_4 \quad (5.52)$$

The coefficients  $K_1$ ,  $K_2$ , and  $K_3$  are found by applying boundary conditions. It is assumed that  $Q=Q_0$  at  $S/D=0$ ,  $\frac{1}{Q_0} \frac{dQ}{d(S/D)} = 0$  at  $S/D=0$ , and  $\frac{1}{Q_0} \frac{dQ}{d(S/D)}$  is continuous at the critical length. Equations 5.50 and 5.51 then become

$$\frac{Q}{Q_0} = 1 + \frac{1}{2} \frac{E}{(S_c/D)} (S/D)^2 \quad (5.53)$$

for the zone of establishment, and

$$\frac{Q}{Q_0} = E \frac{S}{D} \quad (5.54)$$

for established flow. From these relationships, the strength density  $q$  may be written

$$q = \frac{EQ_0(S/D)}{S_c/D} \quad (5.55)$$

in the zone of establishment, and

$$q = EQ_0 \quad (5.56)$$

for established flow. The amount of entrainment is therefore defined by establishing values for  $E$  and  $S_c/D$ . From Keffer (reference 5.14) and Fearn (reference 5.15), the critical length  $S_c/D$  is equal to about 3 for a velocity ratio of 8. This value, although approximate, has more experimental basis than values of  $E$  for deflected jets. The value for  $E$  was adjusted until the model provided good overall correlation with the experimentally determined pressure distribution. The value of  $E$  used in VAPE is 0.6.

## 5.2.2 MULTIPLE JET ANALYSIS

The above approach has been modified at Vought to be applicable to multiple jets using a procedure similar to that employed by Wooler, as explained earlier. In this approach, the front jet in a jet pair is assumed to act independently of the aft jet, therefore the equation for both the jet centerline and the vortex curves as well as the associated singularity strengths for a single jet are used. For the aft jet, it is assumed that the front jet alters the dynamic pressure field into which the aft jet issues. A description of the variation in the dynamic pressure as a function of jet spacing was given in the discussion on Wooler's technique and is applicable to this model also.

Using the experimental data on which Wooler based his multiple jet method, reference 5.16, a modification was obtained to the equation of the aft jet's penetration that produced excellent agreement with this data. The equation obtained for the aft jet is given by.

$$\frac{Z - Z_1}{D} = a(R')^b \left(\frac{x-x_1}{D}\right)^c \quad (5.57)$$

where  $a$  and  $b$  are given in Table 5.1 and  $c$  is set equal to .4 for the jet centerline calculation. The value of  $c$  for the vortex curve is left unchanged due to a lack of experimental data upon which to base any modification. The value  $R'$  is a jet velocity ratio based on the reduced freestream dynamic pressure at the aft jet.  $R'$  is determined in the program by the following relationship

$$R' = R \left(\frac{V_\infty}{V_\infty'}\right) \quad (5.58)$$

where  $V_\infty'$  is determined from either equation 5.24 or 5.25 in the Wooler discussion.

Figure 5.12 presents a comparison of the jet centerline locations as calculated by the above approach to those calculated by Wooler's method and to the experimental data. The above technique gives a good description of the jet centerline and the vortex curves for a two jet system.

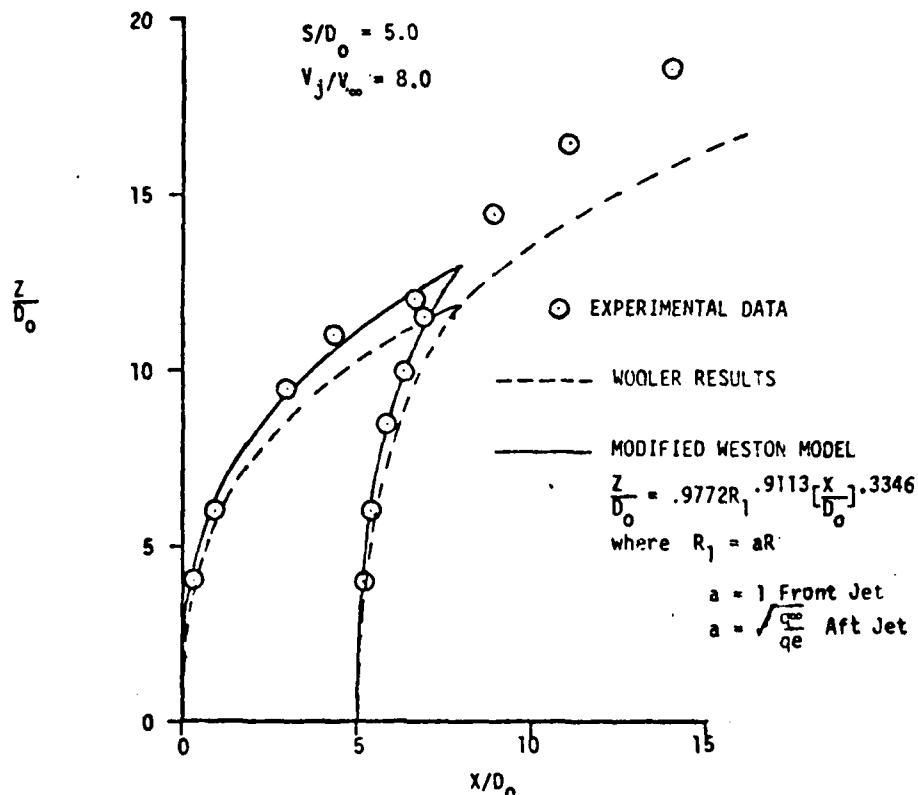


Figure 5.12 Comparison of calculated and experimental jet path centerlines, jet spacing = 5.0 diameters, jet velocity ratio,  $R = 8$

The question which now arises is what happens if these two jets intersect as shown in Figure 5.12. Wooler uses a technique for merging the two jets in his method which suggests a method for use in the approach presented above. Wooler used continuity and momentum considerations to develop a merged jet as discussed earlier. This same approach is used in the Weston model contained in VAPE with some changes. The approach taken in this model requires that the area and velocity of both jets at the intersection point are known. For the Weston model these values are determined in the following manner.

Fearn and Weston, reference 5.6, gives a relationship for the radius of the vortex core,  $r_c$ , of the diffuse vortices. This expression is

$$\frac{r_c}{D} = 1.121 \frac{\beta}{D} \quad (5.59)$$

where  $\beta$  is the diffusion constant presented earlier. Now  $\frac{\beta}{D}$  has been shown to be given by the relation

$$\frac{\beta}{D} = \frac{2.11}{\sqrt{S/D}} \quad (5.60)$$

Therefore the radius of the vortex core at the intersection is

$$R_c = \left\{ \frac{1.121}{(2.11/\sqrt{S/D})} \right\} D \quad (5.61)$$

where D is the jet exit diameter

Now the distance between the vortex core centerline is given by the lateral spacing of the vortices.

$$HIV = \frac{HM}{\text{erf}[(\beta/D)(HM)]} \quad (5.62)$$

$$\text{where } HM = 2.04 \left\{ 1 - e^{-\frac{S/D}{R}} \right\}$$

Therefore the area of the vortex is defined, by use of Figure 5.13, to be

$$AREA_{JET} = \pi R_c^2 + R_c HIV \quad (5.63)$$

The area for the front and aft jets are determined in this manner.

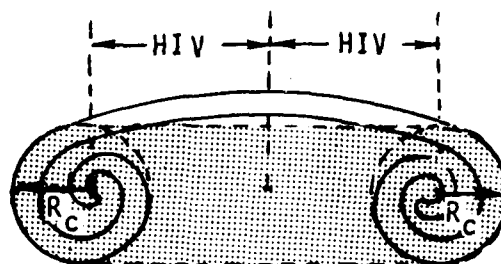


Figure 5.13 Schematic of Vortex Flow Field For Determining Area

The other quantity which is needed is the velocity in each jet at the intersection point. Wooler in reference 5.16, measured the jet velocity decay in both a front and aft jet with various spacings between jets. Figure 5.14 presents a summary of this data plotted as a dynamic pressure ratio versus surface distance along the jet centerline path. The following equation was derived based on a linear regression fit of the data for a single jet or a leading jet in a two jet system.

$$\text{Log } \frac{q_J}{q_{J_{\text{EXIT}}}} = -2.80732 \text{ LOG}(S/D) + 1.55754 \quad (5.64)$$

Since this is compressible flow this can be reduced to:

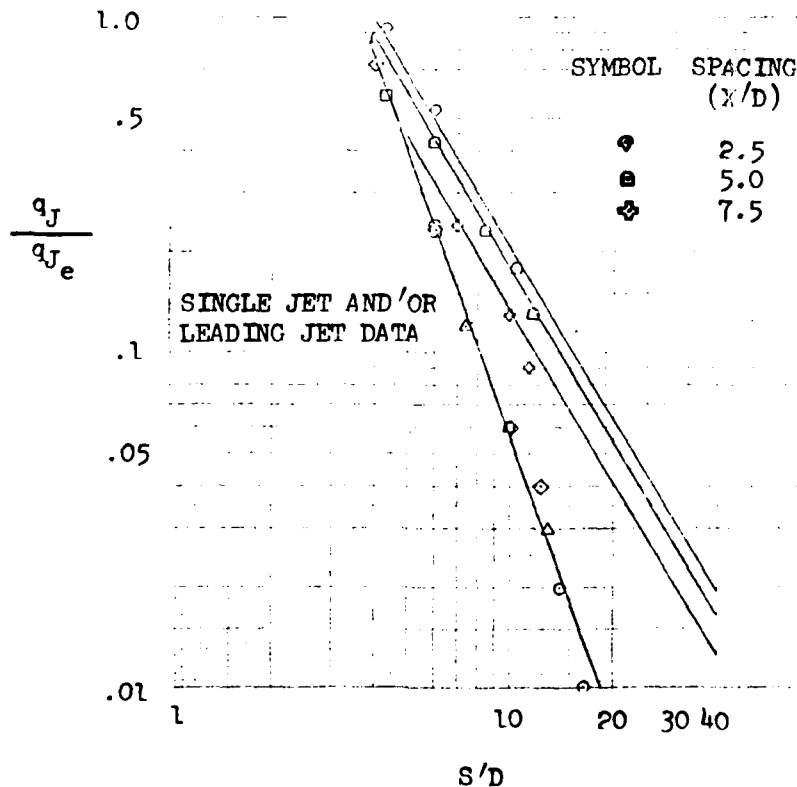


Figure 5.14 Jet Velocity Decay

$$\frac{V_J}{V_{J\text{EXIT}}} = \sqrt{\frac{q_J}{q_{J\text{EXIT}}}} = \sqrt{10^{-2.80732 \text{ LOG}(S/D) + 1.55754}} \quad (5.65)$$

Therefore in terms of jet velocity ratio

$$\frac{V_J}{V_\infty} = R \sqrt{10^{-2.80732 \text{ LOG}(S/D) + 1.55754}} \quad (5.66)$$

This gives the jet velocity decay for the front jet. Thus if the intersection point is known then the velocity for the front jet can be calculated. As for the aft jet, it can be observed from Figure 5.14, e.c. That the jet decay is a function of surface distance and jet spacing. A similarly derived expression for the jet decay for the aft jet is given by

$$\frac{V_J}{V_\infty} = R' \sqrt{10^{[-.00451(\frac{L}{d_{01J}})^2 + .00914(\frac{L}{d_{01J}}) + 1.01772](\frac{S}{D})^{-1.7}}} \quad (5.67)$$

Now, with the jet velocity and the area of both jets at the intersection point, the continuity and momentum equation can be written as done in equation 5.26 in Wooler's analysis.

From the solution of the continuity and momentum equations the following relationships for the components of velocity of the merged jet are obtained:

$$\begin{aligned} XX1 &= (VJM1)(AJM1) \\ XX2 &= (VJM2)(AJM2) \end{aligned} \quad (5.68)$$

where VJM1, VJM2 are the jet velocities at the intersection point for jets 1 & 2 respectively, and AJM1, AJM2 are the corresponding jet areas.

$$\text{then } K = (AJM3)(VJM3) = XX1 + XX2 \quad (5.69)$$

where AJM3, VJM3 are the area and velocity for the merged jet at the intersection point.

Further let

$$\begin{aligned} VX1 &= (VJM1)(VX1M) & VX2 &= (VJM2)(VX2M) \\ VY1 &= (VJM1)(VY1M) & VY2 &= (VJM2)(VY2M) \\ VZ1 &= (VJM1)(VZ1M) & VZ2 &= (VJM2)(VZ2M) \end{aligned} \quad (5.70)$$

where  $VX1M$ ,  $VY1M$ ,  $VZ1M$  and  $VX2M$ ,  $VY2M$ ,  $VZ2M$  are the direction cosines at the intersection point of jets 1 and 2 respectively.

$$VJMX = [(XX1)(VX1) + (XX2)(VX2)]/K \quad (5.71)$$

$$VJMY = [(XX1)(VY1) + (XX2)(VY2)]/K$$

$$VJMZ = [(XX1)(VZ1) + (XX2)(VZ2)]/K$$

Thus,  $VJMX$ ,  $VJMY$  and  $VJMZ$  are the velocities of the merged jet at the intersection point. Then (5.72)

$$\begin{aligned} VJM3 &= (VJMX^2 + VJMY^2 + VJMZ^2)^{\frac{1}{2}} \\ \text{and } AMJ3 &= \frac{K}{VJM3} \end{aligned}$$

so now the velocity at the merged jet and its area (diameter) is known at the initial point (intersection pt). In order to define a curve for the jet path centerline from this point the jet velocity ratio,  $R_3$  and the jet injection angle  $\delta_3$  are needed. Let  $R_3$  be defined as

$$R_3 = \frac{VJM3}{V_\infty \sin \delta_3} \quad (5.73)$$

and  $\delta_3$  is defined by the direction cosines of the velocity vector given by Equation 5.71

This definition for  $R$  is used because only the component of the freestream velocity perpendicular to the jet stream will effect the jet penetration.

Then equation 5.57 is used for the merged jet centerline path location with the values of the constants being:  $a = 1.2583$ ,  $b = .62$ ,  $c = .406$ . The vortex curves are not merged and are allowed to extend to some downstream location. This is not physically correct since they should merge and change



considerably. But since no data is available upon which to base a model, they were left alone. The model even with this anomaly gives very good results for multiple jets as compared to experiment as will be shown in a later section of this report.

The multiple jet method discussed above is for jets mounted in tandem. Consider the case of jets mounted side by side as shown in Figure 5.4(a). This is a typical arrangement, when a jet is located on each side of the fuselage. In the Vought/Wooler jet model both of these jets are modeled even though we may be using a plane of symmetry in the Hess program. This technique is necessary so that the effect of both jets are determined. In the Vought/Weston program, a problem may arise if both jets are modeled. Each jet has a set of contrarotating vortices which flow downstream from the jet exit. If the jets are far enough apart and not too close to the airplane centerline then the model proposed should give reasonable results. However, most configurations of interest have the nacelles fairly close to the plane of symmetry and thus relatively close to each other. In this case, a problem arises in the Vought/Weston model, in that the inboard vortices from each jet may intersect at some point downstream of the jet exit. In real life, these vortices will merge and could possibly cause the vortices to break up. Unfortunately, there is no test data available to indicate exactly how the interaction effects the vortex parameters. In the current jet model, when the inboard vortex crosses the plane of symmetry, the presence of this additional vortex on each side of the fuselage produces very large induced velocities. Since these additional vortices would not exist in real life, this use of the model is not at all representative of the configuration. Therefore, in the Vought/Weston method contained in VAPE, if side-by-side jets on opposite sides of the fuselage are to be analyzed, then the following procedure must be used. The configuration must be analyzed with a plane of symmetry, i.e., only one-half of the configuration is input. Then, in the jet model, only one jet is input. This must be the jet contained on the side of the configuration input. If this procedure is followed the results obtained, as shown in Section 7.2, are very good.

Recommendations will be presented later which would improve the Vought/Weston jet model and remove the above problem.

### 5.2.3 STOL CALCULATIONS

The jet methods discussed so far are for the transitional area of flight which was defined as the regime between normal horizontal flight and vertical hovering. There are several methods which have been developed for the vertical hovering region, references 5.17 and 5.18. One area which has not been considered, is the STOL region of flight which is defined as the region where the aircraft is taking off or landing and is very close to the ground, at a reasonable forward speed. The lift jets are deflected such that they impinge the ground forming wall jets, which are not being reflected back to the aircraft. The wall jets increase entrainment and thus increase the "suck-down" effect of the jets on the aircraft. A technique to predict this effort has been developed and incorporated into the Weston jet model contained in the VAPE program. The details of this approach are given below.

Consider a V/STOL aircraft with its lift jets deflected moving close to the ground as shown in Figure 5.15. The jet flow between the aircraft and the ground plane is assumed to be represented by the flow model in the Weston jet model. When the jet intersects the ground, an impingement region is formed where the jet flow direction is changed to be parallel to the ground plane, forming a radial wall jet. A radial wall jet in a cross-flow creates a rather complex flow field. At some distance ahead of the jet impingement point, the flow along the wall jet separates from the wall and curves back on itself. The focii of these separation points is referred to as the separation line of the wall jet.

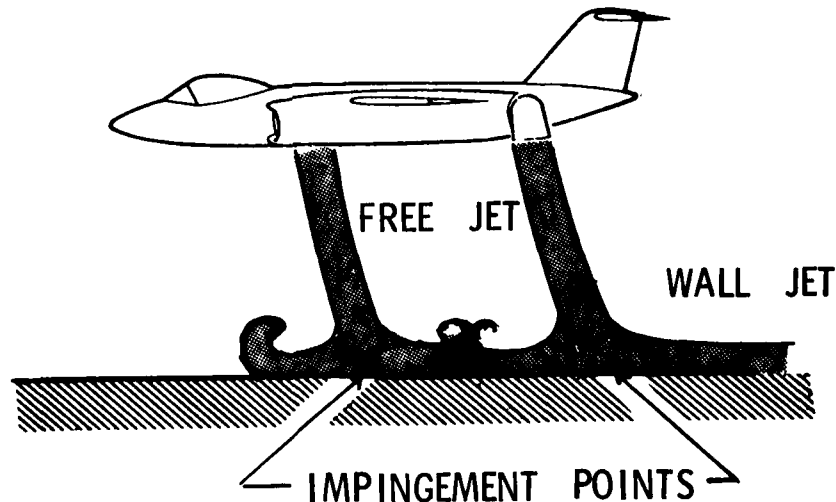


Figure 5.15 Aircraft in STOL Flight Regime

A strong vortex is formed between the source of the wall jet and the separation line of the two flows.

In the approach used in VAPE, the separation line is modeled, but the Vortex is ignored. The algorithm used in VAPE is to (1) determine the impingement point; (2) define the wall jet; (3) find the separation line, and (4) determine the entrainment due to the wall jet aft of the separation line. These entrainment values are then used to calculate a normal velocity at control points on the ground plane which are used as boundary conditions in the Hess program.

The jet impingement location is determined by finding the intersection point of the ground plane with the jet centerline path.

Once the impingement point is found then the velocity of the jet at this point can be determined from equations 5.66 or 5.67. In addition, the angle of the jet relative to the ground plane at impingement must be determined for the wall jet analysis. This angle is calculated in the following manner.

$$\alpha_{JET_{IM}} = \tan^{-1} \left( \frac{dz}{dx} \right)_{JET_{IM}} \quad (5.74)$$

where  $\alpha_{JET_{IM}}$  = IMPINGEMENT ANGLE

$\left( \frac{dz}{dx} \right)_{JET_{IM}}$  = tangent of jet centerline path at impingement point

The separation line may now be determined based on an empirical equation developed by Colin, reference 5.19. This technique requires a new jet velocity ratio to be defined,  $R_\lambda$ , as the ratio of dynamic pressures at the impingement point.

This ratio based on prior reasoning is simply a velocity ratio given by

$$R_\lambda = \frac{V_{JET_{IM}}}{V_{\infty LOCAL}} \quad (5.75)$$

where  $V_{JET_{IM}}$  = JET IMPINGEMENT VELOCITY

$V_{\infty LOCAL}$  = Cross Flow Velocity at Impingement Point

In Colins report an assumption is made that the energies of the wall jet and main stream flows must be equal at the separation line. The energy of the wall jet over a small arc  $ds$  can be represented by

$$dE_{WJ} = \frac{1}{2} \rho \left[ \int_0^{\delta_m} U^3 dy + \int_{\delta_m}^{\delta+\delta_m} U^3 dy \right] ds \quad (5.76)$$

But if we assume

$$\frac{U}{U_m} = \left( \frac{y}{\delta_m} \right)^{\frac{1}{n}} \quad n = 7 \quad (5.77)$$

Then

$$dE_{WJ} = \frac{1}{2} \rho \left[ x_1 U_0^3 K_3 \frac{1}{\left( \frac{x}{x_r} \right)^{2.3}} \right] ds \quad (5.78)$$

Where  $K_3$  is a constant which can be determined from the slope of the inner and outer layers and the rate of growth of the wall jet.

The energy for the external stream in the plane of symmetry is given by

$$dE_{\infty} = \frac{1}{2} \rho \left[ U_{\infty}^3 (\delta + \delta_m) ds \right] = \frac{1}{2} \rho \left[ (K_1 + K_2) x U_{\infty}^3 ds \right] \quad (5.79)$$

The energy ratio is therefore

$$\frac{dE_{WJ}}{dE_{\infty}} = \frac{x_1 U_0^3 K_3 \frac{1}{\left( \frac{x}{x_r} \right)^{2.3}}}{(K_1 + K_2) x U_{\infty}^3} = \frac{K_3}{K_1 + K_2} \left( \frac{U_0}{U_{\infty}} \right) \left( \frac{x_r}{x} \right)^{3.3} \quad (5.80)$$

Now let the energy ratio = 1

$$\text{then } \frac{K_3}{K_1 + K_2} \left( \frac{U_0}{U_{\infty}} \right) \left( \frac{x_r}{x} \right)^{3.3} = 1 \quad (5.81)$$

gives

$$\frac{x_s}{x_r} = \frac{3.3}{\sqrt{\frac{K_3}{K_1 + K_2}}} R_{\lambda}^{0.9} \quad (5.82)$$

or

$$\frac{x_s}{x_r} = K R_{\lambda}^{0.9} \quad (5.83)$$

This concept can be used to determine the separation line on the wall rather simply by considering the potential flow of a plane source in a uniform stream. The matching condition indicated above for the interaction region in the plane of symmetry is used to determine the equivalent source strength. If  $\Lambda$  is the source strength, the equation of the dividing streamline is given by

$$\frac{\Lambda}{2\pi} \text{ARCTNG } \frac{Y}{X} - U_{\infty} Y = 0 \quad (5.84)$$

where  $Y$  is a coordinate on the base plate, perpendicular to the  $x$  axis.

For  $y=0$ , the separation point in the plane of symmetry is given by

$$X_S = \frac{\Lambda}{2\pi U_{\infty}} \quad (5.85)$$

But from equation 5.83 we have

$$\frac{X_S}{D} = KR_{\lambda}^{0.9} \quad \text{so} \quad KR_{\lambda}^{0.9} = \frac{\Lambda}{2\pi U_{\infty}} \quad (5.86)$$

$$\text{and } \Lambda = 2\pi U_{\infty} KR_{\lambda}^{0.9} D \quad (5.87)$$

$$\text{but } R_{\lambda} = \frac{V_{JET IM}}{U_{\infty}} \quad (5.87)$$

$$\text{so } \Lambda = 2\pi D U_{JET IM} \frac{K}{R_{\lambda}^{0.1}} \quad (5.88)$$

But  $2\pi D U_{JET IM}$  is assumed to be the equivalent starting mass flow of the wall jet

$$M_{WJ} = 2\pi D U_{JET IM} = 2\pi D U_{J EXIT} \frac{R_{\lambda}}{V_J/U_{\infty}} = M_J \frac{R_{\lambda}}{V_J/U_{\infty}} \quad (5.89)$$

where  $M_j$  is the actual flow from the nozzle relating the source strength to the actual mass flow from the nozzle.

$$\Lambda = M_j \frac{R_\lambda}{V_j/U_\infty} \frac{K}{R_\lambda^{0.1}} \quad (5.90)$$

$$\text{so } \Lambda = \frac{M_j K R_\lambda^{0.9}}{V_j/U_\infty} \quad (5.91)$$

$$\text{and } x_s = \frac{K M_j R_\lambda^{0.9}}{2 \pi U_\infty (V_j/U_\infty)} \quad (5.92)$$

The equation of the separation line on the base plate becomes

$$K R_\lambda^{0.9} D \text{ ARCTG } \frac{Y}{X} - y = 0 \quad (5.93)$$

$$\text{or } 1.03 R_\lambda^{0.9} D \text{ ARCTG } \frac{Y}{X} - Y = 0 \quad (5.94)$$

$K = 1.03$  based on experimental data correlations

Figure 5.16 presents a comparison of this calculated curve on a flat plate for a  $R_\lambda$  of 28.5 with experimental data.

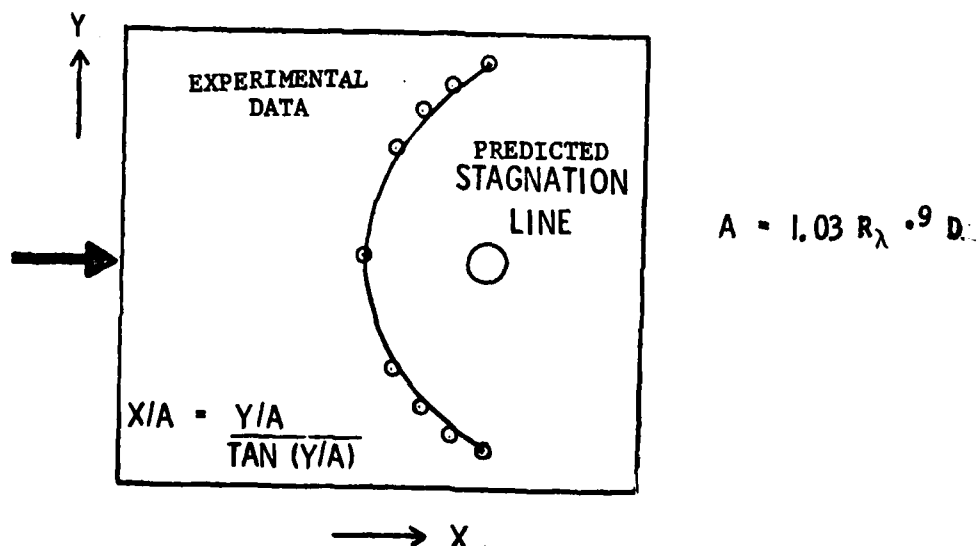


Figure 5.16. Schematic of Model Utilized for STOL Calculations in VAPE

The entrainment due to the wall jet at every control point aft of the separation line must now be determined. These entrainment rates are determined in VAPE by a method based on the technique presented in reference 5.17, developed for a wall jet in a static pressure field. Colin, in reference 5.19 indicates that the wall jet does not change appreciably in terms of size or entrainment when a freestream flow is added as long as the velocity of the crossflow is small. Therefore for application to the analysis method in VAPE the approach of reference 5.17 should give a reasonable approximation to the wall jet effect.

A full description of the approach is discussed in reference 5.17, so only the pertinent equations and their derivation will be discussed below.

The total mass flow in the radial wall jet in an azimuthal sector between the angle  $\theta_B$  and  $\theta_A$  is the following:

$$\dot{m}[(\theta_B - \theta_A), R] = \rho_m \int_{\theta_A}^{\theta_B} \int_0^{\infty} V_{MAX} \left( \frac{U}{U_{MAX}} \right) R N_5 \left( \frac{dN}{N_5} \right) dQ \quad (5.95)$$

where  $\theta_A$  &  $\theta_B$  are the extents of the angular section.

$V_{MAX}$  is the maximum velocity in the wall jet at the sector

$R$  is the radius

$N_5$  is the normal distance above the ground plane to  $V_{MAX}/2$

Now  $V_{MAX}$  is defined as

$$V_{MAX}(R) = \frac{R_I}{R} V_{MAX_I} \quad (5.96)$$

where the subscript I refers to the impingement region.

and  $I_M^*$  is defined as

$$I_M^* = \int_0^{\infty} \left( \frac{U}{U_{MAX}} \right) d\left(\frac{N}{N_5}\right) \quad (5.97)$$

Then equation 5.95 can be written as

$$\frac{\dot{m}}{\rho_m} [(\theta_B - \theta_A), R] = N_5 I_M^* R_I \int_{\theta_A}^{\theta_B} V_{MAX_I} d\theta \quad (5.98)$$

Now  $N_5(R)$  is defined as

$$N_5(R) = N_{5I} + .07 (R - R_I) \quad (5.99)$$

and  $V_{MAX_I}$  is

$$V_{MAX_I} = V_{JET_{IM}} \left[ 0.55 + .170(FI) \right] \left[ 1 - 0.4(FI) \sin \frac{\theta}{2} \right] \quad (5.100)$$

$$\text{where } FI = \frac{90^\circ - \alpha_{JET_{IM}}}{15^\circ}$$

$$\text{Then } \frac{\dot{m}}{\rho_m} \left[ (\theta_B - \theta_A), R \right] = R_I I_M V_{JET_{IM}} \left[ N_{5I} + .07(R - R_I) \right] \left[ 0.55 + .17(FI) \right] \quad (5.101)$$

$$\times \int_{\theta_A}^{\theta_B} \left[ 1 - 0.4(FI) \sin \frac{\theta}{2} \right] d\theta$$

Now the entrained mass between successive radii  $R_A, R_B$  is

$$\frac{\dot{m}}{\rho_m} \left[ (\theta_B - \theta_A), R_B \right] - \frac{\dot{m}}{\rho_m} \left[ (\theta_B - \theta_A), R_A \right] = \frac{\dot{m}_{\text{entrained}}}{\rho_{\text{ambient}}} \quad (5.102)$$

This last term is the volume flow rate of entrained flow per unit area of the wall jet surface assuming the surface is parallel to the ground plane gives

$$A_{\text{SURFACE}} = \int_{R_A}^{R_B} \int_{\theta_A}^{\theta_B} R dR d\theta = \frac{R_B^2 - R_A^2}{2} (\theta_B - \theta_A) \quad (5.103)$$



$$V_N = \frac{0.14 R_I V_{JET_{IM}} I_m^* [0.55 + .170 (F1)]}{(R_B + R_A) (\theta_B - \theta_A)} \times \int_{\theta_A}^{\theta_B} [1 - .4(F1) \sin \frac{\theta}{2}] d\theta \quad (5.104)$$

The integral in this equation can be evaluated and when this is done we obtain

$$V_N = \frac{.07 R_I}{R} V_{JET_{IM}} I_m^* [.55 + .17(F1)] [1 - .4(F1) \sin \frac{\theta}{2}] \quad (5.105)$$

now  $\frac{\theta}{2}$  must be positive for this equation

also  $I_m^* \approx 0.98$

This volume of  $V_N$  is calculated at every control point on the ground plane and used as a boundary conditions in the Hess solution to simulate the effects of the wall jet entrainment.

#### 5.2.4 WAKE EFFECT MODEL

Several different approaches were tried to simulate the wake region in the Vought/Weston jet model. The techniques considered all made use of additional singularities added to the jet model in the wake region. Unfortunately, no method was developed which would improve the results in the wake area without effecting the results in a negative fashion in the rest of the flow field. Therefore, the VAPE method currently contains no model which will treat the wake region correctly. This will pose a problem when considering jets which have a surface directly behind the jet, i.e., a nose jet. But, it is felt, based on results obtained, that this effect is nominally fairly small and will not penalize the methods too severely.

### 5.3 THAMES RECTANGULAR JET MODEL

A method has been developed, reference 5-8, to calculate the propulsive induced effects produced by an aspect ratio 4 rectangular jet orientated with the major axis either parallel or perpendicular to the crossflow. The approach selected parallels that used by Weston and Dietz, reference 5-6 and 5-7. This choice required that an extensive data base be generated to define the vortex strengths for the two nozzle orientation and various jet-to-freestream velocity ratios and nozzle injection angles that the model was to simulate. Thames thus conducted a test phase to generate the required data base and then used this data base to develop the analytical math model. Following is a fairly detailed description of Thames model condensed from reference 5-8.

The model has two principal components.

- o A pair of variable strength potential filament vortices lying along the experimentally determined vortex trajectories.
- o One or more source/sink lines lying along (and parallel to) the experimentally determined jet centerline curve.

The vortices are included to model the real contrarotating vortex pair. The vortex strength distributions were determined from the experimental data. The source/sink lines are used to simulate the blockage/entrainment of the jet. Since there was no direct experimental procedure for measuring the source/sink strengths, these were determined by trial and error to give the best approximation to the experimentally measured flat plate pressure distributions. The induced velocity calculated by the model may be written as

$$\vec{V}(x,y,z) = \vec{V}_V(x,y,z) + \vec{V}_S(x,y,z) \quad (5.106)$$

where  $V_V(x,y,z)$  is the velocity induced at the point  $(x,y,z)$  by the variable strength vortices and  $V_S(x,y,z)$  is the velocity induced by the source/sink lines. The computation procedures for  $V_V$  and  $V_S$  are explained in detail in the next two sections.

#### 5.3.1 VORTEX SIMULATION

Since the strength of each filament vortex varies along its path, each vortex is subdivided into a specified number of constant strength vortex segments,  $N_{VS}$ , as illustrated in Figure 5-17. The segment lengths are cubically stretched to compensate for the rapid variation in  $\Gamma$  immediately downstream of the jet exit.

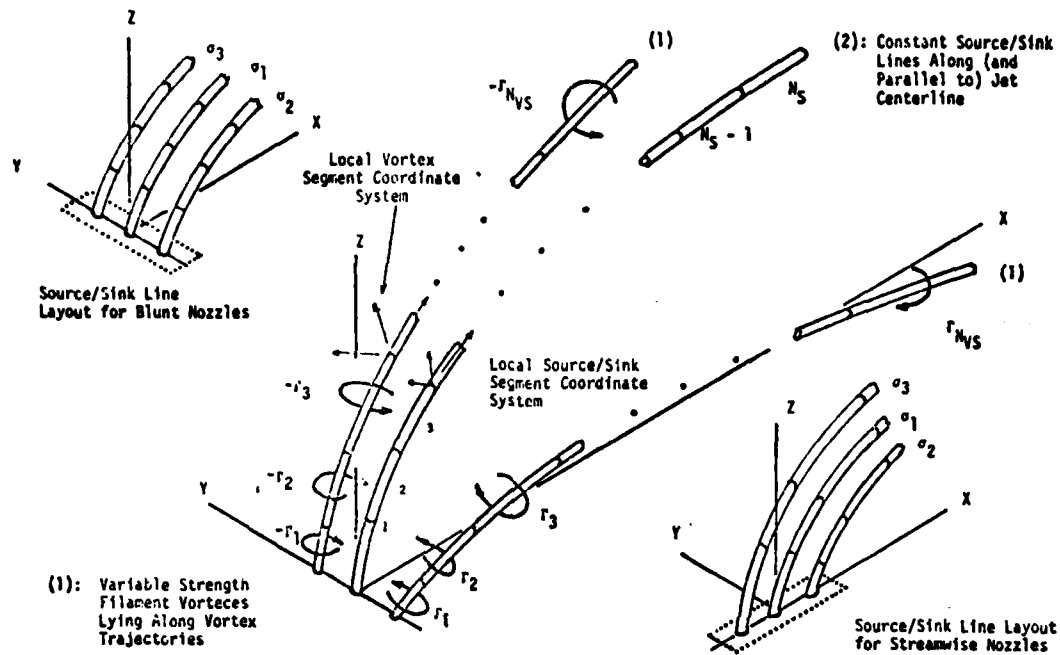


Figure 5-17. Schematic of Rectangular Jet Model Formation

The strength of each segment, say  $\Gamma_i$ , is taken to be the average of the strengths at the segment end points. That is,

$$\overline{\Gamma_i} = \frac{\Gamma_i + \Gamma_{i+1}}{2}, \quad 1 < i < N_{VS} \quad (5-107)$$

The  $\Gamma_i$  values are determined by interpolating the strength data obtained from the wind tunnel tests. In this interpolation  $\Gamma_i$  is treated as a function of three independent variables--distance downstream of the jet exit, velocity ratio, and jet injection angle.

The velocities induced by each constant strength segment are calculated from the Biot-Savart Law. Let  $X_{K,L}$ ,  $Y_{K,L}$ ,  $Z_{K,L}$  be the coordinates of the Kth control point with respect to the local vortex segment coordinate system (Figure 5-17). Then the velocity induced at the point K by the ith segment of the jth vortex is

$$\begin{aligned} \vec{(v_{V_{K,L}})}_{i,j} &= (u_{V_{K,L}})_{i,j} \vec{i}_L + (v_{V_{K,L}})_{i,j} \vec{j}_L \\ &\quad + (w_{V_{K,L}})_{i,j} \vec{k}_L \end{aligned} \quad (5-108)$$

where the L subscript implies that the vector components are with respect to the local vortex segment coordinate system and  $i_L$ ,  $j_L$ , and  $k_L$  are the unit vectors in this system.

Then from the Biot-Savart Law

$$(u_{V_{K,L}})_{i,j} = 0 \quad (5.109)$$

$$(v_{V_{K,L}})_{i,j} = -\frac{\Gamma_{i,j}}{2\pi} \frac{z_{K,L}}{H_{K,L}} \bar{R}_{K,L} \quad (5.110)$$

$$(w_{V_{K,L}})_{i,j} = \frac{\Gamma_{i,j}}{2\pi} \frac{y_{K,L}}{H_{K,L}} \bar{R}_{K,L} \quad (5.111)$$

where

$$H_{K,L} \equiv y_{K,L}^2 + z_{K,L}^2 \quad (5.112)$$

$$\bar{R}_{K,L} \equiv -\frac{x_{K,L} - S_{V_i}}{R_2} + \frac{x_{K,L}}{R_1} \quad (5.113)$$

$$R_1 \equiv [x_{K,L}^2 + H_{K,L}]^{1/2} \quad (5.114)$$

$$R_2 \equiv [(x_{K,L} - S_{V_i})^2 + H_{K,L}]^{1/2} \quad (5.115)$$

$S_V$  is the length of vortex segment  $i$  (segment lengths are the same on both  $i$  vortices) and  $\Gamma_{i,j}$  is the associated strength of the segment. In general, none of the local segment coordinate systems will be parallel as the vortex trajectory is curved. Therefore, since we wish to sum the velocities induced by all vortex segments of both vortices, it is necessary to express the induced velocities in some common coordinate system. In this effort, the jet exit coordinate system is used. Let  $T_{i,j}^V$  be the proper rotation matrix.

The velocity induced at K by segment i of the jth vortex in the jet exit coordinate system is then

$$(\vec{v}_{V_K})_{i,j} = \underline{T_{i,j}^V} (\vec{v}_{V_K,L})_{i,j} \quad (5.116)$$

The total velocity induced by a single vortex at K is

$$\begin{aligned} (\vec{v}_{V_K})_j &= \sum_{i=1}^{N_{VS}} (\vec{v}_{V_K})_{i,j} \\ &= \sum_{i=1}^{N_{VS}} \underline{T_{i,j}^V} (\vec{v}_{V_K,L})_{i,j} \end{aligned} \quad (5.117)$$

so that the total velocity induced at point K by both vortices is

$$\vec{v}_{V_K} = \sum_{j=1}^2 \left[ \sum_{i=1}^{N_{VS}} \underline{T_{i,j}^V} (\vec{v}_{V_K,L})_{i,j} \right] \quad (5.118)$$

where  $N_{VS}$  is the number of vortex segments per vortex. The double sum given by Equation 5.118 is carried out for all control points. The velocity induced by the two vortices at all control points is

$$\vec{v}_V = \sum_{K=1}^{N_{CP}} \left\{ \sum_{j=1}^2 \left[ \sum_{i=1}^{N_{VS}} \underline{T_{i,j}^V} (\vec{v}_{V_K,L})_{i,j} \right] \right\} \quad (5.119)$$

where  $N_{CP}$  is the number of control points.

The calculations outlined above require that the vortex trajectories be known. These trajectories were measured during the test program. The trajectory is calculated as follows: Based on user input, the model generates an array of cubically stretched trajectory abscissas using the equation

$$x_{V_i} = L_V \left( \frac{i-1}{N_{VS}} \right)^3, \quad 1 < i < N_{VS} + 1 \quad (5.120)$$

where  $L_V$  is the distance downstream of the jet exit that the vortex flows are assumed to propagate (usually,  $L_V = 20 - 30$ ). The velocities induced by these portions of the vortex flows beyond  $L_V$  are neglected by the model. The  $Z_V$  coordinates are obtained from the vortex curve fit equations. That is

$$Z_{V_i} = a_V R^{b_V} (X_{V_i} + X_{o_V})^{c_V} - Z_{o_V}, \quad 1 < i < N_{V_S} + 1 \quad (5.121)$$

where

$$X_{o_V} = \left[ \frac{\text{TAN } \delta_e}{a_V R^{b_V}} \right]^{\frac{1}{c_V - 1}} \quad (5.122)$$

$$Z_{o_V} = a_V R^{b_V} X_{o_V}^{c_V}$$

$$\text{and } \delta_e = 90 + d(90 - \delta_j) + e(90 - \delta_j)^2$$

The parameters  $a_V$ ,  $b_V$ ,  $c_V$ ,  $d_V$  and  $e_V$  are given in Table 5.2. The lateral coordinate,  $h$  (or  $Y_V$ ), of the trajectory is obtained by interpolation of the vortex spacing data obtained during the tests. In these interpolations  $h$  is assumed to be a function of three independent variables--distance downstream of the jet exit, velocity ratio, and jet deflection angle. After the trajectory is calculated, the vortex segment lengths,  $S_{V_i}$ , are computed using

Nozzle Configuration	Curve	a	b	c	d	e	RMS Error
Blunt	Vortex	0.2105	1.2368	0.4131	-0.09306	-.02681	0.315 D
	Jet Centerline	0.7947	0.9120	0.3190	0.02458	-.02351	0.276 D
Streamwise	Vortex	0.9378	0.8109	0.3394	-0.1383	0.0	0.161 D
	Jet Centerline	1.5405	0.7345	0.3293	-0.2486	0.0	0.320 D

Table 5.2. Vortex and Jet Centerline Curve Fit Parameters

$$S_{V_1} = \left[ (x_{V_1} - x_{V_{1-1}})^2 + (y_{V_1} - y_{V_{1-1}})^2 + (z_{V_1} - z_{V_{1-1}})^2 \right]^{1/2} \quad (5.123)$$

for

$$1 < i < N_{VS} + 1$$

## 5.3.2 SOURCE/SINK SIMULATION

To simulate the blockage/entrainment effects of the jet, the model uses one or more segmented source/sink lines lying along (or parallel to) the experimentally determined jet centerline (Figure 5-17). The source/sink strength along a given line is constant. However, if more than one line is used, the strengths may vary from line to line. In addition, if multiple lines are used, the strengths must be symmetric about the symmetry plane (only an odd number of lines is allowed) for blunt oriented jets. However, non-symmetric strengths may be used for streamwise oriented nozzles. As mentioned before, the number and strengths of the source/sink lines was determined by a trial and error procedure. The strength distributions are determined by interpolation in the model assuming that the source/sink strength,  $\sigma$ , is a function of nozzle orientation, velocity ratio, and jet incidence angle. However, the model does allow the user to specify these quantities if desired.

Using notation similar to that used in the previous section, the velocity induced at a point K by the  $i$ th segment of the  $j$ th source/sink line is

$$(\vec{V}_{S_{K,L}})_{i,j} = (U_{S_{K,L}})_{i,j} \vec{i}_L + (V_{S_{K,L}})_{i,j} \vec{j}_L + (W_{S_{K,L}})_{i,j} \vec{k}_L \quad (5.124)$$

where

$$(U_{S_{K,L}})_{i,j} = \frac{\sigma_j}{2\pi} \left( \frac{1}{R_2} - \frac{1}{R_1} \right) \quad (5.125)$$

$$(V_{S_{K,L}})_{i,j} = \frac{\sigma_j}{2\pi} \frac{Y_{K,L}}{H_{K,L}} \bar{R}_{K,L} \quad (5.126)$$

$$(W_{S_{K,L}})_{i,j} = \frac{\sigma_j}{2\pi} \frac{Z_{K,L}}{H_{K,L}} \bar{R}_{K,L} \quad (5.127)$$

with

$$H_{K,L} \equiv Y_{K,L}^2 + Z_{K,L}^2 \quad (5.128)$$



$$\bar{R}_{K,L} = -\frac{X_{K,L} - S_{S_{i,j}}}{R_2} + \frac{X_{K,L}}{R_1} \quad (5.129)$$

$$R_1 = [X_{K,L}^2 + H_{K,L}]^{\frac{1}{2}} \quad (5.130)$$

$$R_2 = [(X_{K,L} - S_{S_i})^2 + H_{K,L}]^{\frac{1}{2}} \quad (5.131)$$

These equations are quite similar to those developed for the vortex flows. However, the coordinates of point K (i.e.,  $X_{K,L}$ ,  $Y_{K,L}$ ,  $Z_{K,L}$ ) used here are the coordinates of the Kth control point in the local source/sink segment coordinate system (Figure 5-17). Again, we must transform the components given by (5.125) - (5.127) to the jet exit coordinate system. Thus,

$$(\vec{V}_{S_K})_{i,j} = \underline{T_{i,j}^S} (\vec{V}_{S_{K,L}})_{i,j} \quad (5.132)$$

where  $T_{i,j}^S$  is the appropriate rotation matrix. Summing over a single source/sink line, the velocity induced by that line at point K is

$$\begin{aligned} (\vec{V}_{S_K})_j &= \sum_{i=1}^{N_{SS}} (\vec{V}_{S_K})_{i,j} \\ &= \sum_{i=1}^{N_{SS}} \underline{T_{i,j}^S} (\vec{V}_{S_{K,L}})_{i,j} \end{aligned} \quad (5.133)$$

and the total velocity induced by all source/sink lines at K is

$$\vec{V}_{S_K} = \sum_{j=1}^{N_S} \left[ \sum_{i=1}^{N_{SS}} \frac{T_{i,j}}{r_{i,j}} \vec{V}_{S_{K,L}} \right]_{i,j} \quad (5.134)$$

where  $N_{SS}$  is the number of source/sink segments per line and  $N_S$  is the number of source/sink lines.

The source/sink line trajectories lie either along the jet centerline trajectory or parallel to it. Regardless of the number of lines used, one will always lie along the centerline path. The coordinates for this path are developed as follows: The model initially calculates a set of linearly stretched abscissas using

$$X_{S_i} = L_S \left( \frac{i-1}{N_{SS}} \right), \quad i=1, N_{SS} + 1 \quad (5.135)$$

where  $L_S$  is the distance downstream of the jet exit that the source/sink lines are assumed to exist (nominally,  $L_S = L_V$ ). The  $Z_S$  coordinates are obtained from the jet centerline curve fit equations. Thus,

$$Z_{S_i} = a_c R^{b_c} (X_{S_i} - X_{O_c})^{c_c} - Z_{O_c}, \quad 1 < i < N_{SS} + 1 \quad (5.136)$$

where  $X_{O_c}$  and  $Z_{O_c}$  are evaluated as indicated in the last section, the parameters  $a_c$ ,  $b_c$ ,  $c_c$ ,  $d_c$  and  $e_c$  are given in Table 5.2. Since the jet centerline lies in the symmetry plane, the  $Y_S$  array is simply

$$Y_{S_i} = 0, \quad 1 \leq i \leq N_{SS} + 1 \quad (5.137)$$

The source/sink segment lengths are then

$$S_{S_i} = [(X_{S_i} - X_{S_{i-1}})^2 + (Y_{S_i} - Y_{S_{i-1}})^2]^{1/2} \quad (5.138)$$

for  $2 \leq i \leq N_{SS} + 1$ . If there are more than one source/sink line, the trajectories depend upon the nozzle orientation (i.e., blunt or streamwise). Each case is covered separately below.

Blunt Orientation

This case is illustrated in Figure 5-18. Each additional pair (recall that the number of source/sink lines,  $N_S$ , must be an odd number) is displaced a constant distance,  $\Delta$ , on either side of a central source/sink line. Therefore, the  $X_S - Z_S$  distributions given by Equations (5.135) and (5.136) are appropriate for the additional source/sink lines and the lateral displacement arrays are given by

$$Y_{S_{i,j}} = (-1)^j M \Delta, \quad \begin{matrix} 1 \leq i \leq N_{SS} + 1 \\ 2 \leq j \leq N_S \end{matrix} \quad (5.139)$$

where  $M$  is the somewhat peculiar function

$$M = \begin{cases} j/2, & j \text{ even} \\ \frac{(j-1)}{2}, & j \text{ odd} \end{cases} \quad (5.140)$$

and  $\Delta$  is given by

$$\Delta = \frac{[\pi A_R]^{1/2}}{2(N_S + 1)} \quad (5.141)$$

$A_R$  is the nozzle aspect ratio. The segment lengths given by Equation (5.138) are valid for all additional source/sink lines.

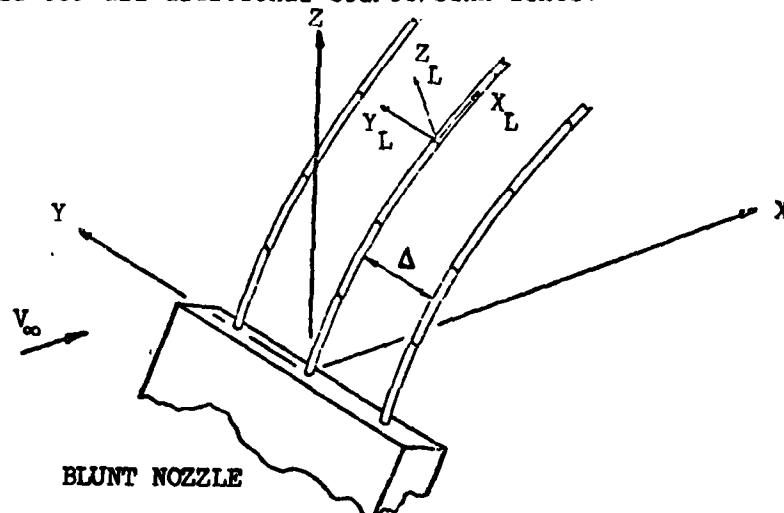


Figure 5-18. Multiple Source/Sink Lines for Blunt Nozzles

Streamwise Orientation

This case is somewhat more complicated as evidenced by the drawing given in Figure 5-19. The basic idea is that the additional source/sink lines be parallel to the line lying along the jet centerline trajectory and spaced a constant distance  $\Delta$  from it. The lateral spacing distribution given by Equation (5.137) is obviously valid for all additional source/sink lines. The variation of  $X_S$  and  $Z_S$  for each additional sink line is

$$X_{S_{i,j}} = X_{S_{i,1}} + \Delta'_j \sin \theta_{c_i} \quad (5.142)$$

$$Z_{S_{i,j}} = Z_{S_{i,1}} - \Delta'_j \cos \theta_{c_i} \quad (5.143)$$

for  $1 \leq i \leq N_{SS} + 1$  and  $2 \leq j \leq N_S$  and where

$$\Delta'_j \equiv (-1)^j M \Delta \quad (5.144)$$

with  $M$  given by (5.140) and  $\Delta$  by (5.141).  $\theta_{c_i}$  is the local slope of the jet centerline curve and is given by

$$\theta_{c_i} = \tan^{-1} \left\{ a_c C_c R^{b_c} (X_{S_{i,1}} + X_{0_c})^{C_c - 1} \right\} \quad (5.145)$$

$X_{S_{i,1}}$  and  $Z_{S_{i,1}}$  are the coordinates of the central source/sink line given by Equations (5.135) and (5.136) respectively. The source/sink segment length arrays are then

$$S_{S_{i,j}} = [(X_{S_{i,j}} - X_S)^2 + (Z_{S_{i,j}} - Z_{S_{i-1,j}})^2]^{1/2} \quad (5.146)$$

for  $1 \leq i \leq N_{SS} + 1$  and  $2 \leq j \leq N_S$ .

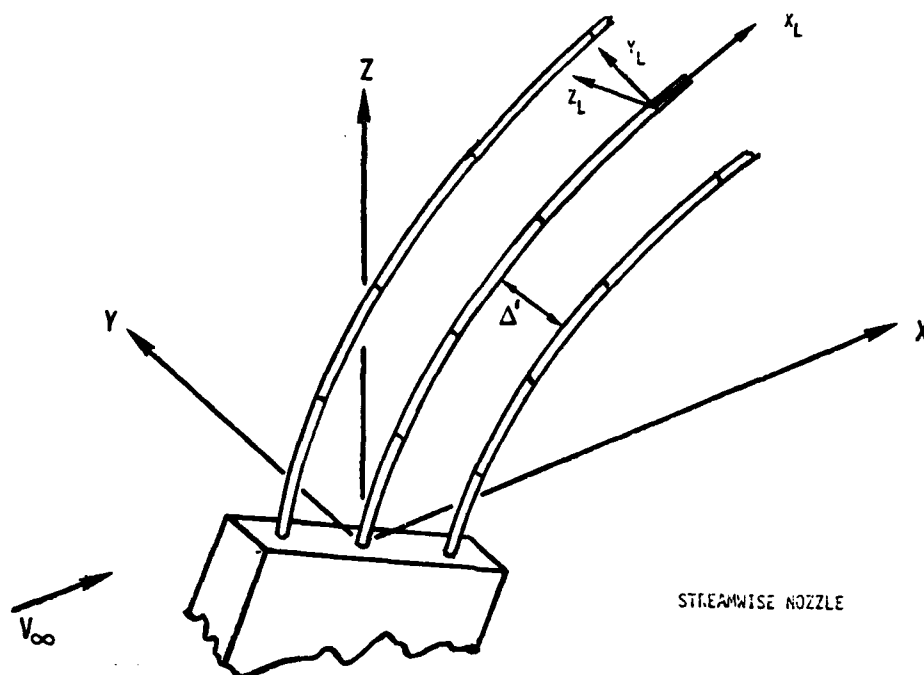


Figure 5.19. Multiple Source/Sink Lines for Streamwise Nozzles

The total velocity induced by the model is the vector sum of velocity induced by both the vortex and source/sink flows. Thus, from Equation (5.106)

$$\vec{V}_J = \vec{V}_V + \vec{V}_S$$

Using Equations (5.19) and (5.135)

$$\begin{aligned} \vec{V}_J = & \sum_{k=1}^{N_{CP}} \left( \sum_{j=1}^2 \left[ \sum_{i=1}^{N_{VS}} T_{i,j}^V (\vec{V}_{V_{K,L}})_{i,j} \right] \right) \\ & + \sum_{k=1}^{N_{CP}} \left( \sum_{j=1}^{N_S} \left[ \sum_{i=1}^{N_{SS}} T_{i,j}^S (\vec{V}_{S_{K,L}})_{i,j} \right] \right) \end{aligned} \quad (5.147)$$

In effect, this equation and those which describe the individual terms plus the supporting data base are the model.

### 5.3.3 MODEL APPLICABILITY

The jet model described in this section was based entirely on the tests described in reference 5.8. Technically speaking, the model is directly applicable only to the nozzle configurations and jet flow parameters bracketed by the test results. These conditions are:

- o Nozzle aspect ratio: 4.0
- o Nozzle equivalent diameter: 4.0 (in appropriate units)
- o Nozzle Orientations: Blunt, streamwise
- o Velocity Ratio:  $4 \leq R \leq 10$
- o Jet Deflection:
  - Blunt Nozzles:  $45^\circ \leq \delta_j \leq 90^\circ$
  - Streamwise Nozzles:  $75^\circ \leq \delta_j \leq 90^\circ$

The computer code allows input outside these bounds. In fact, the routine allows virtually any input (except that which is obviously erroneous such as  $R < 0$ ) and will execute. However, if the input conditions differ drastically from those listed above, the results may be meaningless (or, nearly so).

The model should give reasonable results for nozzle and jet flow conditions which differ only slightly from those given above. The following are suggested off-design limits for the model:

- o Nozzle aspect ratio:  $3.0 \leq A_R \leq 5.0$
- o Nozzle equivalent diameter:  $3.5 \leq D \leq 4.5$
- o Nozzle orientations: Blunt, streamwise
- o Velocity ratio:  $3.0 \leq R \leq 12.0$
- o Jet Deflection:
  - Blunt Nozzles:  $45^\circ \leq \delta_j \leq 90^\circ$
  - Streamwise Nozzles:  $60^\circ \leq \delta_j \leq 90^\circ$

## 6.0 INLET ANALYSIS METHOD

In order to properly model the entire flow field about a V/STOL aircraft, the effects produced by the flow entering the inlet and the forces and moments on the inlet itself must be determined. Several years ago, N.O. Stockman of NASA Lewis Research Center developed an analytical technique to calculate the flow in and around subsonic axisymmetric inlets, reference 6.1, including first order viscous effects. This approach was composed of an iterative solution of several computer programs including a compressible axisymmetric boundary layer program, reference 6.3. Stockman also developed a compressibility correction for the potential flow solution, reference 6.4. This technique provided a valuable tool for estimating the performance and optimizing lip shapes for V/STOL and conventional inlets. In Stockman's approach, the potential flow solution was performed and the resulting pressures on the internal surfaces were corrected for compressibility using the method of reference 6.4. These pressures along with the original geometry were then input to the boundary layer program to obtain the desired viscous parameters. The displacement thickness,  $\delta^*$ , was then added, by hand, to the original geometry and the process repeated to obtain the viscous effects on the flow field. It was evident at Vought, that the process could be made more efficient and flexible if these programs were unified into one computer program with the geometry modification being accomplished by the computer code. Consequently, these programs were combined into a single iterative computer code at Vought, reference 6.5. This code has proven to be an excellent way to screen preliminary inlet designs and thereby to reduce the scope of expensive inlet parametric test programs. Additionally, this code has been modified at Vought to calculate the inlet ram forces and moments.

Individual computer routines and methods of combination are described in Section 6.1. The modifications developed to permit calculation of inlet forces and moments are presented in Section 6.2. Section 6.3 presents a description of a study done to develop design charts for inlet boundary layer separation.

### 6.1 VOUGHT/STOCKMAN PROGRAM

A complete description of this method is given in the references cited above so only a brief description of the basic program formulation will be included in this report.

Solution of the basic problem involves calculation of the compressible viscous flow in an arbitrary axisymmetric inlet at any combination of operating conditions of free-stream velocity  $V_\infty$ , inlet incidence angle,  $\alpha$ , and inlet mass flow rate,  $\dot{W}$  (Figure 6-1). At non-zero incidence angle, flow in and around the inlet is three-dimensional. Since there were no exact practical three-dimensional compressible viscous flow methods of solution available, NASA-Lewis Research Center (NASA-LeRC) applied a series of four computer routines to obtain a pseudo-three dimensional solution.

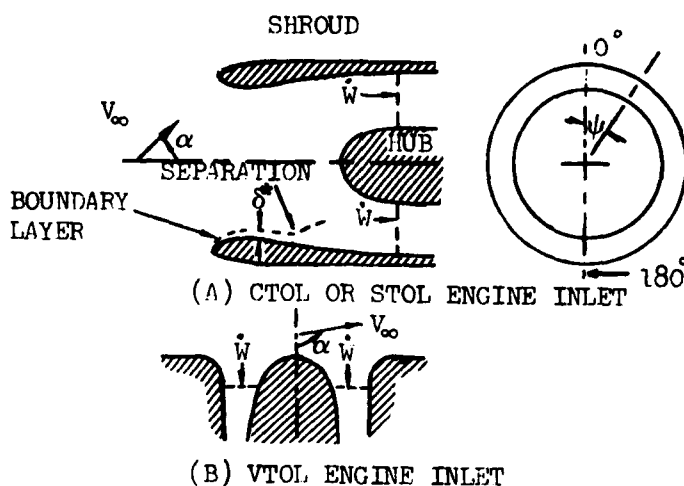


Figure 6-1. Inlet Configurations and Input Parameters for Flow Routines

The Vought subsonic inlet analysis flow routine is composed of the four NASA Lewis computer routines, reported by N. O. Stockman, reference 6-1, plus some linking and editing routines developed at Vought. Each of the major NASA Lewis routines are described in some detail in reference 6-1. Discussion of the individual components of the combined routine and the method of linking are described in the following sections.

#### POTENTIAL FLOW SOLUTION

The inlet potential flow solution is obtained by the first three Stockman routines - SCIRCL, EOD, and COMBYN. Description of these three routines follows.

##### 6.1.1 GEOMETRY REPRESENTATION

The inlet is assumed to be axisymmetric and is represented by its meridional profile. This profile is divided into segments at convenient tangent points. Each segment is defined by an analytic expression. The inlet walls and outer surface (nacelle or bellmouth) must be extended far downstream to insure accurate potential flow solutions in the inlet region of interest. The geometry routine (SCIRCL) prepares coordinate point input for efficient use by the potential flow routine and also prints out information such as surface curvature, wall angles, and flow area distribution. SCIRCL is a convenient and effective tool for preparing the input for the potential flow program from a minimum set of input data.

##### 6.1.2 INCOMPRESSIBLE POTENTIAL FLOW SOLUTIONS

The Hess axisymmetric program (EOD) is used for calculating the incompressible potential flow (reference 6-2). The program utilizes a distribution of sources or sinks of initially unknown strength to represent the inlet profile. This model results in an integral equation which is exact for a continuous distribution of source strength. This continuous distribution is approximated by defining the inlet profile by a finite number



of discrete elements. Each element is represented by a point on the element (the midpoint) called the control point. Also, the source strength is assumed to be constant on each element. This approximation results in a set of linear algebraic equations which are solved by matrix methods for the source strength at the control points. Velocities at the control points and at specified off-body points are then calculated from the source distribution.

The Hess axisymmetric potential flow routine is used to obtain three basic solutions which are used in linear combination to satisfy the prescribed inlet operating conditions. Solutions obtained for the inlet in axial freestream flow with an open-duct inlet, axial freestream flow with a closed-duct inlet, and freestream cross flow with an open-duct inlet.

### 6.1.3 ARBITRARY FLOW CONDITION SOLUTION

The three basic solutions from EOD are then used by the Combination Routine (COMBYN) to compute a solution of interest having arbitrary flow conditions of  $V_\infty$ ,  $\alpha$ , and mass flow ( $\dot{W}$ ). The linear combination equation is:

$$\vec{V} = A\vec{V}_1 + B\vec{V}_2 + C\vec{V}_3 \quad (6.1)$$

where  $V_1, V_2, V_3$  are the three basic solutions and A,B,C are influence coefficients obtained from the three flow conditions:  $V_\infty$ ,  $\alpha$ ,  $\dot{W}$ .

The velocity obtained by equation (6.1) is incompressible. The Lieblein-Sockman compressibility correction (reference 6.4)

$$V_{cor} = V_i \left( \frac{\rho_T}{\rho_S} \right)^{1/2} V_i / \bar{V}_i \quad (6.2)$$

is used to compute the compressible velocity. All the terms on the right hand side of equation (6.2) are obtained from the incompressible solution or the input flow conditions. This equation handles both local sonic and supersonic velocities. The compressible flow properties (Mach number, pressure ratio, streamlines) are obtained from the compressible velocity,  $V_{cor}$ . Typical output and capabilities of the potential flow routine are shown in Figure 6-2.

METHOD: DOUGLAS NEUMANN  
(REFERENCE 6.3)

OUTPUT

$P_S / P_T$   
 $V_{SUR}$  AND  $M_{SUR}$   
SUR = SURFACE

CAPABILITIES

AXISYMMETRIC  
ISENTROPIC  
SUBSONIC FLOW  
COMPRESSIBILITY  
LOCALLY SUPERSONIC  
FLOW FIELDS { INTERNAL  
EXTERNAL

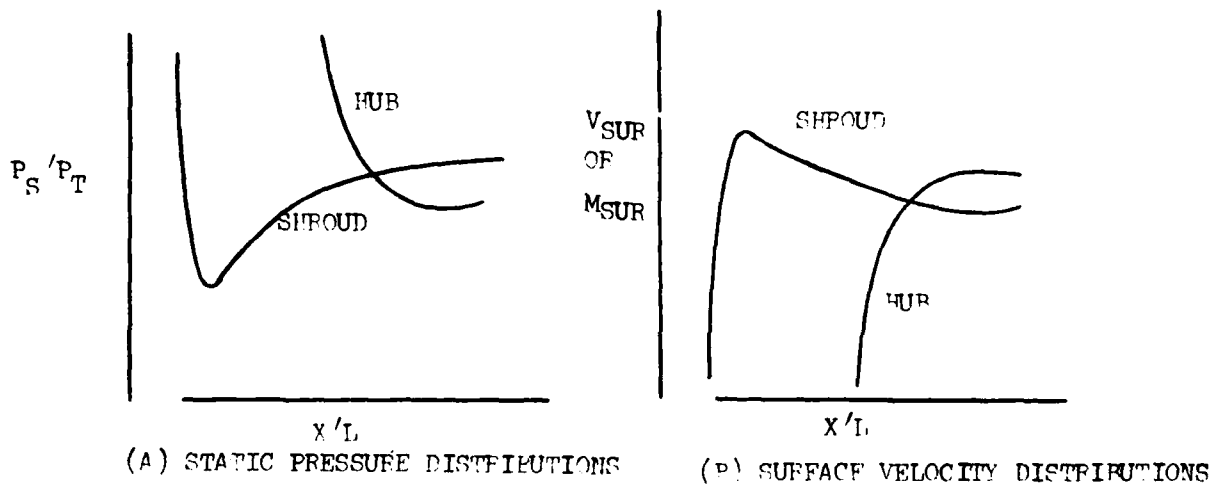


Figure 6-2. Typical Potential Flow Routine Results

#### 6.1.4 BOUNDARY LAYER SOLUTION

The surface Mach number distributions obtained from program COMBYN are used as input to the Albers-Gregg boundary layer calculation (program VISCUS). The boundary layer calculations are based on the assumption that the flow is two-dimensional, either planar or axisymmetric. Program VISCUS, documented in reference 6-3 calculates information such as boundary layer profiles, displacement thickness,  $\delta^*$  and skin friction coefficient,  $C_f$ , at each station, and also predicts transition from laminar to turbulent flow. Separation is predicted when  $C_f$  is zero. Typical output and capabilities of the boundary layer routine is shown in figure 6-3.

OUTPUT	CAPABILITY
M	2-D OR AXISYMMETRIC
S	PREDICTS: SEPARATION
C	LAMINAR TRANSITION
F	BLOWING
H	SUCTION
*	

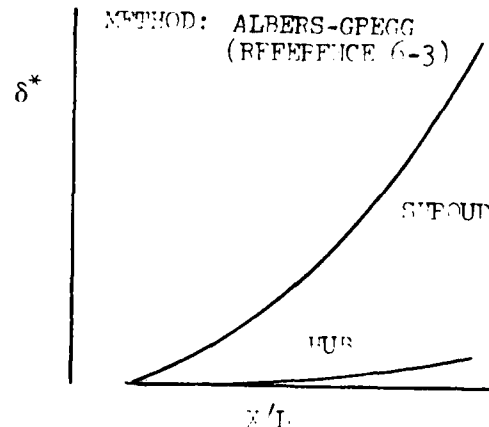


Figure 6-3. TYPICAL BOUNDARY LAYER ROUTINE RESULTS

#### 6.1.5 ITERATIVE LOOP

If the boundary layer is significant in the inlet region of interest, it may be desirable to add the displacement thickness,  $\delta^*$ , to original inlet profile and repeat the entire solution procedure. Thus new Mach number and  $\delta^*$  distributions are obtained. This process may be repeated to achieve satisfactory convergence. Usually one iteration is sufficient.

#### 6.1.6 COMBINED POTENTIAL FLOW AND BOUNDARY LAYER ROUTINE

Originally, the Sockman Inlet Analysis routines (SCIRCL, EOD, and COMBYN) and the boundary layer routine (VISCUS) were executed separately in the iterative loop, Figure 6.4. Output from the geometry routine (SCIRCL) included punched card output to be used as input to EOD. Output from the potential flow routine (EOD) included punched cards in binary form for input to COMBYN. Compressible flow Mach number distributions from the combination routine (COMBYN) were then manually prepared for input to VISCUS. Displacement thickness,  $\delta^*$ , from the boundary layer program VISCUS was then used to modify the inputs to SCIRCL, and the process repeated.

In the combined program, output data from SCIRCL and EOD are stored on scratch files which are then accessible by the succeeding routine. Therefore, only a minimum of input data in card form are required. In addition, in the combined program all routines are combined into one large program with an overlay mode of operation. Also, a coordinate transformation routine was developed to bridge from COMBYN to VISCUS, and a geometry modification routine was required to modify the original inlet profile by the viscous displacement thickness,  $\delta^*$ .

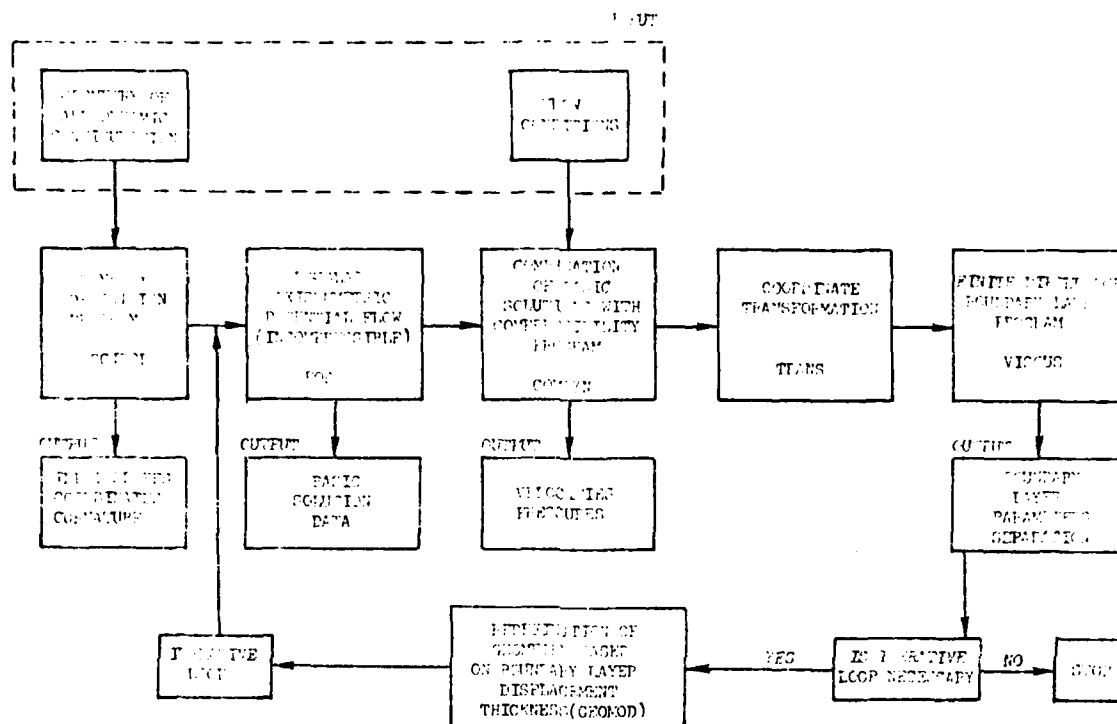


Figure 6-4. Vought Combined Potential Flow and Boundary Layer Program

Combination of the flow solution procedures resulted in cost savings, both in preparation time and in computer run time while maintaining the same accuracy of solution as achieved by the individual codes.

## 6.2 INLET FORCE AND MOMENT PROGRAM

Many proposed advanced aircraft require propulsion system inlets which can operate over a wide range of flight speeds, mass flow, and angles of attack. For example, requirements placed on inlets for Navy V/STOL aircraft can be especially severe due to the operating environment onboard various types of combatant ships. Thus, considerable research and configuration development is required to design inlets for such an application.

Results from analytical studies and from limited test data indicate the forces and moments induced by the inlets can significantly influence the aerodynamic control power requirements for V/STOL aircraft, specifically during transitional flight and at high angles of inlet incidence such as with tilt nacelle configurations. Thus, correct estimation of these forces and moments is important.

The influence of fixed nacelle, lift fan inlets can also influence the control power requirements of the V/STOL aircraft, but generally to a lesser degree due to the reduced inlet angle of incidence. Correct estimation of these forces and moments is also important to the designer.

Inlet forces and moments due to the entering stream tube are a vector sum of the forces and moments created by ram drag and additive drag at a specific engine power setting, angle of inlet incidence, and flight speed.

Test data obtained to determine the magnitude of these forces and moments has been rather limited to date due to the relatively high cost of metric inlet experimentation with flow through simulation. Most available data has been obtained from test installations with the entire nacelle or airframe metric. Because of these deficiencies and limitations in available test data the ability to predict analytically, with accuracy, the force and moments induced by the inlet is a prime requirement for V/STOL research and configuration development.

The Vought force and moment analysis for each inlet operating condition is conducted in two specific steps. First, the combined inlet analysis routine in VAPE is used to calculate pressures on the inlet lip and velocities of the fluid within the inlet duct. Forces and torques imposed on the lip by these pressures; as well as effluxes of momentum and angular momentum in the duct across a plane normal to the axis at the throat, are calculated by the inlet force and moment subroutines in VAPE. Proper accounting of these parameters yields the inlet forces and moments for specific configurations.

The computer code provided with this task was used to generate a series of parametric ram drag charts for subsonic inlets as a function of the point of application, mass flow rate, pitch angle and inlet type and shape. These charts can be used in preliminary aircraft performance synthesis and in simulator programs for flight control studies, to provide rapid estimates of ram drag from the generalized charts without the need for specific computer solutions for each inlet/nacelle configuration evaluated.

## 6.2.1 METHOD OF SOLUTION

The analytical approach to solving for forces and moments induced by the inlet is outlined in the following four step procedure:

- 1 For a particular inlet geometry, the internal and external surface pressure and streamwise velocity distributions at several circumferential ( $\psi$ ) stations around the inlet are determined by VAPE . The user must also define internal and external control boundaries which must include the predicted stagnation points and all of the rake stations.
- 2 The program searches the internal and external surface velocity distribution at each station to define the stagnation points.
- 3 The inlet control volume is defined by the Loci of surface stagnation points and by a user specified rake station where the streamwise velocity distribution is known. Note that this rake station must be within the control volume boundaries defined in (1) above.
- 4 The inlet force and moments are calculated by summing the force and moment integrals (presented below) around the control volume.

The program determines the inlet force and moment components relative to (a) the aircraft body axis coordinate system, (b) the inlet coordinate system, and (3) the inlet coordinate system about the user selected reference point. These coordinate systems are defined in Figure 6.5.

The remainder of this section defines the pertinent equations utilized in the inlet force and moment code and presents parametric charts of ram force and moment arm data.

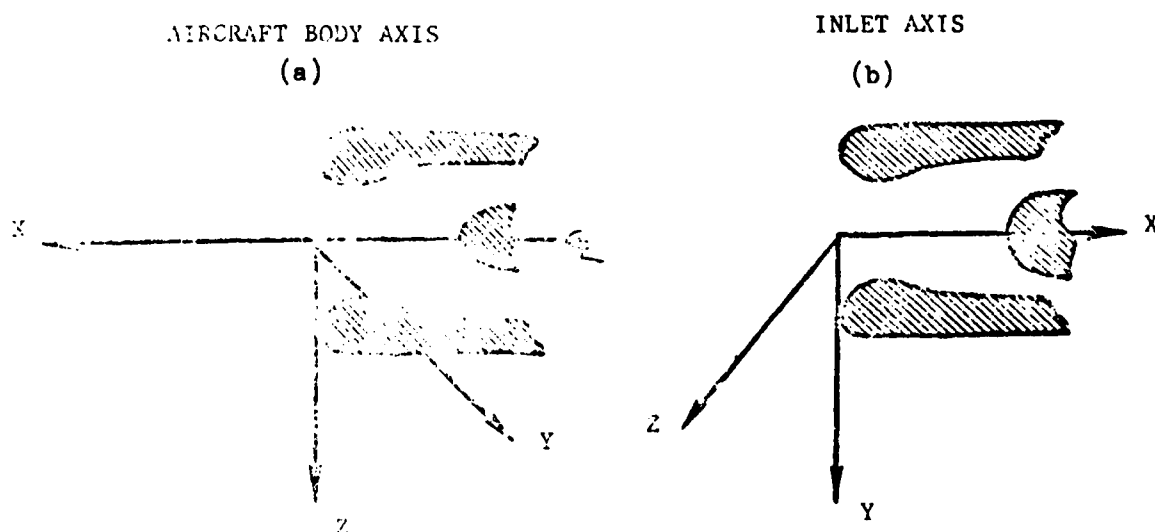


Figure 6.5. Coordinate System for Force and Moment Calculations

## 6.2.2 FORCE EQUATIONS

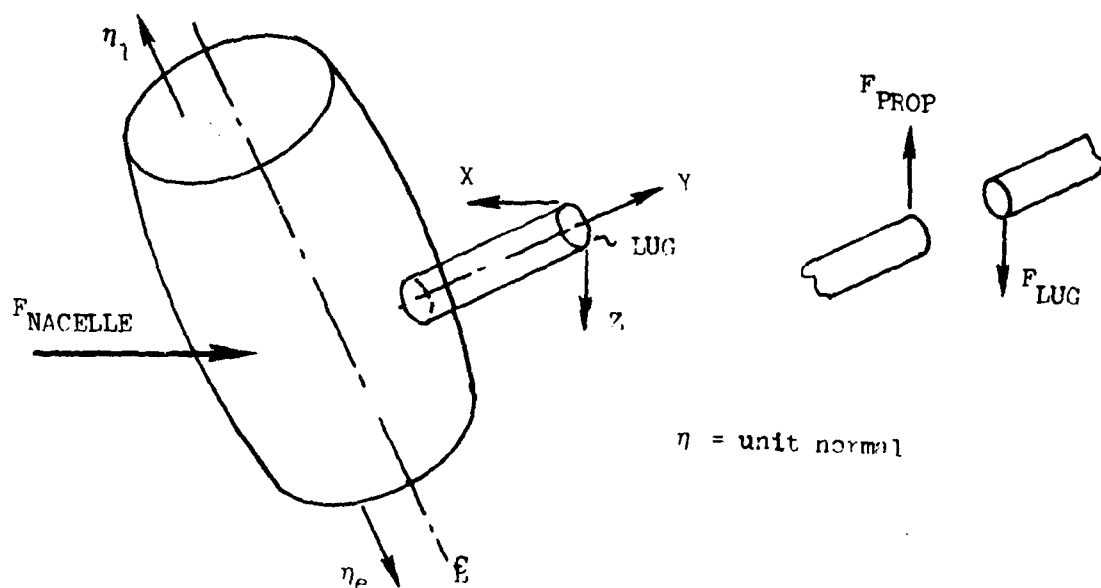


Figure 6.6. Force Schematic for Inlet Force and Moment Algorithm

## CONFIGURATION OF MOMENTUM EQUATIONS

$$\begin{aligned}
 \vec{F}_{lug} + \vec{F}_{nacelle} + \int_{inlet} (P_1 - P_{AMB}) \vec{n}_1 dA_1 + \int_{exit} (P_e - P_{AMB}) \vec{n}_e dA_e \\
 = \int_{inlet} \frac{\rho}{q_0} (\vec{V}_1 \cdot \vec{n}_1) \vec{V}_1 dA + \int_{exit} \frac{\rho}{q_0} (\vec{V}_e \cdot \vec{n}_e) \vec{V}_e dA \\
 \vec{F}_{lug} = \int_{inlet} (P_1 - P_{AMB}) \vec{n}_1 dA_1 + \int_{inlet} \frac{\rho}{q_0} (\vec{V}_1 \cdot \vec{n}_1) \vec{V}_1 dA \\
 + \int_{exit} (P_e - P_{AMB}) \vec{n}_e dA_e + \int_{exit} \frac{\rho}{q_0} (\vec{V}_e \cdot \vec{n}_e) \vec{V}_e dA - \vec{F}_{nacelle}
 \end{aligned}$$

$F_{\text{PROP}}$  = Right hand side of equation (6.4)

$$\vec{F}_{\text{inlet}} = - \int (P_1 - P_{\text{AMB}}) \vec{n}_1 dA_1 - \int \frac{\rho}{q_0} (\vec{V}_1 \cdot \vec{n}_1) \vec{V}_1 dA$$

These inlet force integrals are evaluated using the inlet flow analysis program.

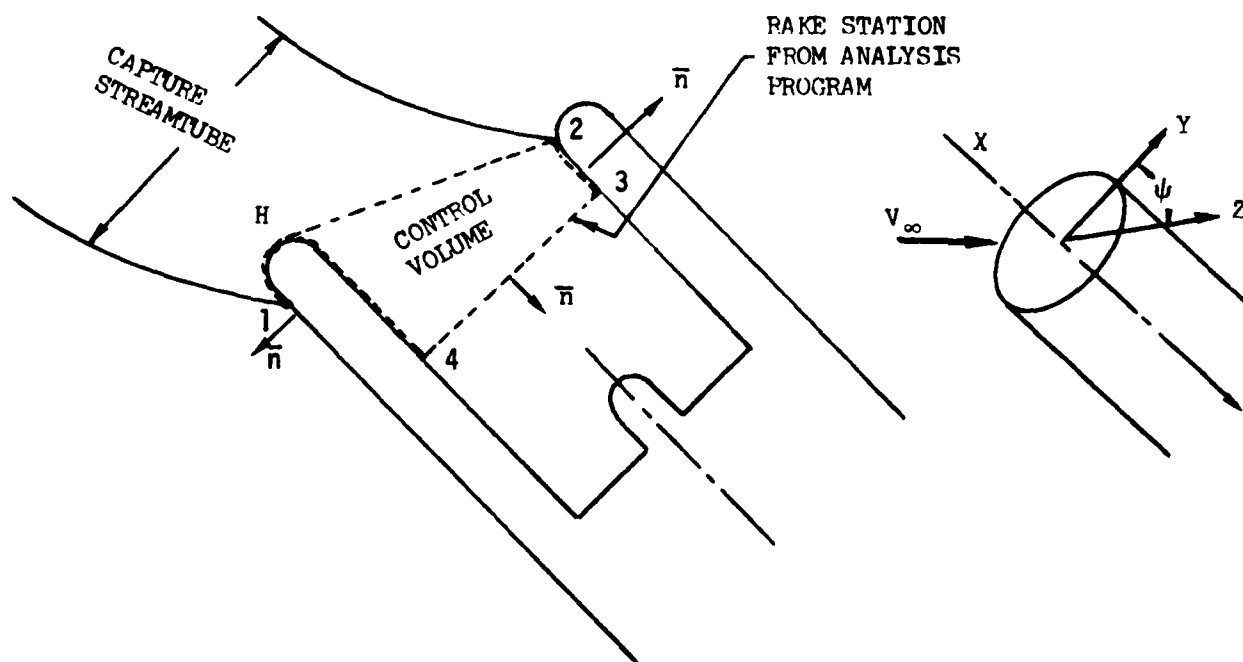


Figure 6.7. Schematic of Momentum Box for Inlet Integration

$$\begin{aligned} \vec{F}_{\text{inlet}} = & \int_{2-3}^{(1)} (P_{23} - P_{\text{AMB}}) \vec{n}_{2-3} dA + \int_{3-4}^{(2)} (P_{3-4} - P_{\text{AMB}}) \vec{n}_{3-4} dA \\ & + \int_{4-H-1}^{(3)} (P_{4H1} - P_{\text{AMB}}) \vec{n}_{4H1} dA + \int_{3-4}^{(4)} \frac{\rho_0}{q_0} (\vec{V}_{3-4} \cdot \vec{n}_{3-4}) \vec{V}_{3-4} dA \end{aligned}$$



- o Integrate integrals (1) and (3) along  $X$  and  $\psi$

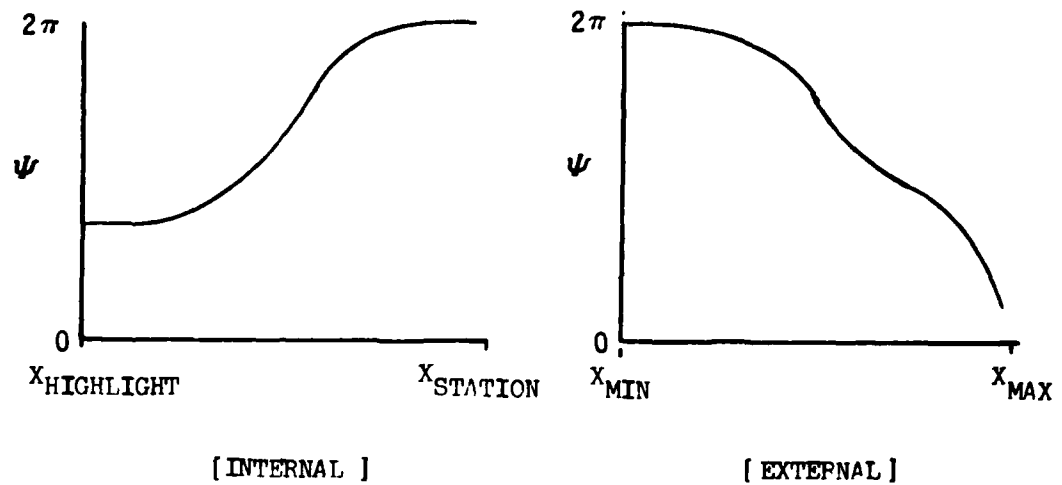


Figure 6.8. Schematic of Integrals (1) and (3) Domains

Internal pressure area integrals have same equations except for sign change.

(INTERIOR)  $\int_{X_{MIN}}^{X_{STATION}} \int_{\psi_{MIN}}^{\psi_{MAX}} (P - P_{AMB}) \left[ \left( \frac{dy}{dx} \right) \vec{i} - \cos \psi \vec{j} - \sin \psi \vec{k} \right] \gamma_S dx d\psi$

Where

with  $P$  = surface pressures at  $x$

$\frac{dy}{dx}$  is derivative of surface at station  $x$

Figure 6.9. Coordinate Axis Definition

- o Integrate integral (2) along  $\psi$  and  $r$

$$\int_0^{2\pi} \int_{r_0}^{r=r_{STATION}} (P_{34} - P_{AMB}) \vec{n}_{3-4} dA \quad \text{with } P = \text{Surface Pressures at } r$$

with  $dA = r d\psi dr = y d\psi dr$

$$\vec{n}_{34} = \vec{i}$$

o Integrate integral (4) along  $X$  and  $\psi$

$$\int_0^{2\pi} \int_{r_0}^{r_{\text{STATION}}} \frac{\rho_0}{q_0} \left[ 1 - (.20) \left\{ \frac{V_X^2 + V_Y^2 + V_Z^2}{a_0^2} \right\} \right]^{\frac{1}{\gamma-1}} (V_X)(i \vec{V}_X + j \vec{V}_Y + k \vec{V}_Z) r dr d\psi$$

With  $V_X, V_Y, V_Z$  = velocities at rake station

After the forces are obtained, they are then resolved into components relative to the airplane body axes.

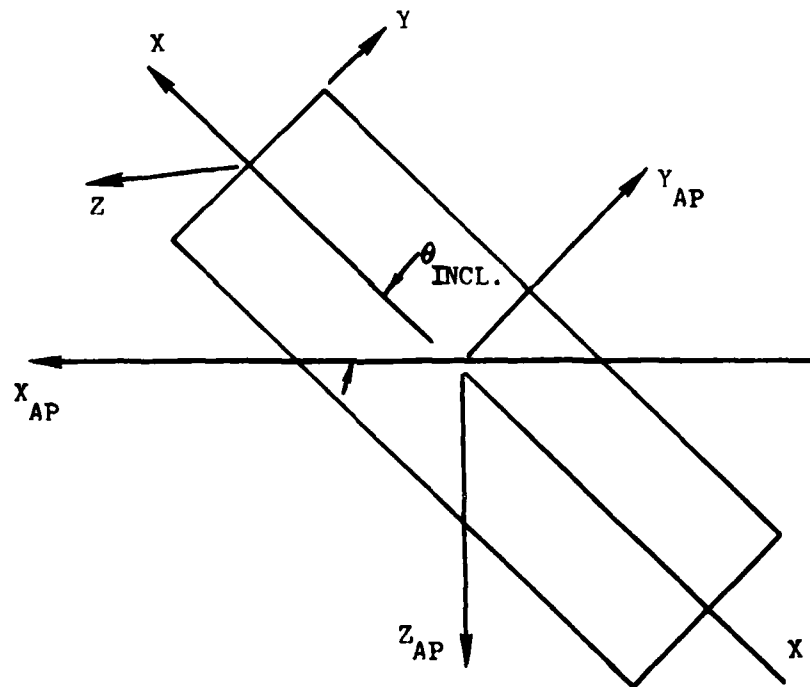


Figure 6.10 Transformation Description

## 6.2.3 MOMENT EQUATIONS

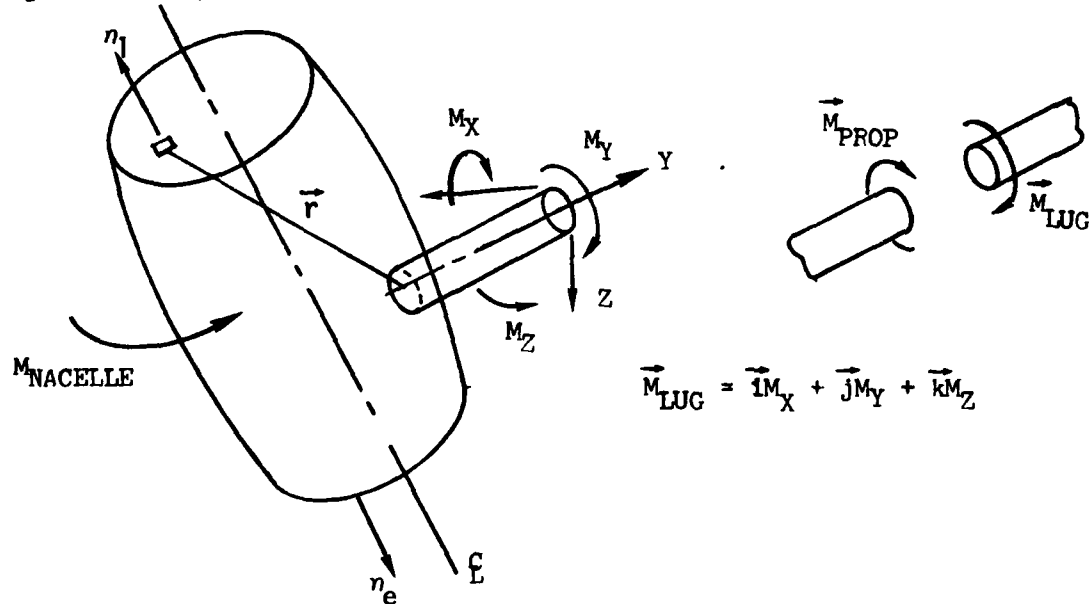


Figure 6.11. Schematic of Moments Generated on Nacelle

## MOMENT OF MOMENTUM EQUATIONS

$$\begin{aligned}
 -\vec{M}_{lug} + \vec{M}_{nacelle} + \int_{inlet} -(P_1 - P_{AMB}) \vec{n}_1 dA_1 \vec{r} + \int_{exit} -(P_e - P_{AMB}) \vec{n}_e dA_e \vec{r} \\
 = \int_{inlet} \frac{\rho}{q_0} (\vec{V}_1 \cdot \vec{n}_1) \vec{V}_1 dA \vec{r} + \int_{exit} \frac{\rho}{q_0} (\vec{V}_e \cdot \vec{n}_e) \vec{V}_e dA \vec{r}
 \end{aligned}$$

$$\begin{aligned}
 -\vec{M}_{lug} = \vec{M}_{prop} = \int_{inlet} (P_1 - P_{AMB}) \vec{n}_1 dA_1 \vec{r} + \int_{inlet} \frac{\rho}{q_0} (\vec{V}_1 \cdot \vec{n}_1) \vec{V}_1 dA \vec{r} + \\
 \int_{exit} (P_e - P_{AMB}) \vec{n}_e dA_e \vec{r} + \int_{exit} \frac{\rho}{q_0} (\vec{V}_e \cdot \vec{n}_e) \vec{V}_e dA \vec{r} \\
 - \vec{M}_{nacelle}
 \end{aligned}$$

then let

$$M_{\text{inlet}} = \int_{\text{inlet}} (P - P_{\text{AMB}}) \vec{n}_1 dA \vec{r} + \int_{\text{inlet}} \frac{\rho}{q_0} (\vec{V}_1 \cdot \vec{n}_1) \vec{V}_1 dA \vec{r}$$

These inlet integrals are evaluated using the inlet flow analysis program.

$$\begin{aligned} M_{\text{inlet}} = & \int_{2-3,4H-1} (P - P_{\text{AMB}}) \vec{n} dA \vec{r} + \int_{3-4} (P - P_{\text{AMB}}) \vec{n} dA \vec{r} \\ & + \int_{3-4} \frac{\rho_0}{q_0} (\vec{V}_{34} \cdot \vec{n}_{34}) \vec{V}_{34} dA \vec{r} \end{aligned}$$

These inlet moment or momentum integrals are then evaluated in a similar manner to the momentum equations previously described.

After the moments are obtained they are then resolved into components relative to the airplane body axes.

The moment arm of the resolved components is obtained by dividing the Moment of Momentum by the Momentum Force 11:

#### 6.2.4 PROGRAM CODE CAPABILITY

The program is capable of dealing with the following geometric and free stream flow conditions.

- a. Axisymmetric inlet geometry with arbitrary cowl lip shape.
- b. Arbitrary tilt angle of the inlet centerline relative to the aircraft X (longitudinal axis) -Y (lateral axis) plane.
- c. Arbitrary angle of attack and side slip angle of the aircraft relative wind. (The effects of the aircraft surfaces on the flow approaching the inlet are ignored, however.)
- d. Arbitrary moment reference point specification within the plane of the inlet centerline and the aircraft lateral axis.
- e. Arbitrary subsonic free stream velocity magnitude and inlet mass flow rate.

Input data requirements include the following items:

- a. Geometry of the external and internal inlet cowl in the vicinity of the cowl lip.
- b. Specification of the relative wind magnitude, angle of attack, and angle of sideslip.
- c. Moment reference point specification.
- d. Pressures on the inlet lip surfaces.
- e. Velocities of the flow across some station of the inlet duct.

Items (d) and (e) can be obtained from the VAPE computer program or from measurements taken during a wind tunnel test.

Output data are as follows:

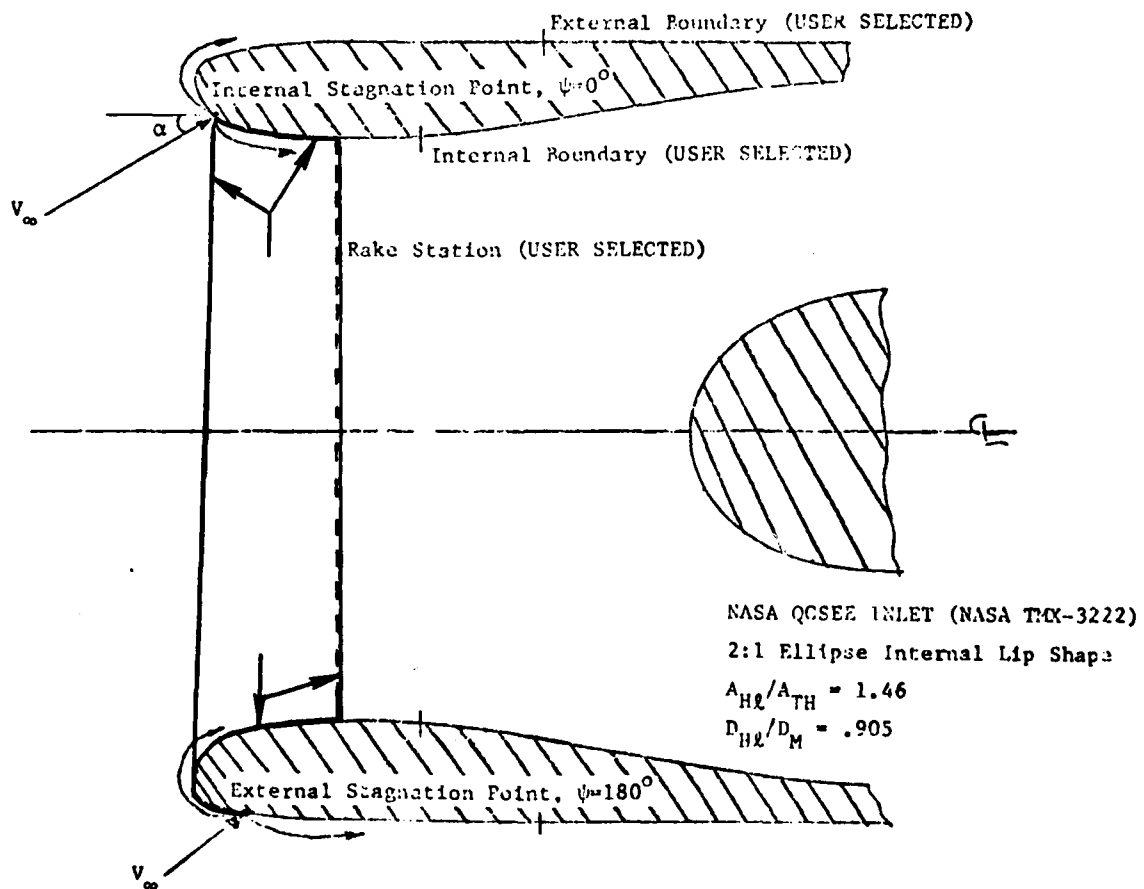
- a. Inlet forces and moments about the user selected reference point and with components parallel to the aircraft body axes coordinate system.
- b. Inlet forces and moments about the user selected reference point and with components parallel to an inlet centerline relative wind vector coordinate system.
- c. Forces and moments imposed on the internal and external surfaces on the inlet cowl lip.
- d. Stream thrust and angular momentum of the flow within the inlet as it crosses the station where flow velocities were defined as a part of the input data. (See item (e) of the preceding paragraph.)

### 6.2.5 RAM FORCE AND MOMENT ARM CHARTS

Charts of ram force and moment arm based on VAPE calculations are presented in this section. These charts give streamwise force,  $F_x$ , Lift Force,  $F_y$ , and ram moment arm,  $z$ , as functions of incidence angle, forward speed, and inlet geometry. These data, while calculated for a tilt nacelle configuration are also applicable to fixed nacelle inlets. All inlet force and moment data presented are based on an aircraft body axis system (Figure 6-5).

The NASA QCSEE inlet, shown in Figure 6.12, was used as the analytical model for this study. This inlet is designed for the low speed characteristics of subsonic V/STOL applications. NASA has conducted experimental investigations and documented the performance of this inlet design. The inlet features an area contraction ratio of 1.46, a diameter ratio of 0.905 and a 2:1 ellipse internal lip shape.

The force and moment data were generated by calculating surface and streamwise flow data at 19 circumferential positions around the inlet ( $0 \leq \psi \leq 180$ ). The control volume boundaries for the ram force and moment arm analysis are also defined in Figure 6.12.



6.12. NASA QCSEE GE2 Inlet Geometry

The lift, ram drag, and ram moment arm are presented in Figures (6.13) - (6.15) at a forward speed of 75 kts as functions of mass flow rate and incidence angle. The parameter  $V_{TH}$  in the abscissa of Figures 6.13 - 6.15 is defined as the velocity for uniform flow at the throat station. The lift and ram drag are presented in absolute terms here but are given in non-dimensional form in Appendix B.

Figure 6.13 shows that lift increases with increases in both flow rate (smaller  $V_{\infty}/V_{TH}$ ) and angle of attack. The lift is very sensitive to increases in angle of attack up to  $45^{\circ}$ . However, at the higher angles ( $70^{\circ}$  to  $90^{\circ}$ ) essentially no effect of angle of attack on lift is evident.

Figure 6.14 shows that inlet drag decreases with angle of attack, and generally increases with inlet flow rate. However, at the highest flow rates, especially above  $70^{\circ}$  angle of attack, there is a gradual reduction in drag with inlet flow rate. A reduction in drag as incidence angle increases is reasonable because the effective ram area becomes smaller at higher angles of attack. The effect of incidence angle and mass flow rate on ram moment arm is shown in Figure 6.15. The moment arm increases with both angle of attack and inlet flow rate, but the angle of attack has the more pronounced effect.

The effect of forward speed on the absolute levels of lift, drag and the ram moment arm is presented in Figure 6.16. Reducing forward speed decreases lift and drag, but increases ram moment arm. Additionally, the ram moment arm change with respect to forward speed is shown to be sensitive to inlet angle of attack. This effect could be significant in the design of fixed nacelle V/STOL aircraft controls for the approach and hover flight regimes.

A brief study was made to examine the effect of inlet cowl lip shape on forces and moments. Axisymmetric inlet geometries studied are shown in Figure 6.17. They consist of the NASA QCSEE GE 2 Test Inlet and a thin lip inlet suitable for a supersonic V/STOL.

Forces imposed on the inlet by the captured tube of air that enters the inlets are shown as a function of inlet velocity ratio in Figure 6.18. The force convention is the same as that used for a body-fixed coordinate system in an airplane. The forces are equal to the vector sum of the ram drag and additive drag terms encountered for conventional flight propulsion calculations. For an angle of attack of  $20^{\circ}$ , the streamwise components of the forces are essentially the same for the two inlets. The lift component forces differ by about 6% with the QCSEE inlet having more lift. Forces imposed on the inlets for an angle of attack of  $90^{\circ}$  are essentially the same. The lift and drag forces are given in absolute units in figure 6.18, but are presented in non-dimensional form in Appendix B.

The effect of inlet lip shape on inlet ram moment arm is presented in Figure 6-19. These data show that at low angles of attack, the QCSEE, inlet has a larger moment arm than the thin lip as a result of a thicker lip shape. As the inlet incidence angle is increased to  $90^{\circ}$ , the moment arm for each inlet is essentially the same.

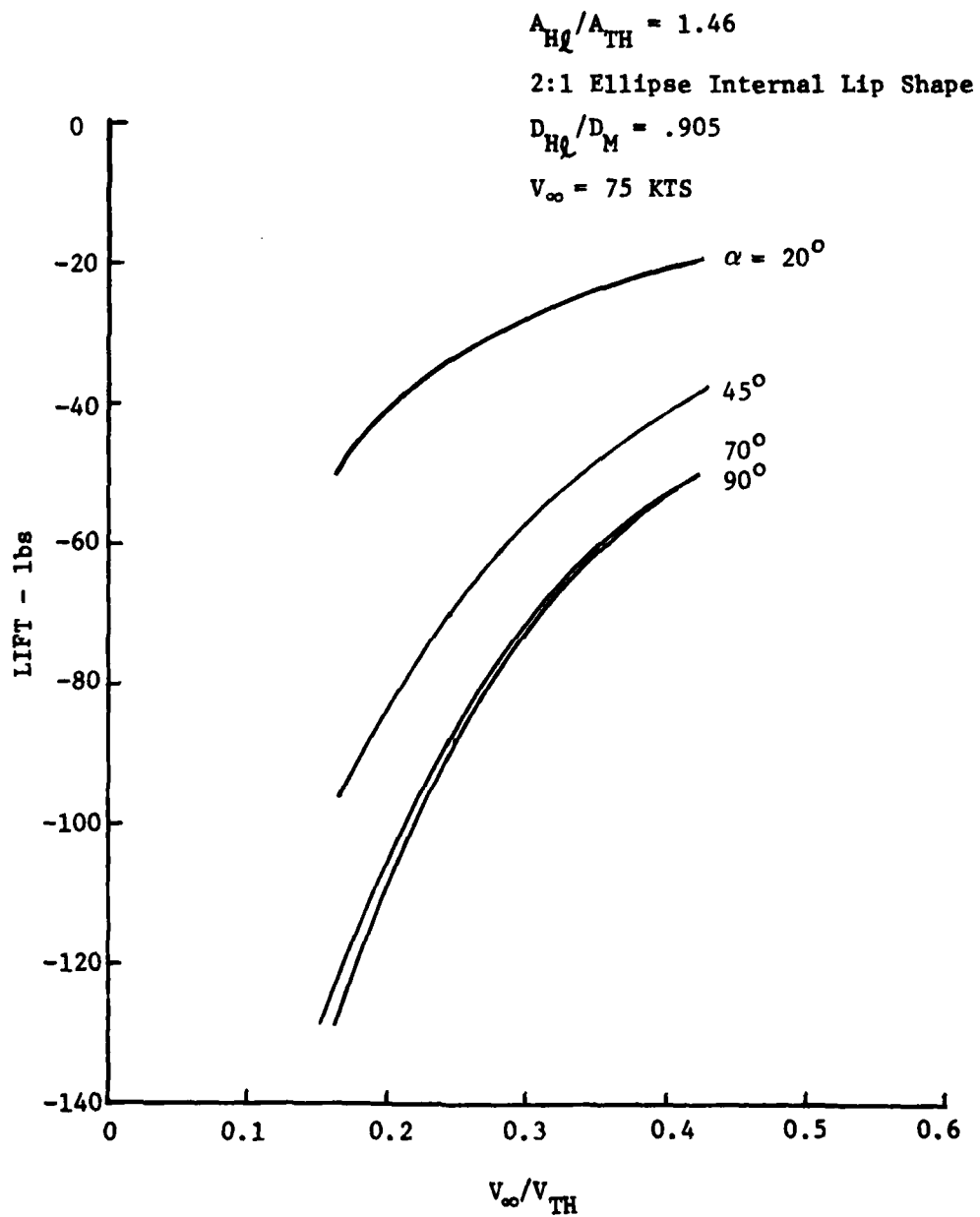


Figure 6-13. Effect of Velocity Ratio on Inlet Lift Force.



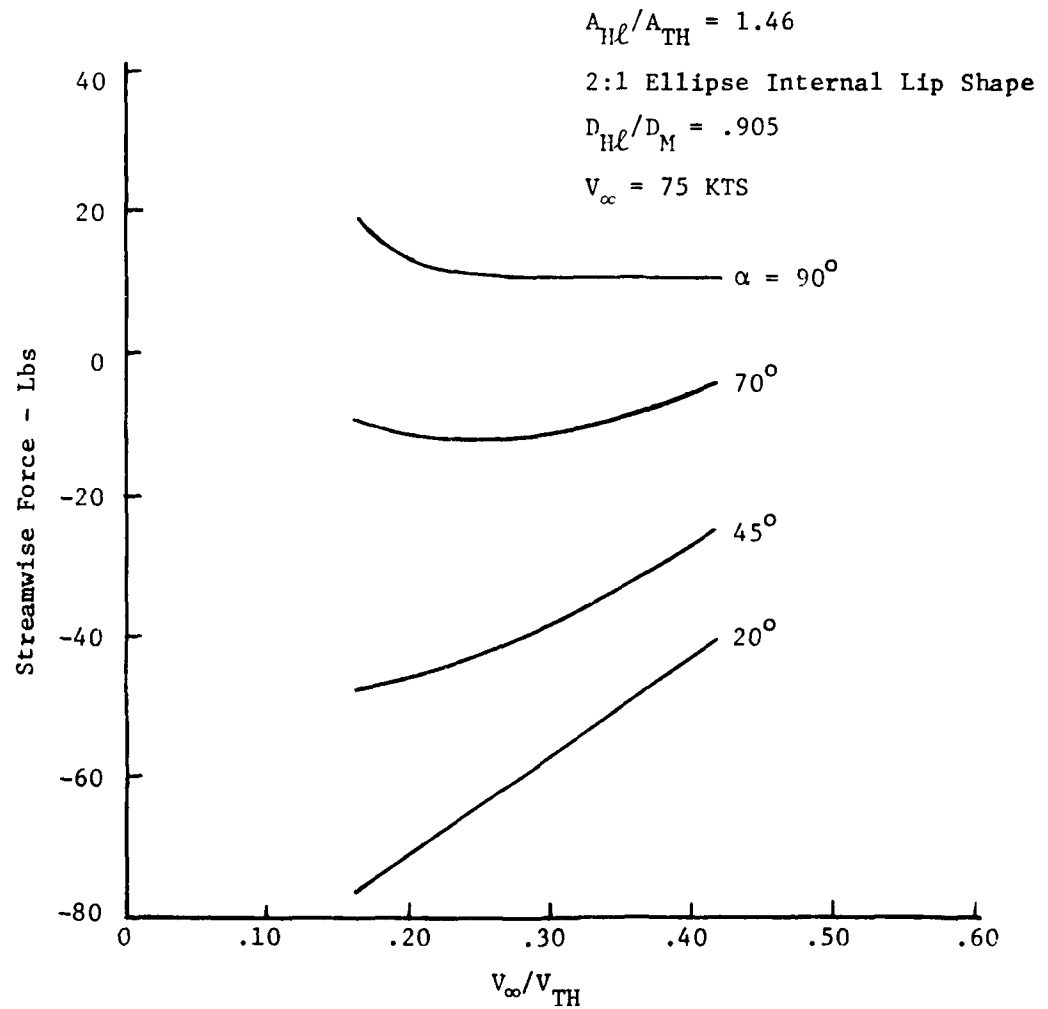


Figure 6-14. Effect of Velocity Ratio on Inlet Streamwise Force

AD-A103 272

VOUGHT CORP DALLAS TX  
PREDICTION METHODOLOGY FOR PROPULSIVE INDUCED FORCE AND MOMENTS--ETC(U)  
JUL 79 T D BEATTY, S S KRESS

F/6 1/3

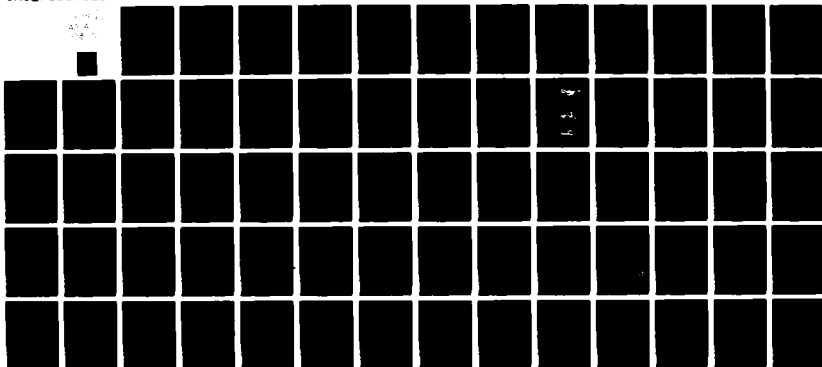
N62269-78-C-0036

NL

NADC-77119-30

UNCLASSIFIED

AD-A103 272



END

DATE

FORMED

9 81

DTIC

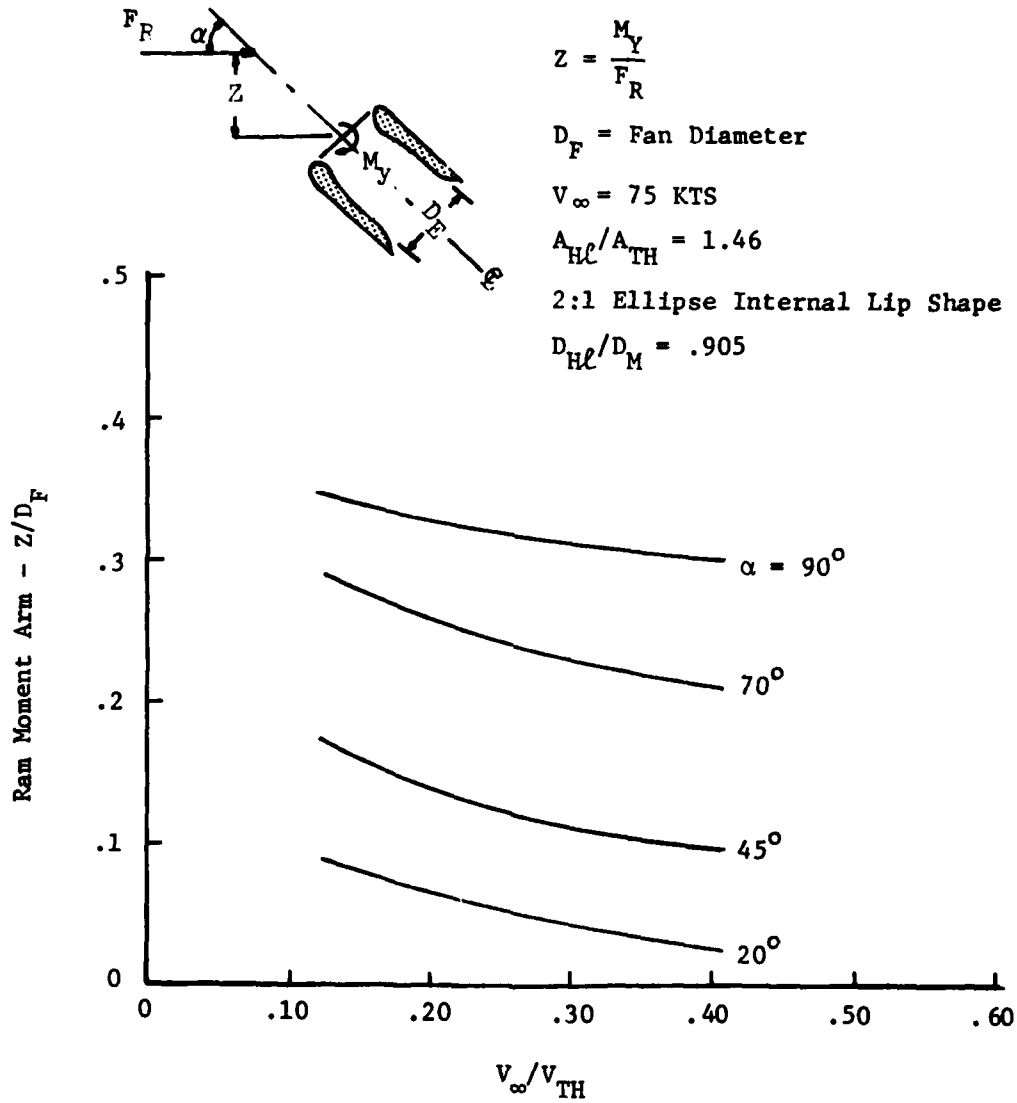


Figure 6-15. Effect of Velocity Ratio on Inlet Ram Moment Arm

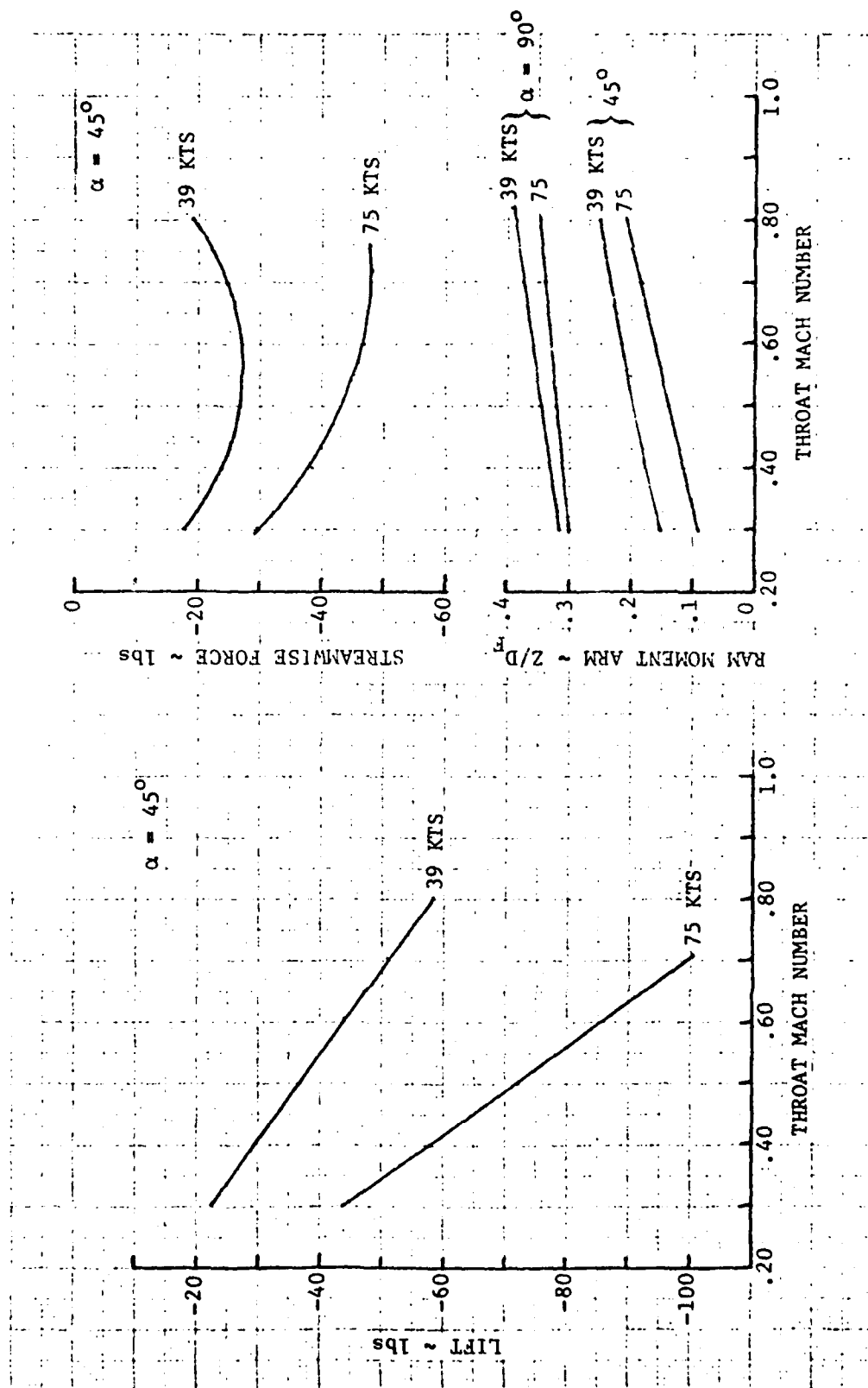


Figure 6-16. Effect of Freestream Velocity on Inlet Forces and Moments

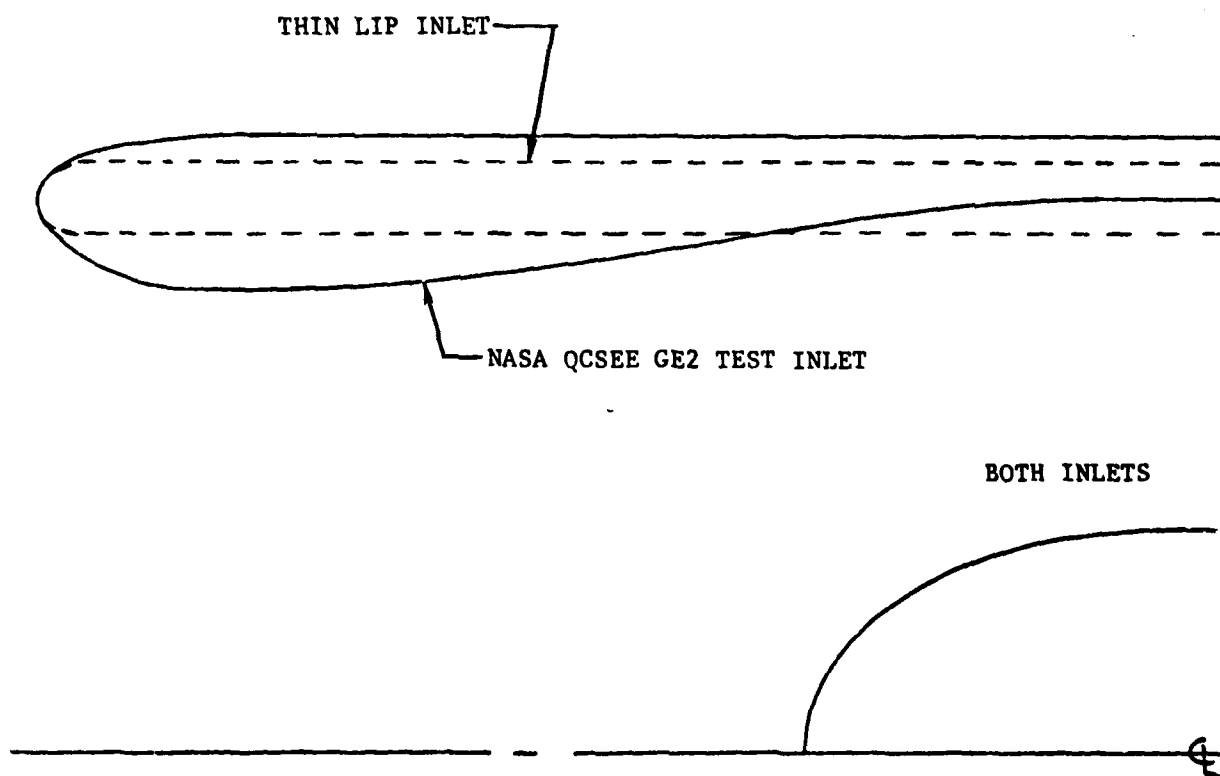


Figure 6-17. Comparison of Thin Lip Inlet to QCSEE Configuration

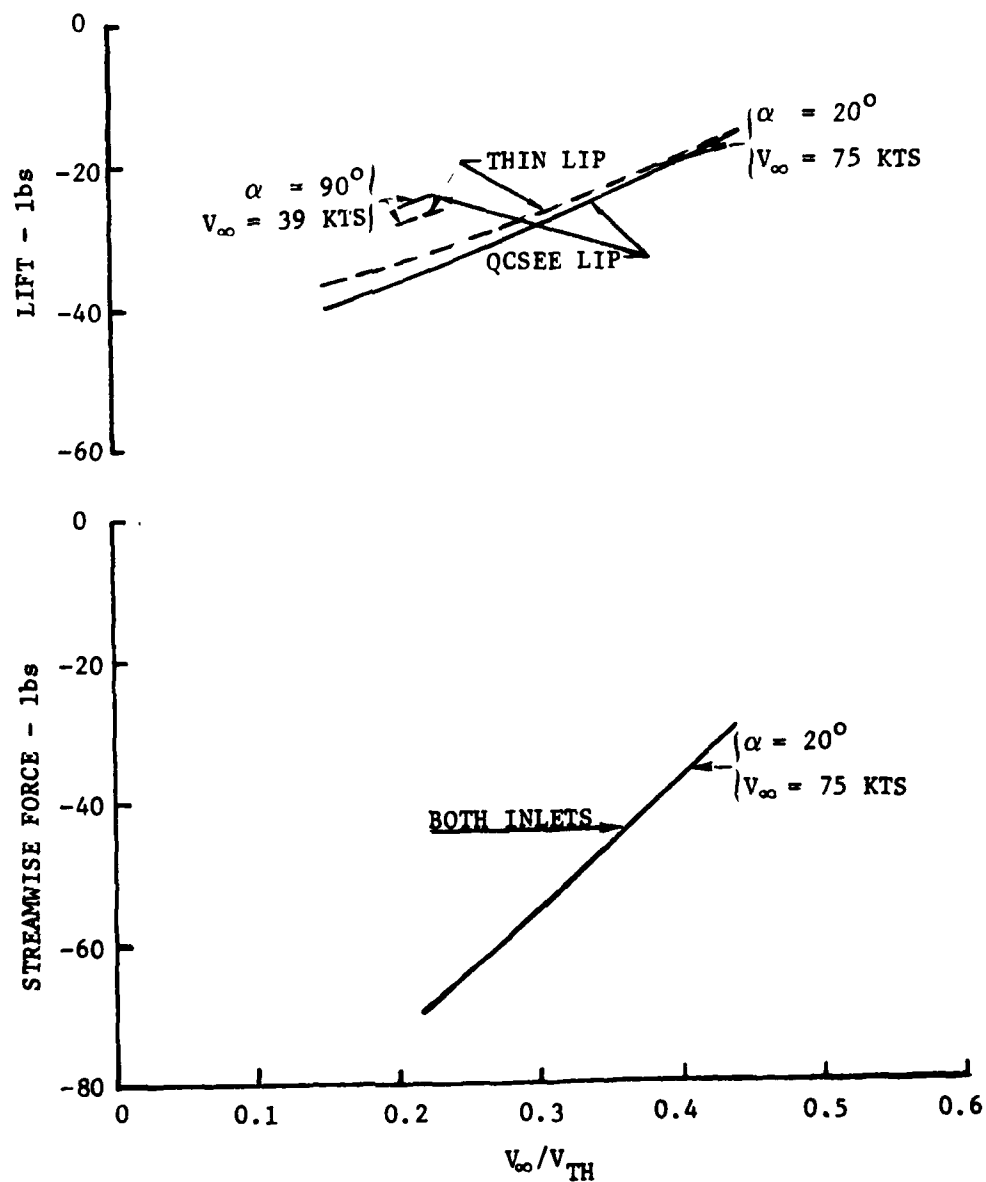


Figure 6-18. Effect of Lip Shape on Inlet Force Components.

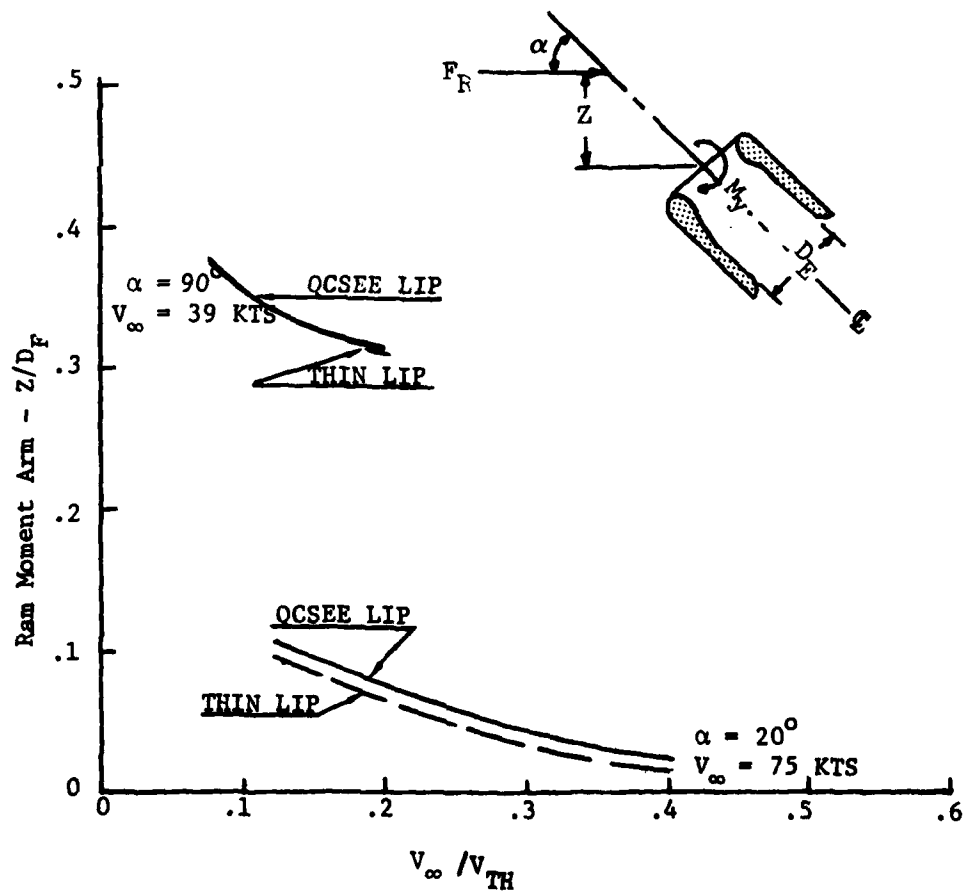


Figure 6-19. Effect of Lip Shape on Inlet Ram Moment Arm

### 6.3 INLET SEPARATION ANALYSIS

A study was performed to develop inlet separation boundaries for V/STOL aircraft using the inlet analysis techniques discussed in Sections 6.0 and 6.1. This section presents the details of the approach used and the results obtained.

#### 6.3.1 INLET DESIGN VARIABLES

The major variables defining inlet design are shown in Figure 6.20. For this study, three design variables were investigated: (1) area contraction ratio,  $D_{H1}/D_{TH}$ ; (2) diameter ratio,  $D_{H1}/D_M$ ; and (3) internal lip shape. All of the configurations considered are based on the QCSEE, entry lip 2 inlet described in reference 6.6. Figure 6.21 presents the variations in entry lip design used to obtain the parametric inlet separation data. No effect of diffuser wall slope or length was considered in this study. In all cases, the inlet throat and diffuser exit diameters and the diffuser length were held constant. The reader is referred to reference 6.7 for a description of the effects to be expected from these diffuser parameters.

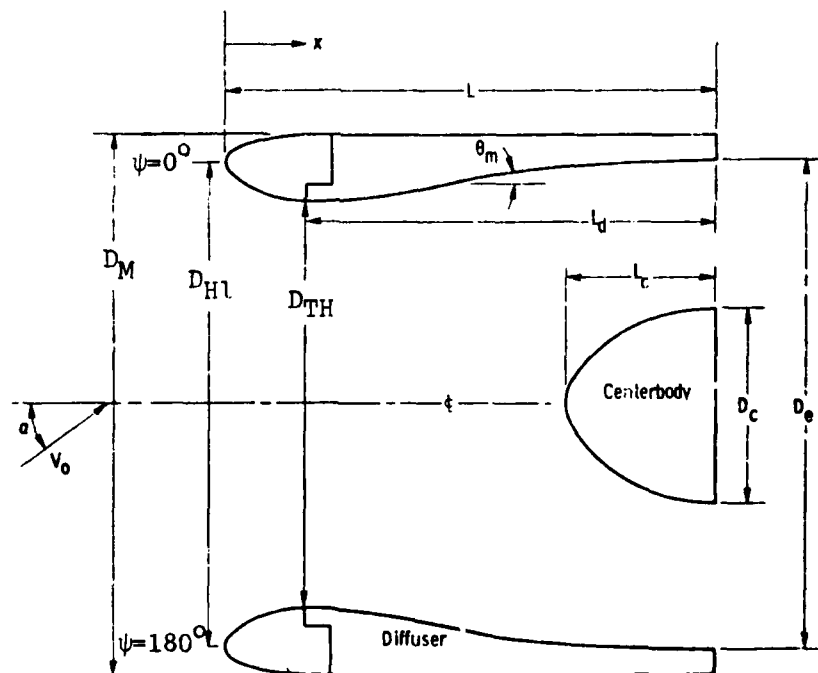


Figure 6.20. Inlet Nomenclature



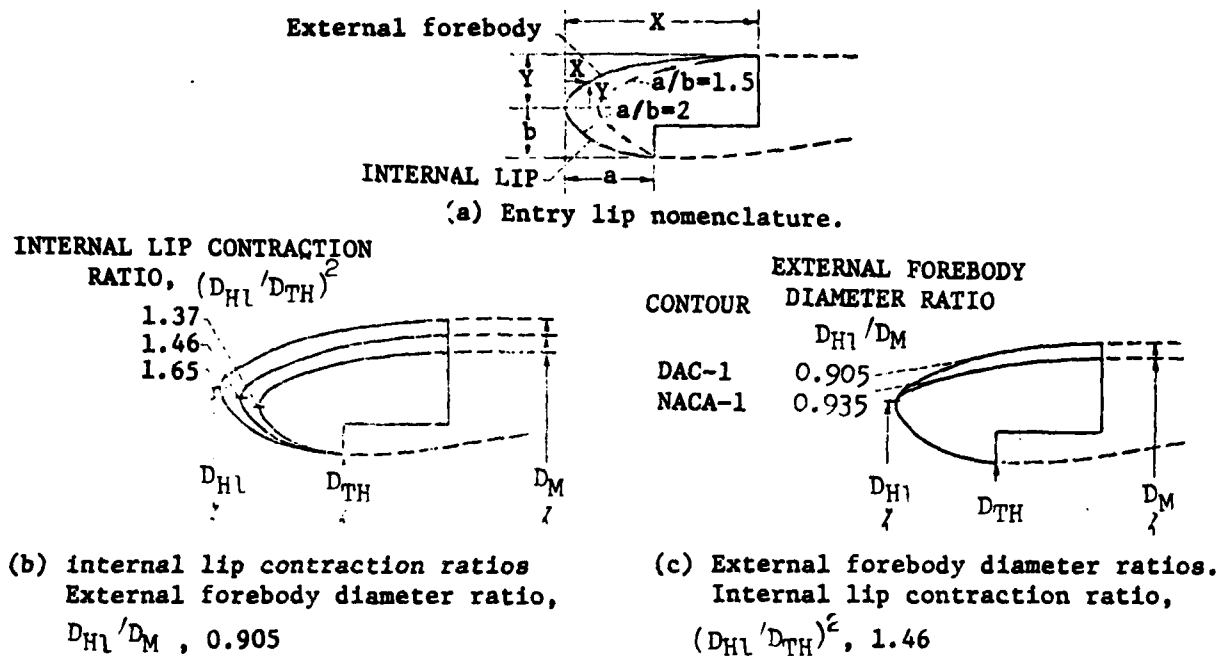


Figure 6.21. Entry-lip Nomenclature and Range of Geometric Variables Tested

Table 6.1 presents a complete summary of all inlet geometric variables considered.

### 6.3.2 ANALYSIS METHOD

Prediction of inlet lip separation boundaries for each of the configurations summarized in Table 6.1 was accomplished by running the inlet analysis routine discussed in Section 6.1.

Two types of inlet separation are predicted by the viscous routine: diffuser separation and lip separation. Diffuser separation is defined as the point on the shroud or hub surface where the boundary layer skin friction coefficient,  $C_f$ , is zero or where the derivative  $dC_f/ds$  changes sign (in an adverse pressure gradient). The latter anomaly occurs in several finite difference type boundary layer programs. At this point the program will define a separation velocity profile and print out various boundary layer parameters at each station preceeding the predicted separation point. The lip separation is determined by analyzing the configuration at various angles of attack (always increasing in value) until an angle is reached where laminar separation without the possibility of turbulent reattachments is obtained.

TABLE 6.1. SUMMARY OF INLET GEOMETRIC VARIABLES

## (a) Entry Lip

GEOMETRIC VARIABLE	ENTRY-LIP NUMBER				
	1	2	3	4	5
Internal lip contraction ratio, $(D_{Hl}/D_t)^2$	1.37	1.46	1.56	1.46	1.46
External forebody diameter ratio, $D_{Hl}/D_M$	0.905	0.905	0.905	0.935	0.905
Ratio of external forebody length to maximum diameter, $\chi/D_M$	0.2	0.2	0.2	0.175	0.161
External forebody contour <sup>a</sup>	DAC-1	DAC-1	DAC-1	NACA-1	*
External forebody proportions, $\chi/Y$	4.21	4.21	4.21	5.38	3.38
Internal lip contour	Ellipse	Ellipse	Ellipse	Ellipse	Ellipse
Internal lip proportions, $a/b$	2.0	2.0	2.0	2.0	1.5
Ratio of overall inlet length of diffuser exit diameter, $L/D_e$	0.97	1.00	1.06	1.00	0.96

## (b) Diffuser

Ratio of exit flow area to inlet flow area, $(D_e^2 - D_c^2)/D_t^2$	1.21
Ratio of diffuser length to exit diameter, $L_d/D_e$	0.826
Ratio of centerbody diameter to diffuser exit diameter, $D_c/D_e$	0.400
Maximum local wall angle, $\theta_m$ , deg	8.7
Location of maximum local wall angle, percent $L_d$	50
Equivalent conical half angle, deg	2.9
Surface contour	Cubic

## (c) Centerbody

Ratio of length to diameter, $L_c/D_c$	0.75
Surface contour	Ellipse
Ratio of centerbody length to diffuser length, $L_c/L_d$	0.357

<sup>a</sup>The DAC-1 contour was developed by the Douglas Aircraft Company and is given by:

$$\left(\frac{Y}{Y}\right)^2 = 2.318 \left(\frac{X}{X}\right) - 2.748 \left(\frac{X}{X}\right)^2 + 2.944 \left(\frac{X}{X}\right)^3 - 1.113 \left(\frac{X}{X}\right)^4$$

\*Faired into same  $x$  for entry-lip number 2 by SCIRCL.

The combined routine, described in Section 6.1.6, uses a different approach for each type of separation as discussed below.

**DIFFUSER SEPARATION:** Diffuser separation occurs where the boundary layer skin friction coefficient goes to zero. The program, if desired, will create a "VISCOUS" body by adding the boundary layer displacement thickness,  $\delta^*$ , to the original geometry at each station up to the point of separation. For each station aft of the predicted separation point, a constant  $\delta^*$  equal to the last calculated value will be used to modify the geometry.

**LIP SEPARATION:** The lip laminar boundary layer separation is defined to occur when laminar separation occurs and the viscous turbulent boundary layer routine cannot negotiate the lip adverse velocity distribution aft of the laminar separation point. The program terminates in the VISCOUS routine with an error code generated.

### 6.3.3 COMPARISON TO NASA EXPERIMENTAL DATA

The predicted inlet lip separation boundaries are compared to NASA test data from references 6.6 and 6.8 in Figure 6.22 for area contraction ratios of 1.37, 1.46, and 1.65. Each inlet has a forebody diameter ratio of 0.905 and a 2:1 ellipse internal lip shape (2:1 defines the ratio of a/b). All of the data presented in Figure 6.22 is for a forward speed of 80 KTS. The boundary layer data was calculated along the  $\psi = 180^\circ$  meridian angle (see Figure 6.1). All of the predicted lip separation boundaries were calculated at inlet throat Mach numbers of 0.371, 0.600, 0.700 and 0.800. Generally, for a given  $M_{TH}$  inlet incidence angle was increased until lip separation occurred.

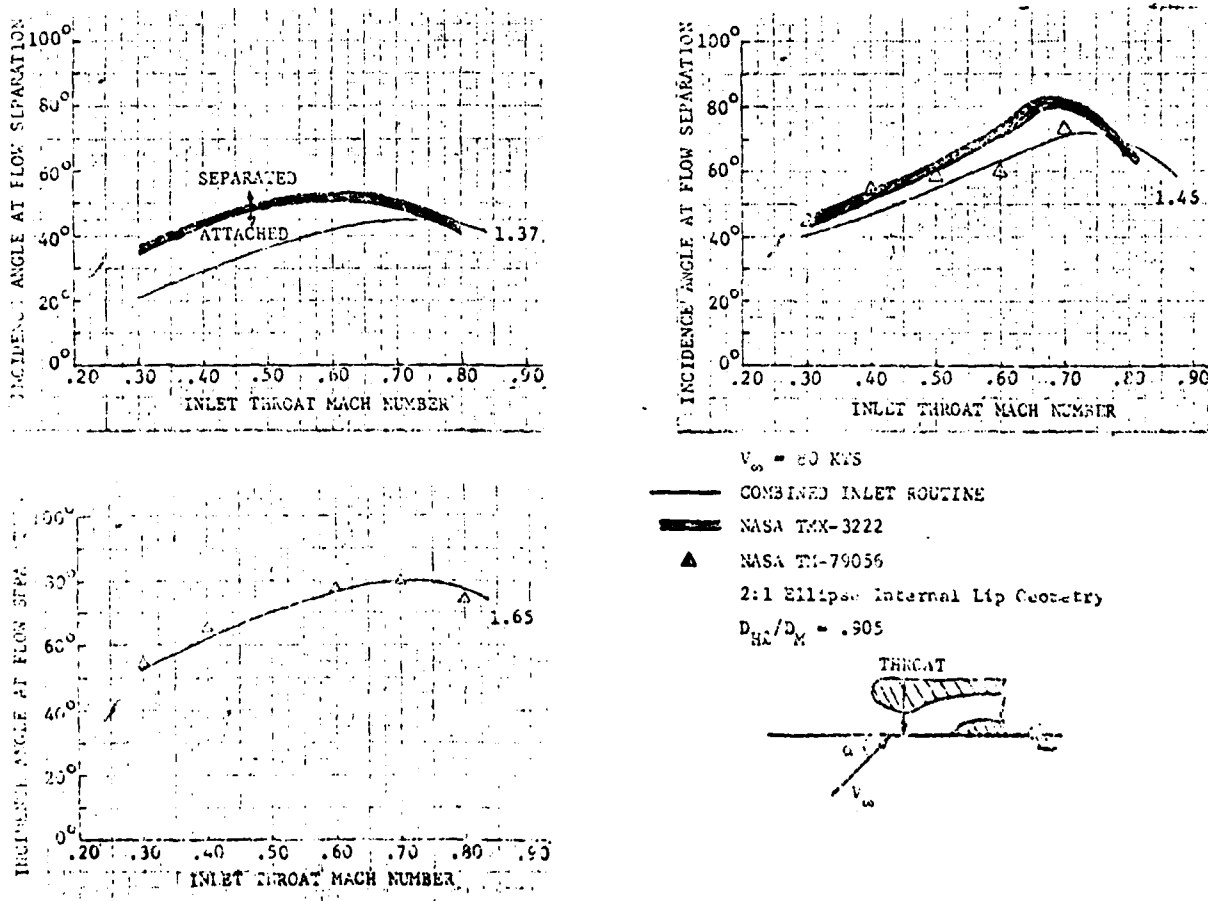


Figure 6.22 Comparison of Calculated Results with NASA Experimental Data

The data presented in Figure 6.22 show better agreement between the predicted separation boundary and the experimental data for the larger inlet area contraction ratios. The correlation presented for a contraction ratio of 1.65 shows excellent agreement at all throat mach numbers. At the lower contraction ratios, the calculated maximum lip separation angle is seen to occur at a higher flow rate than found experimentally. This shift is due to two causes. First, for low contraction ratios, the lower separation boundaries indicated by the predicted data may be due to the boundary layer analysis routine. The predicted results are based on an axisymmetric boundary layer method whereas the experimental data is asymmetric. This would imply that the severity of the pressure gradient is less in the experimental data than in the calculated results, which would result in early prediction of separation. Secondly, the experimental lip separation boundaries decrease more rapidly at the high throat mach numbers. Reference 6.9 suggests that this trend is caused by shock-boundary layer interaction on the cowl surface. The predicted data do not account for these effects; therefore, the separation boundaries will be more optimistic in this region.

In all of the predicted inlet separation data presented in this report, the incidence angle at lip separation was used to define the boundaries. This method should therefore produce slightly conservative results.

#### 6.3.4 INLET SEPARATION CHARTS

Representative flight conditions for V/STOL aircraft are presented in Figure 6.23. Generalized inlet lip separation charts have been developed for these flight conditions for screening of preliminary inlet designs, and are presented in Appendix A. Lip separation data are presented for three of these flight conditions in this section. The charts present inlet incidence angle for lip separation as a function of mass flow rate, inlet geometry, and forward speed. All of the curves represent separation boundaries for the inlet lower lip ( $\psi = 180^\circ$  Figure 6.1). Although the flight conditions presented in Figure 6.23 are for a tilt nacelle configuration, these charts are applicable to fixed nacelle V/STOL aircraft. It has been shown in V/STOL Type A studies that supercirculation effects from high lift devices can cause a high induced angle of attack at the inlet even though the aircraft angle of attack is low. These effects should be included when screening fixed nacelle designs.

Inlet separation boundaries for area contraction ratios of 1.37, 1.46, and 1.65 are presented as a function of inlet throat Mach number and forward speed in Figure 6.24 through 6.26. These data indicate that at low forward speed, the lip thickness has a significant effect on inlet performance. However, as the forward speed is increased, the lip thickness has a lesser impact (see Figures 6.25 and 6.26). Figures 6.24 and 6.25 indicate that an area contraction ratio of 1.65 is more than sufficient for low speed performance during transition and hover for a typical V/STOL operating envelope.

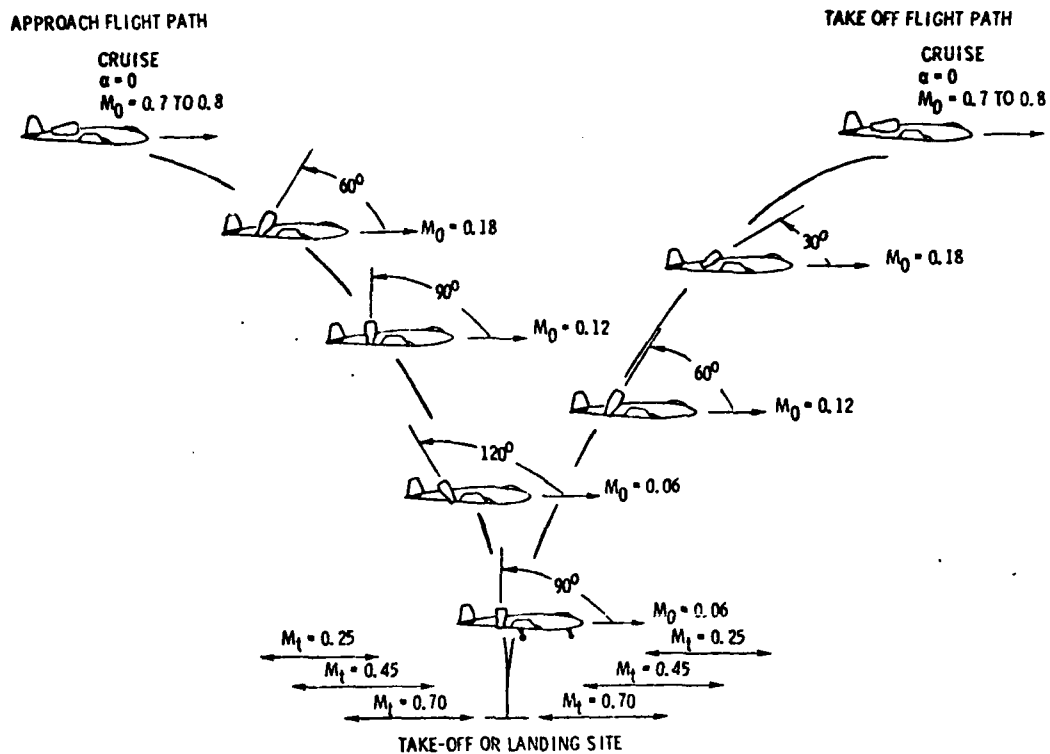
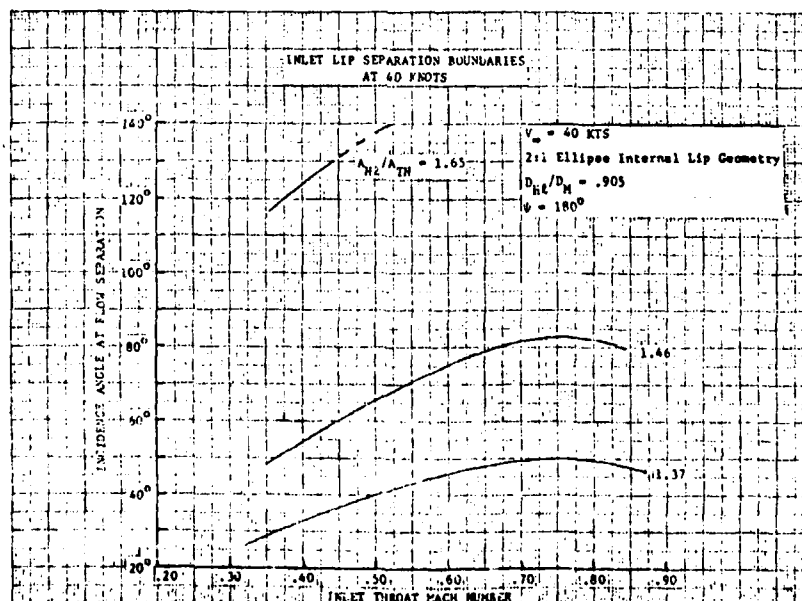


Figure 6.23. Representative Flight Conditions for Tilt-Nacelle VTOL Aircraft

Figure 6.24. Effect of Forward Speed and Inlet Contraction Ratio on Inlet Separation,  $V_\infty = 40$  KTS

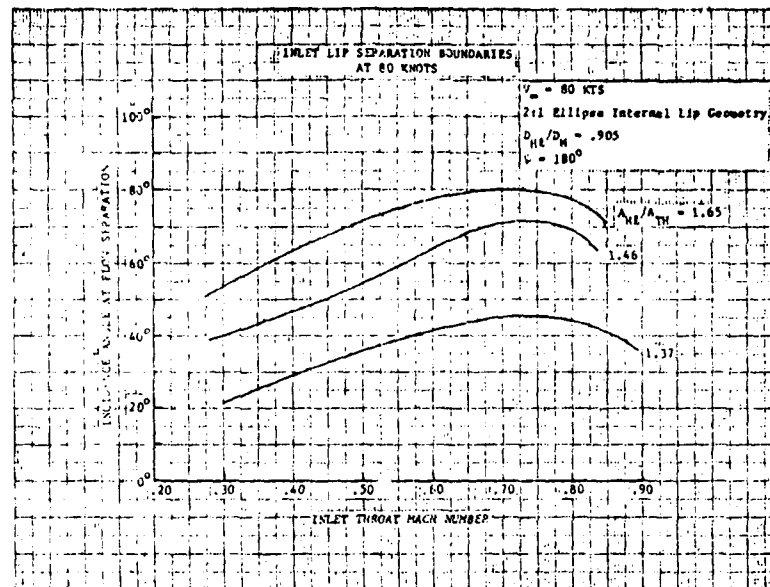


Figure 6.25. Effects of Forward Speed and Inlet Contraction Ratio on Inlet Separation,  $V_\infty = 80 \text{ KTS}$

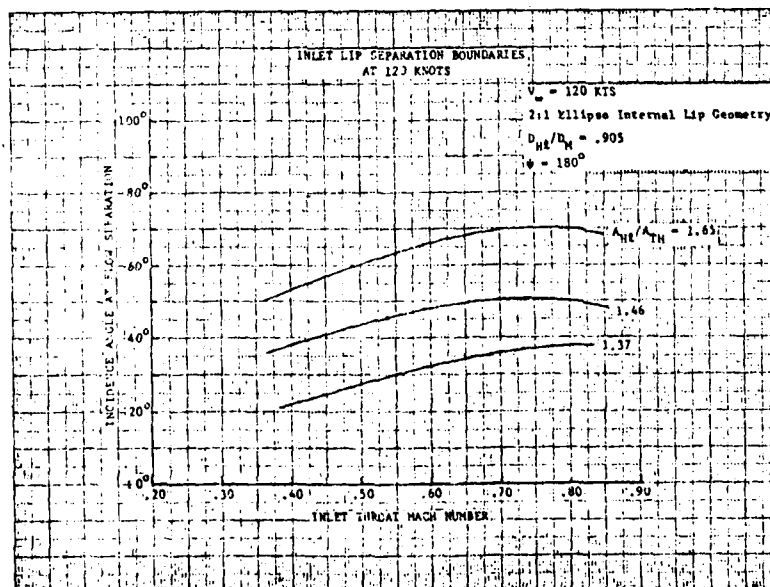


Figure 6.26. Effects of Forward Speed and Inlet Contraction Ratio on Inlet Separation,  $V_\infty = 120 \text{ KTS}$

Predicted and measured inlet separation boundaries as a function of area contraction ratio and throat Mach number are presented in Figure 6.27 at 80 KTS. The experimental data, obtained from references 6.6, 6.8 and 6.10 indicate two effects of lip thickness on inlet separation angle. First, at low contraction ratios, the inlet mass flow rate has a little effect on the separation boundary. As lip thickness is increased, performance is improved with increasing flow rate until the surface velocities on the lip get large enough to produce strong shock/boundary layer interaction effects. This phenomenon occurs at approximately  $M_{TH} = .80$  for area contraction ratios of 1.46 and 1.65, Figure 6.22. Secondly, increasing the lip thickness allows the inlet to operate at higher angles of attack at any flow rate.

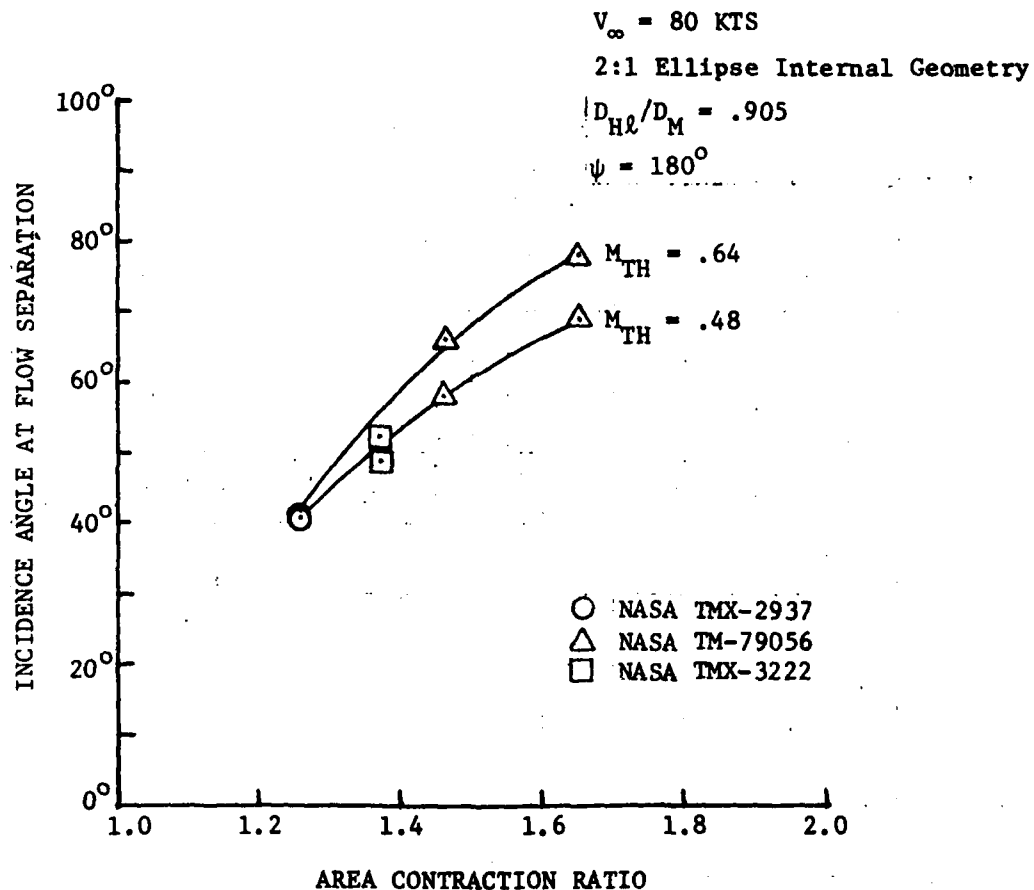


Figure 6.27. Effects of Area Contraction Ratio and Throat Mach Number on Inlet Separation

The effect of decreasing the inlet maximum diameter ratio is shown in Figure 6.28 for an area contraction ratio of 1.46, a 2:1 ellipse internal lip shape, and a forward speed of 80 KTS. These data show that decreasing the maximum diameter by 3% has a significant effect on the inlet lip separation boundary at all flow rates. This trend is also demonstrated in reference 6.6.

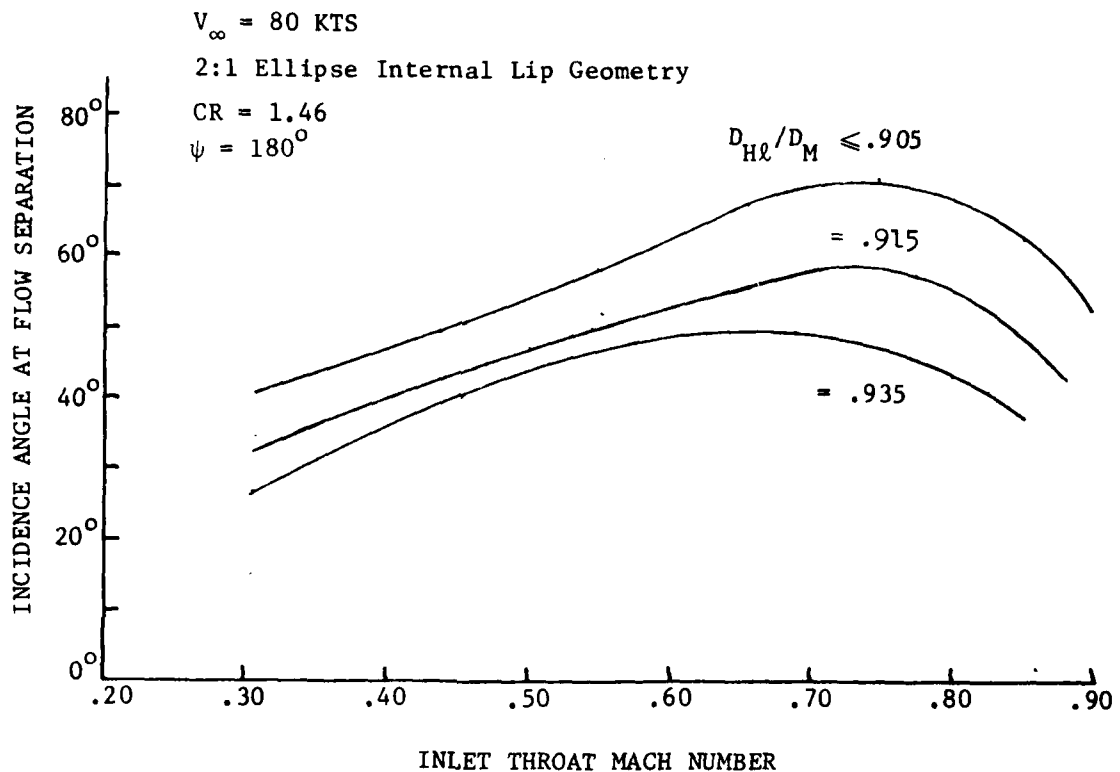


Figure 6.28. Effect of Diameter Ratio on Inlet Separation

The effect of changing the internal lip shape is presented in Figure 6.29 for an area contraction ratio of 1.46, diameter ratio of 0.905, and a forward speed of 80 KTS. In this case the internal lip shape has changed from a 2:1 ellipse to a 1.5:1 ellipse. This shortens the entry lip but maintains the same thickness. These data indicate that at low flow rates, the 1.5:1 ellipse gives substantial improvement up to a  $M_{TH} = 0.65$ . However, at higher flow rates, inlet separation performance for the 1.5:1 ellipse degrades and the 2:1 ellipse inlet is better. The inlet analysis routine accurately predicts the angle for separation in the lower throat Mach number region, but at higher flow rates where the surface velocities become large enough to cause strong shock/boundary layer interactions, the solution begins to break down and the program no longer accurately predicts the boundary layer parameters. This effect is well documented in References 6.1 and 6.5. Therefore, for inlet throat Mach numbers greater than 0.60, it should be realized that the data in Figure 6.29 could be considerably optimistic and treated accordingly.



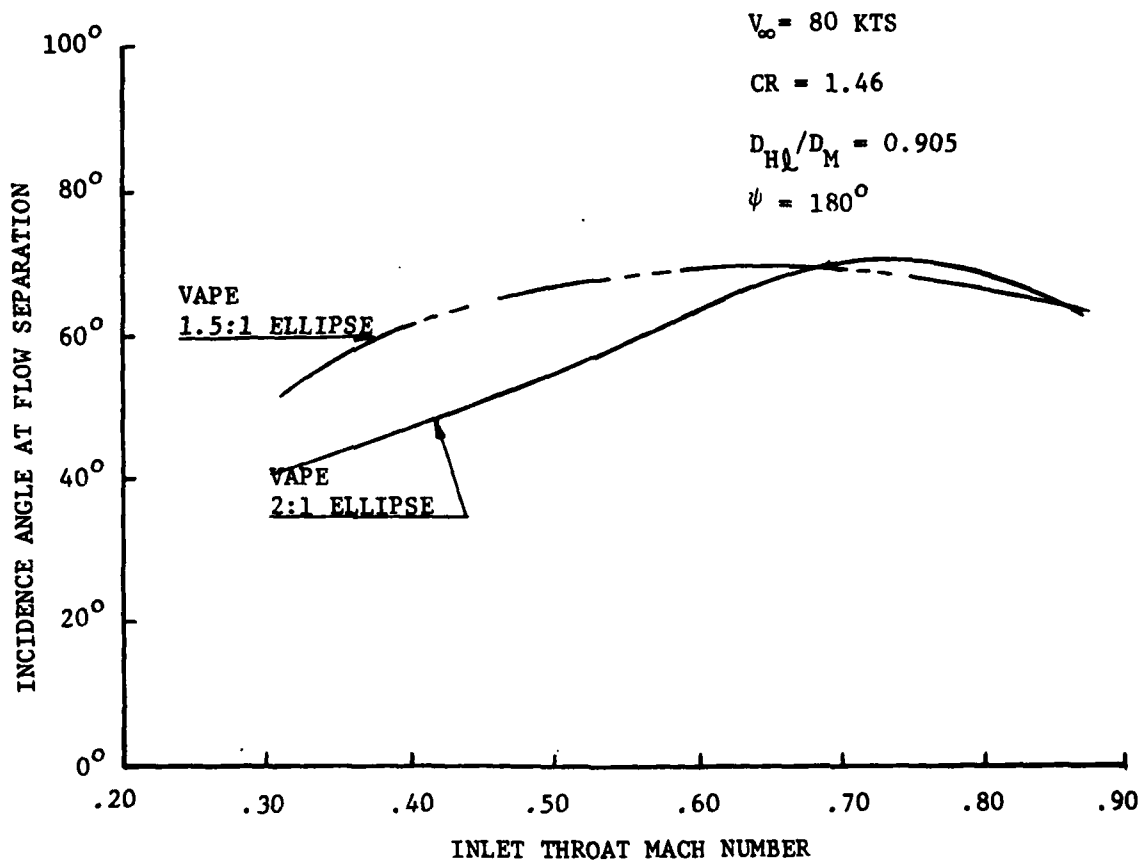


Figure 6.29. Effect of Internal Lip Shape on Inlet Separation.

## 6.3.5 EFFECT OF MODEL SCALE ON BOUNDARY LAYER SEPARATION

A study was performed to determine model scale effects on the lip separation boundaries presented in Figures 6.24 through 6.29. The QCSEE 1/6 scale model was used to conduct this analytical exercise and the results are shown in Figure 6.30. The ordinate is the ratio of incidence angle at which separation occurs for a reduced scale to the incidence angle at which separation occurred for the "full scale". The abscissa is the ratio of model scale to "full" scale. Note that a scale of 1.0 in Figure 6.30 is actually based on the QCSEE 1/6-scale model size.

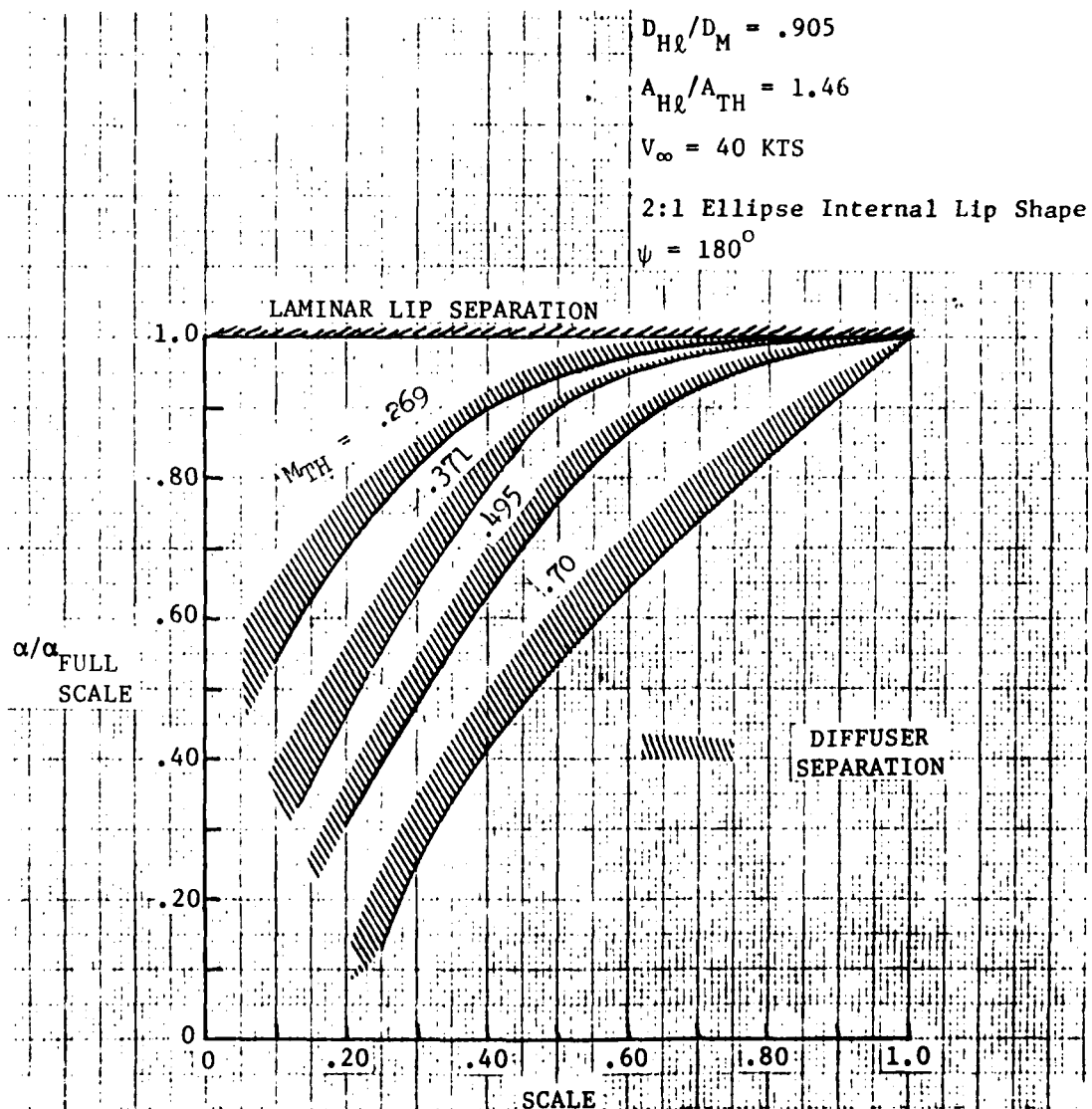


Figure 6.30. Effect of Model Scale on Inlet Separation

The following conclusions can be drawn from these data:

- (1) The relative lip separation boundary is independent of scale or mass flow rate ( $\alpha/\alpha_{FULL\ SCALE} = 1.0$  for all conditions). Therefore, the data presented in Figures 6.24 through 6.29 should apply to both large and small scale inlet configurations.
- (2) The diffuser separation boundary is a function of both scale size and mass flow rate. These data indicate that small scale inlets are able to maintain stable diffuser separation, providing a large margin between diffuser separation and lip separation. This margin increases with increasing mass flow rate. This conclusion is supported by experimental results presented in reference 6.11.

Additionally, experimental data indicate that full scale inlets are relatively intolerant of turbulent flow separation in that once turbulent (diffuser) separation is obtained, a small increase in either incidence angle or mass flow rate will cause the separation to propagate upstream resulting in laminar lip separation.

- (3) Small scale inlets will separate in the diffuser at a lower incidence angle than full scale. Figure 6.31 (reproduced from reference 6.12) shows the skin friction coefficient variations as a function of surface distance along the inlet and scale. These data show that the boundary layer buildup in the diffuser is comparatively more significant in small scale inlets (lower Reynolds number) and the flow tends toward separation as scale is decreased.

NASA TMX-73575

$M_\infty = 0.13$

$\alpha = 41^\circ$

$M_{TH} = 0.28$

WINDWARD SIDE OF INLET

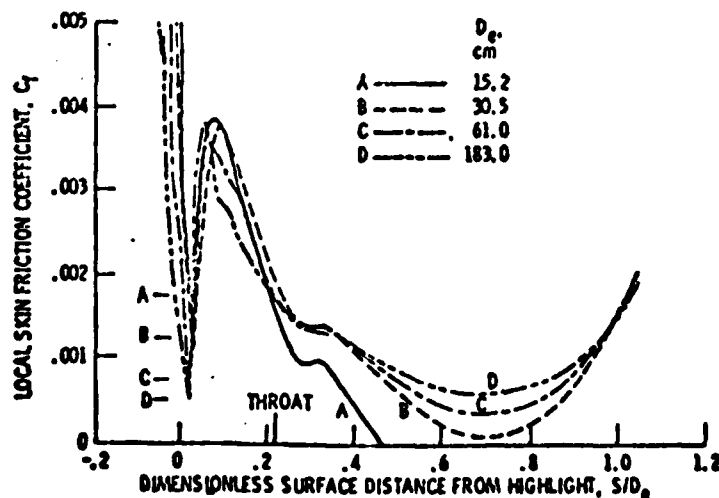
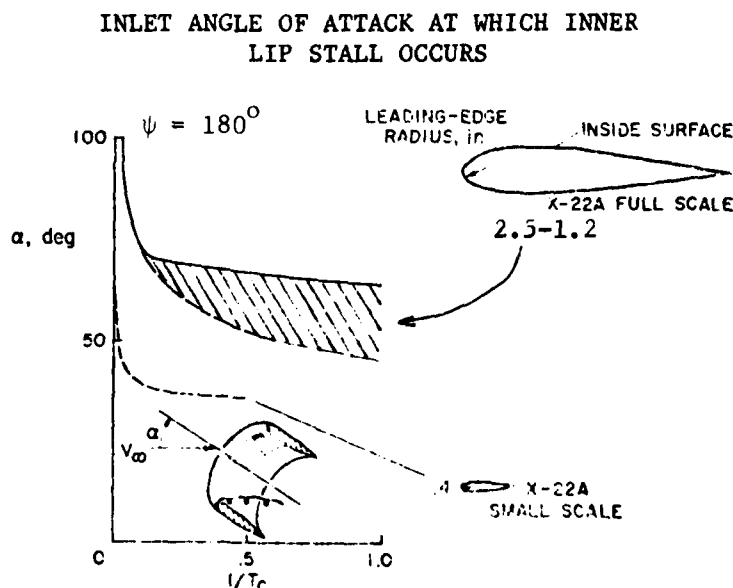


Figure 6.31. Effect of Scale on Skin Friction Coefficient.  
Windward Side of Inlet  $M_\infty = .13$ ,  $\alpha = 41^\circ$ ,  $M_T = 0.28$

- (4) As flow rate ( $M_{TH}$ ) is decreased, small scale configurations behave closer to full scale. This is also supported by experimental data presented in reference 6.11.

Data presented in Figure 6.32, (reference 6.13), show possible scale effects in laminar lip separation boundaries. The incidence angle at which lip separation occurs is plotted as a function of the inverse of thrust coefficient for a full scale tilt nacelle and an 0.4-scale model. These data indicate that there is a limiting scale size beyond which experimental results indicate a different (lower) separation boundary. The analytical procedure is not sensitive to scale effects on lip separation as seen in Figure 6.30. Since the lip separation boundaries presented in this section are based on 12 inch fan diameter models, they should be applied to inlet designs with  $D_F \geq 6$  inches. Inlet designs smaller than these should be adjusted according to available test data (see Figure 6.32).

The data of Figure 6.32 indicate that although the incidence angle at separation for the 0.4 scale model is lower than for the full-scale, the ratio  $(\alpha/\alpha_{FULL SCALE})$  is relatively constant with thrust coefficient, ( $T_c$  is a function of  $M_{TH}$ ). Therefore, the experimental data in Figure 6.32 agrees with the analytical procedure characteristic that the inlet lip separation is independent of throat mach number.



## 7.0 EXPERIMENTAL VERIFICATION

In order to substantiate the methodology developed in this study, comparisons of calculated results against experimental data were performed. The analytical methods contained in the VAPE program can be separated into two types: (1) existing methods which have been modified to improve calculation efficiency and (2) new methods which were developed during the course of this study. The methods contained in Type 1 and 2 are:

### TYPE 1:

- o Hess Three-Dimensional Potential Flow Program
- o Vought/Stockman Inlet Analysis Program
- o Vought/Wooler Jet Method

### TYPE 2:

- o Vought/Weston Jet Method
- o Thames Rectangular Jet Method
- o STOL Method
- o Inlet Force and Moment Method

The first two methods contained in Type 1 are substantiated in other documents and no additional verification was performed. The Vought/Wooler jet method, however, was not felt to be adequately substantiated for complete aircraft configurations and so some analytical/experimental correlations were performed. In Type 2, all of the methods require substantiation. In the following discussion, results of these verification studies will be presented. It should be noted that no calculations were performed using the Thames rectangular jet model on a complete airplane configuration. However, correlations with flat plate data were performed and reported in reference 5.8.

The correlations for the jet math models were performed for two aircraft configurations and a flat plate case. The two aircraft configurations were chosen based on availability and quality of the experimental test data. The two configurations selected were:

- (1) A two jet configuration tested in the NASA Langley V/STOL wind tunnel, reference 7.1.
- (2) A two/three jet configuration tested in the Ames 40' by 80' wind tunnel, reference 7.2.

Figure 7.1 is a series of computer drawn pictures of the digitized aircraft configuration of reference 7.1 as input to the VAPE program. This is a fairly simple model which required only 396 panels to accurately describe the geometry.

Figure 7.2 is a similar series of pictures of the digitized model of reference 7.2. Note that the model was much more detailed and therefore required a very careful modeling of the geometry. This configuration used all of the 650 available panels to accurately describe the geometry. For most practical cases, such a detailed description would not be required, but it does indicate the geometric complexities which can be modeled.

The flat plate used in the analysis is modeled from a configuration tested in the NASA Langley V/STOL wind tunnel by Fearn and Weston, reference 5.1. The paneling used in these calculations is shown in Figure 7.3.

The geometry used in the verification of the inlet force and moment studies will be presented later.



Figure 7.1(c)

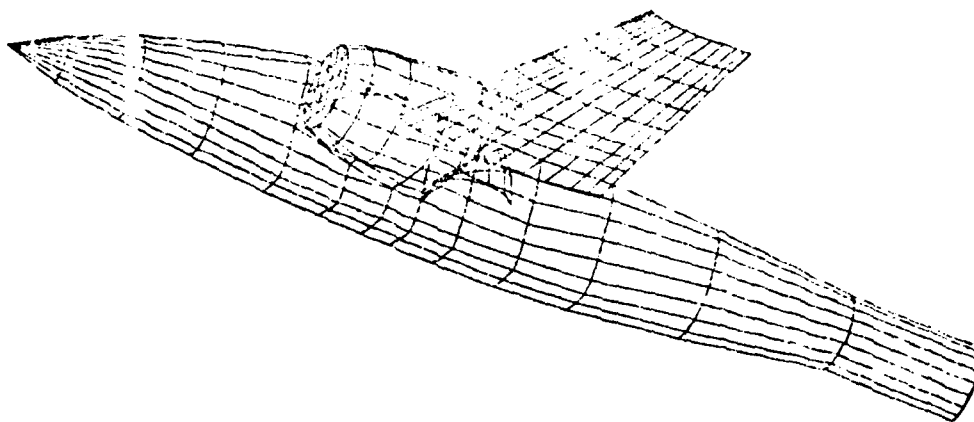


Figure 7.1(b)

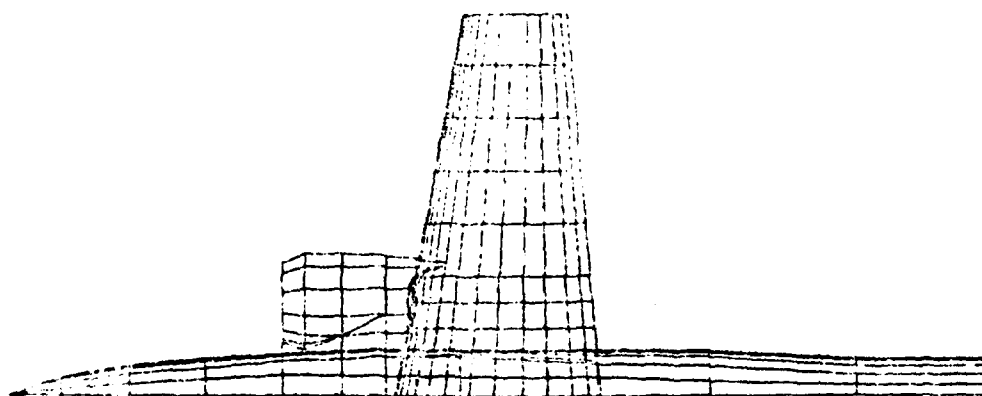


Figure 7.1(a). Geometry for Aircraft Configuration from Reference 7.1

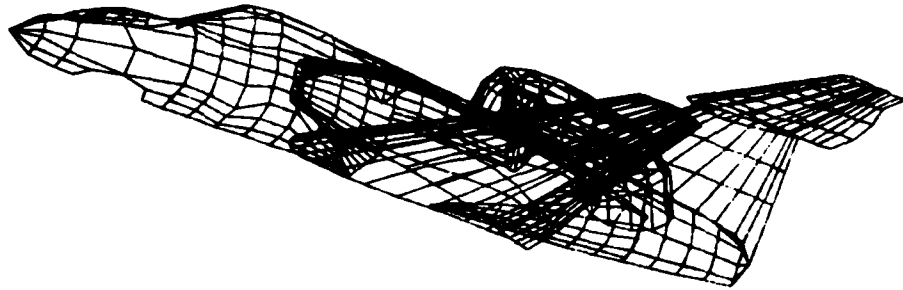


Figure 7.2(c)

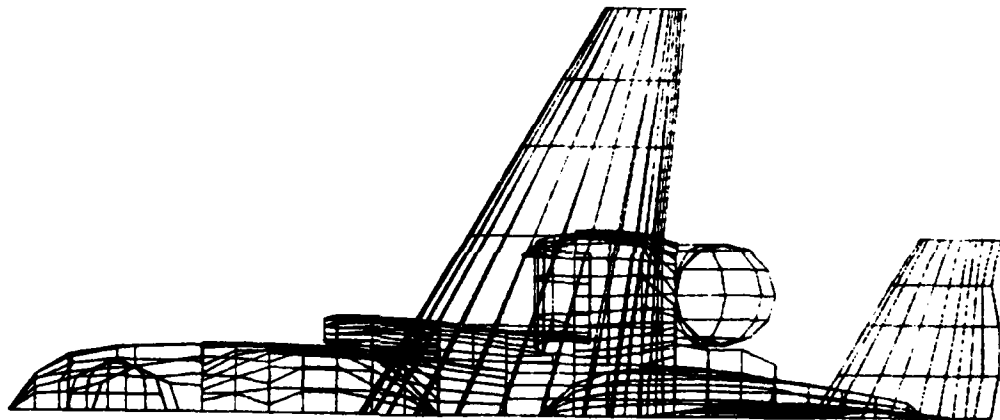


Figure 7.2(b)

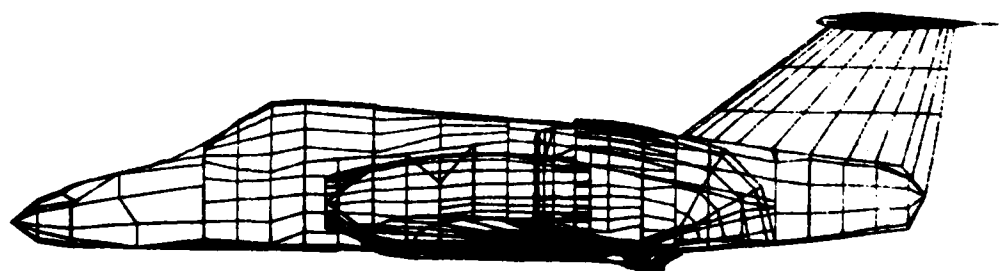


Figure 7.2(a). Geometry for Aircraft Configuration From Reference 7.2



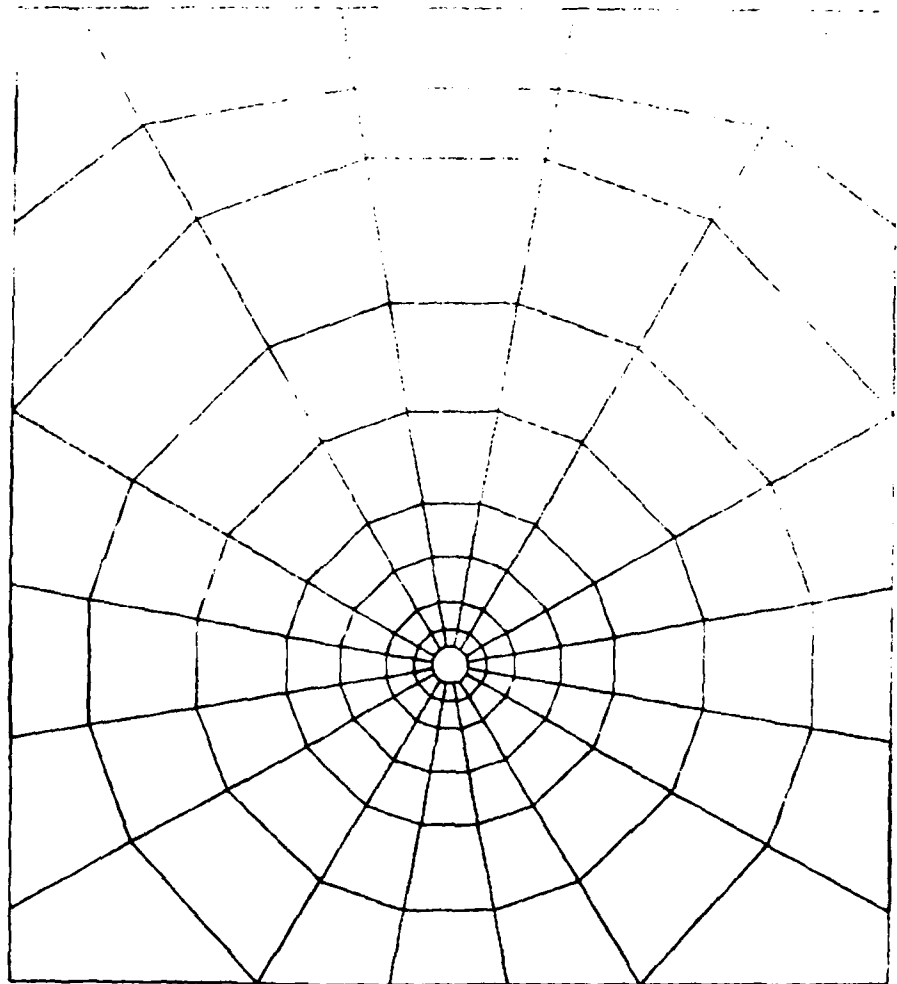


Figure 7-3. Geometry of Flat Plate Configuration

## 7.1 VERIFICATION OF VOUGHT/WOOLER JET MODEL

The Vought/Wooler jet model was verified by correlations between calculated results and experimental data for the three configurations discussed in Section 7.0. Figure 7.4 presents a comparison of pressure coefficients calculated by VAPE using the Vought/Wooler jet model to the experimental values from reference 7.3. This figure presents the pressure coefficients lying on radial lines at several meridional angles about the jet exit. The zero degree angle is upstream of the jet aligned with the free-stream. The calculated results presented in 7.4(a) through 7.4(e) show very good agreement with the experimental values. However, the comparison presented in figure 7.4(f) is poor. This discrepancy is due to the "wake" effect, i.e., a region of separated flow which exists directly downstream of the jet exit, close to the surface. The Wooler method currently will not properly model this effect and so the results in this region are not very good. It should be noted that this defect is not too serious for a large majority of aircraft configurations, since there is no surface directly aft of the nacelles. Therefore, for the cases considered below, only the forces due to the nose jet in one configuration will be suspect.

Figures 7.5 and 7.6 present force data comparisons for the model of reference 7.1 as a function of angle of attack and the inverse of the jet velocity ratio,  $R$  ( $V_{\text{freestream}}/V_{\text{jet}}$ ). The values of  $R$  range from 2 to approximately 10. At the higher values of  $R$  the comparisons are very good; however, at the lower values, the Wooler method underpredicts both the lift loss and the moment change. These results are not surprising since the test data upon which the Wooler method is based, reference 7.4, only spanned a range of  $R$  from 3 to 10. Therefore, the highest value of  $1/R$  was .3 which is where the good correlation begins to end. This indicates that the method should not be trusted at values of  $R$  lower than 3. Since most V/STOL aircraft will be operating at  $R$  values higher than 3 or 4, this limit should not penalize the method too severely.

The next configuration to be analyzed was that of reference 7.2. This model was selected because it was tested nearly full scale in the NASA Ames 40' by 80' wind tunnel and because it was representative of the Navy Type A V/STOL configurations. The model was analyzed using the Vought/Wooler jet model with all three jets operating. The results are presented in Figure 7.7 in the form of  $L/T$  versus angle of attack as a function of jet velocity ratio. The results are quite good considering the complexity of the model and the fact that viscosity on the model is ignored. This correlation is an example of how accurate the total VAPE system is in predicting total aircraft loads. It should be noted that both the experimental and analytical induced loads were positive for this configuration. That is, there was an increase lift due to the induced effects rather than a "suck down." This is normal for the location of the jets on this configuration. Reference 7.5 presents similar results on a very simple model where jet location effect on induced effects was studied.

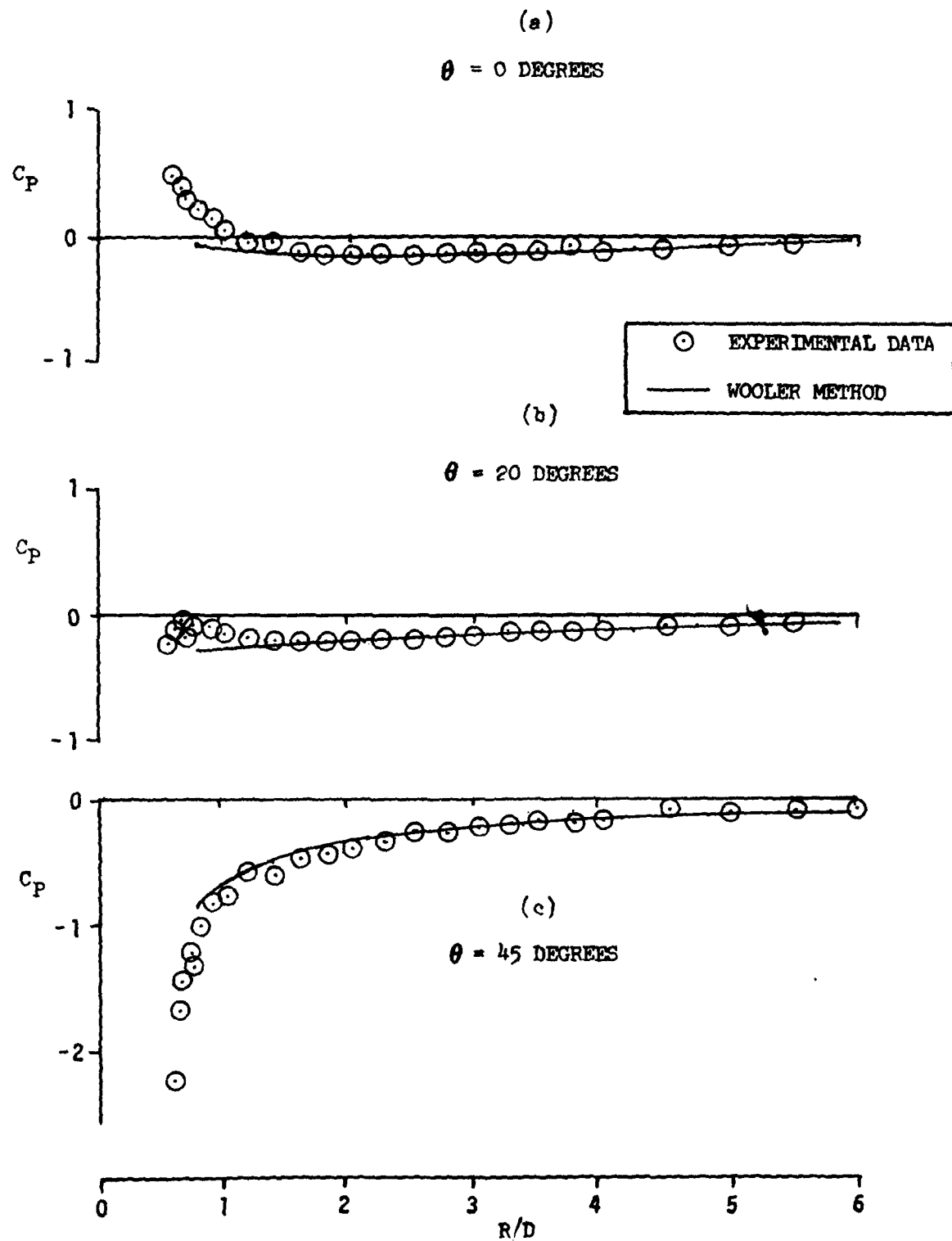


Figure 7-4. Comparison of Predicted Results from Vought/Wooler Jet Model to Experimental Data for Flat Plate Configuration

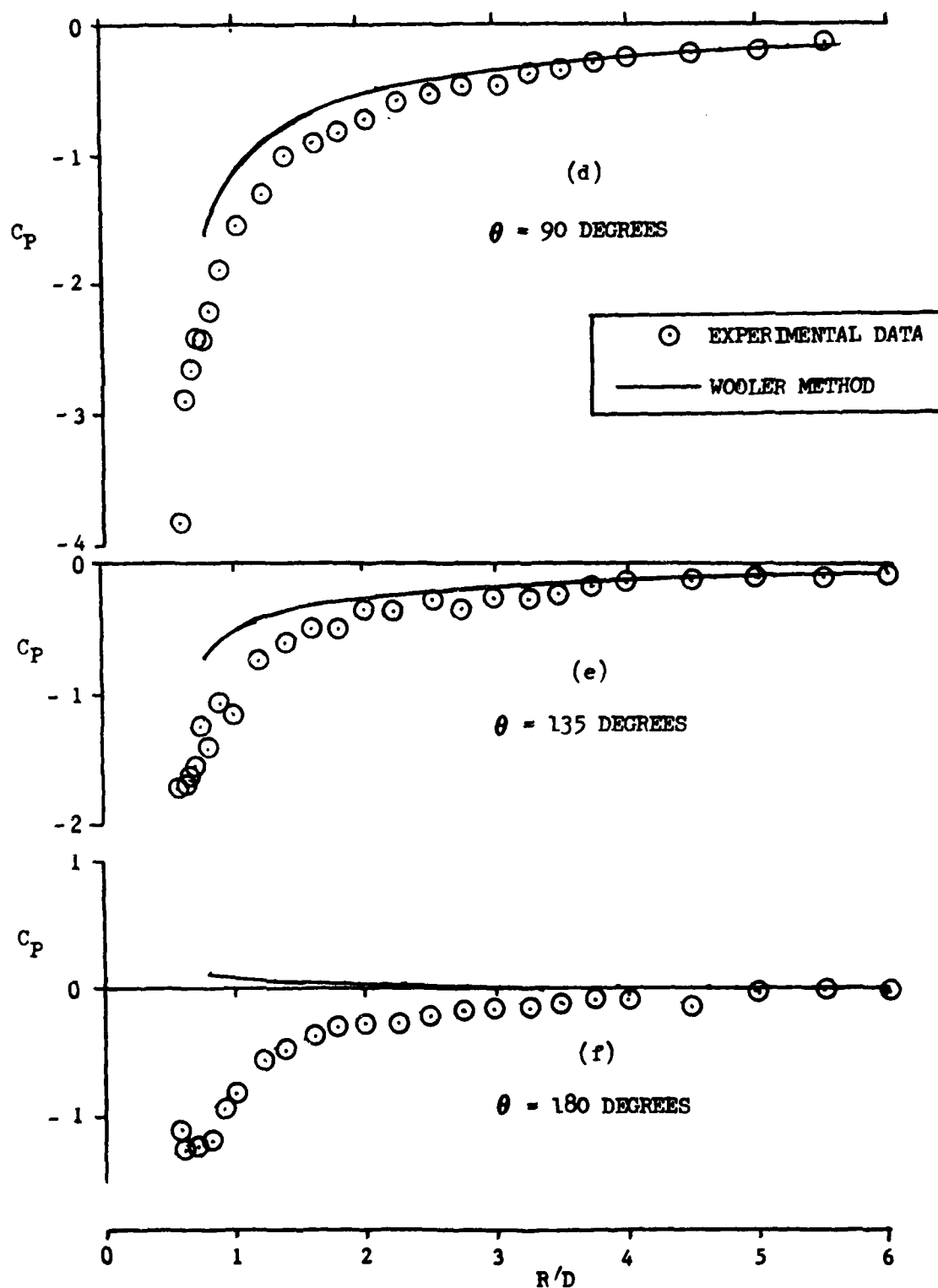


Figure 7-4. Comparison of Predicted Results from Vought/Wooler Jet Model to Experimental Data for Flat Plate Configuration

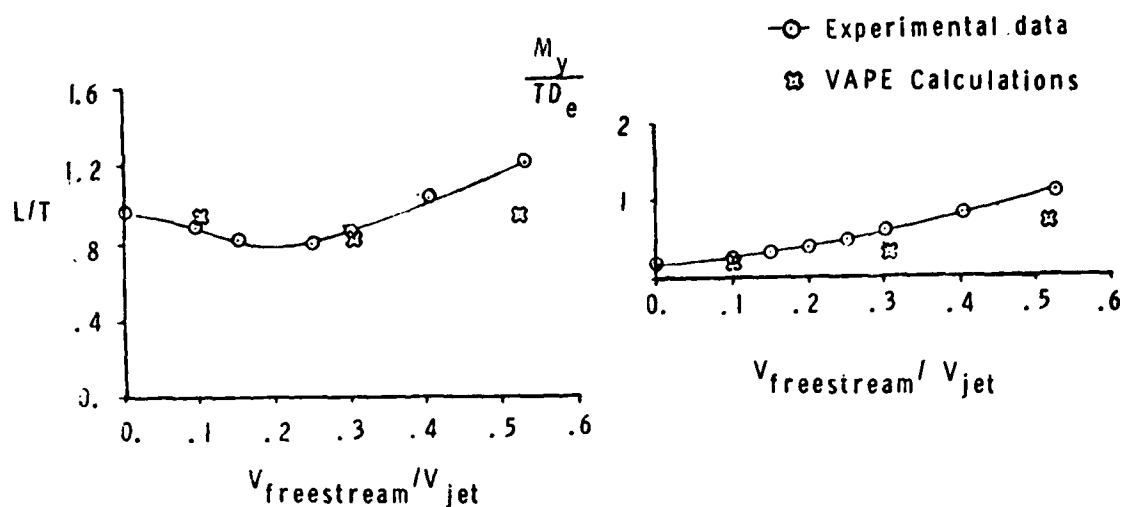


Figure 7-5. Comparison of Predicted Results from Vought/Wooler Jet Model to Experimental Data for the Configuration of Figure 7-1.  $\alpha = 0$  degrees

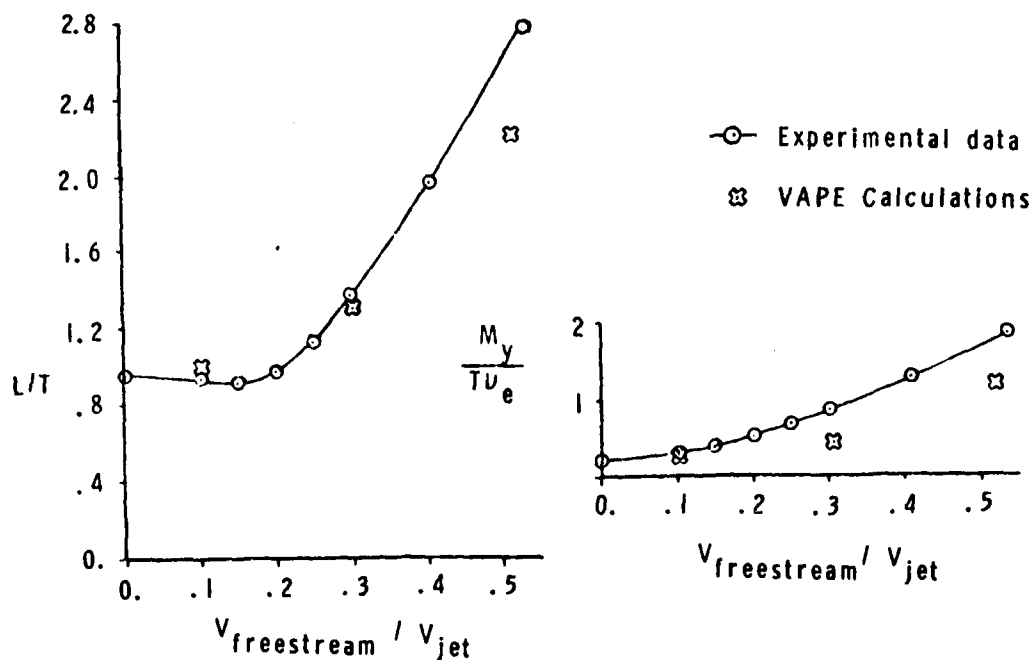


Figure 7-6. Comparison of Predicted Results from Vought/Wooler Jet Model to Experimental Data for the Configuration of Figure 7-1.  $\alpha = 10$  degrees

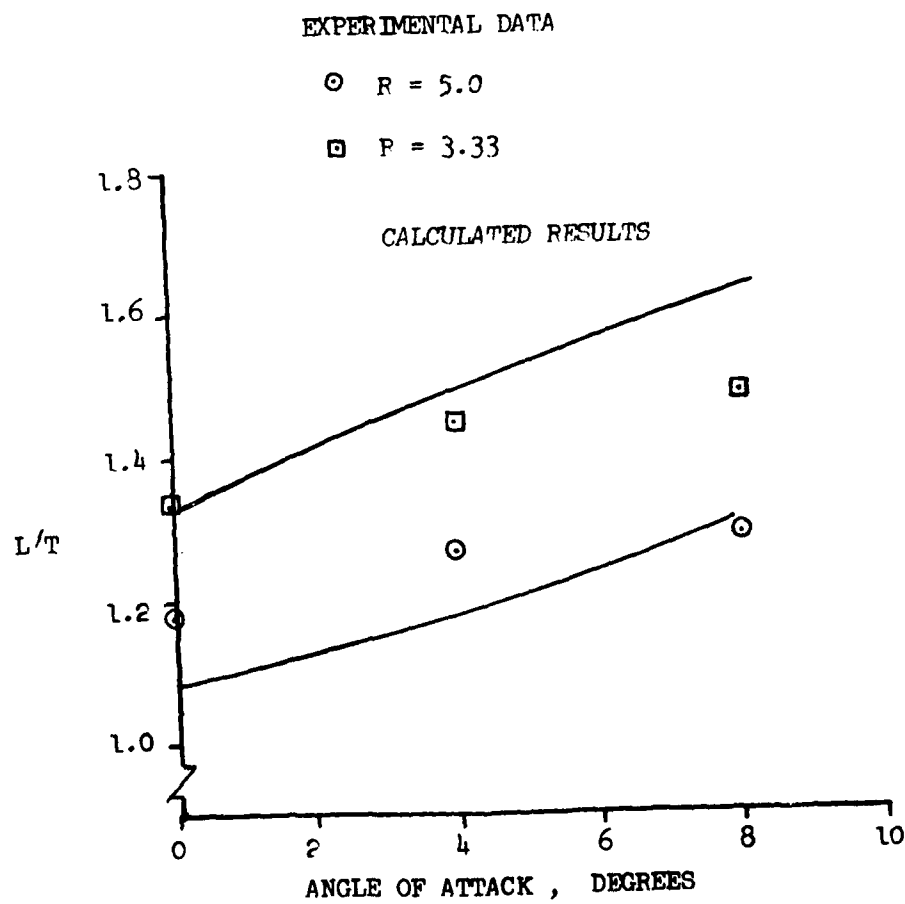


Figure 7-7. Comparison of Predicted Results from Vought/Wooler Jet Model to Experimental Data for the Configuration of Figure 7-2.

## 7.2 VERIFICATION OF VOUGHT/WESTON JET MODEL

The Vought/Weston jet model was verified by correlations between calculated results and experimental data for two of the configurations discussed in Section 7.0.

The first case considered was the flat plate configuration presented in Figure 7.3. The Vought/Weston jet model was used to generate results using the same conditions as specified for the Vought/Wooler case presented in Figure 7.4. Figure 7.8 presents the comparisons of calculated results with experimental data for several meridional angles. The correlation is similar to that obtained with the Wooler model. Again, the only poor results were obtained in the wake region. Modifications were made to this method in an attempt to improve the calculations in this wake region. However, as discussed in section 5.2.4, no reliable approach was found.

The second configuration analyzed was that of reference 7.1. Figure 7.9 and 7.10 present force data comparisons similar to those presented for the Vought/Wooler method in Figures 7.5 and 7.6. As can be observed, the results are quite good for this two-jet case. It should be noted that as discussed in Section 5.2.2, this case due to the geometric location of the jets, is treated as a single jet case in the Vought/Weston model as discussed in Section 8.

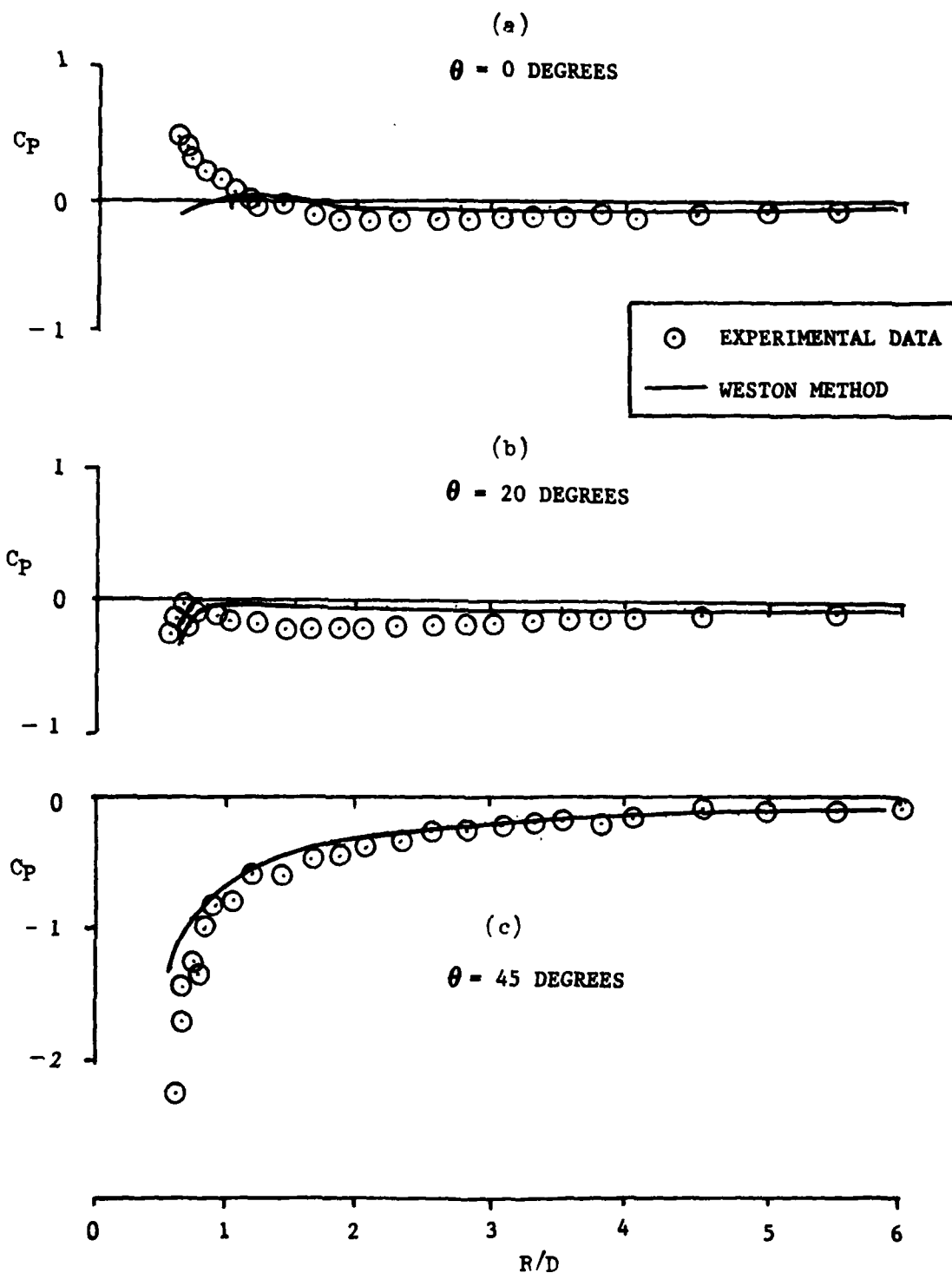


Figure 7-8. Comparison of Predicted Results from Vought/Weston Jet Model to Experimental Data for the Flat Plate Configuration of Figure 7-3.



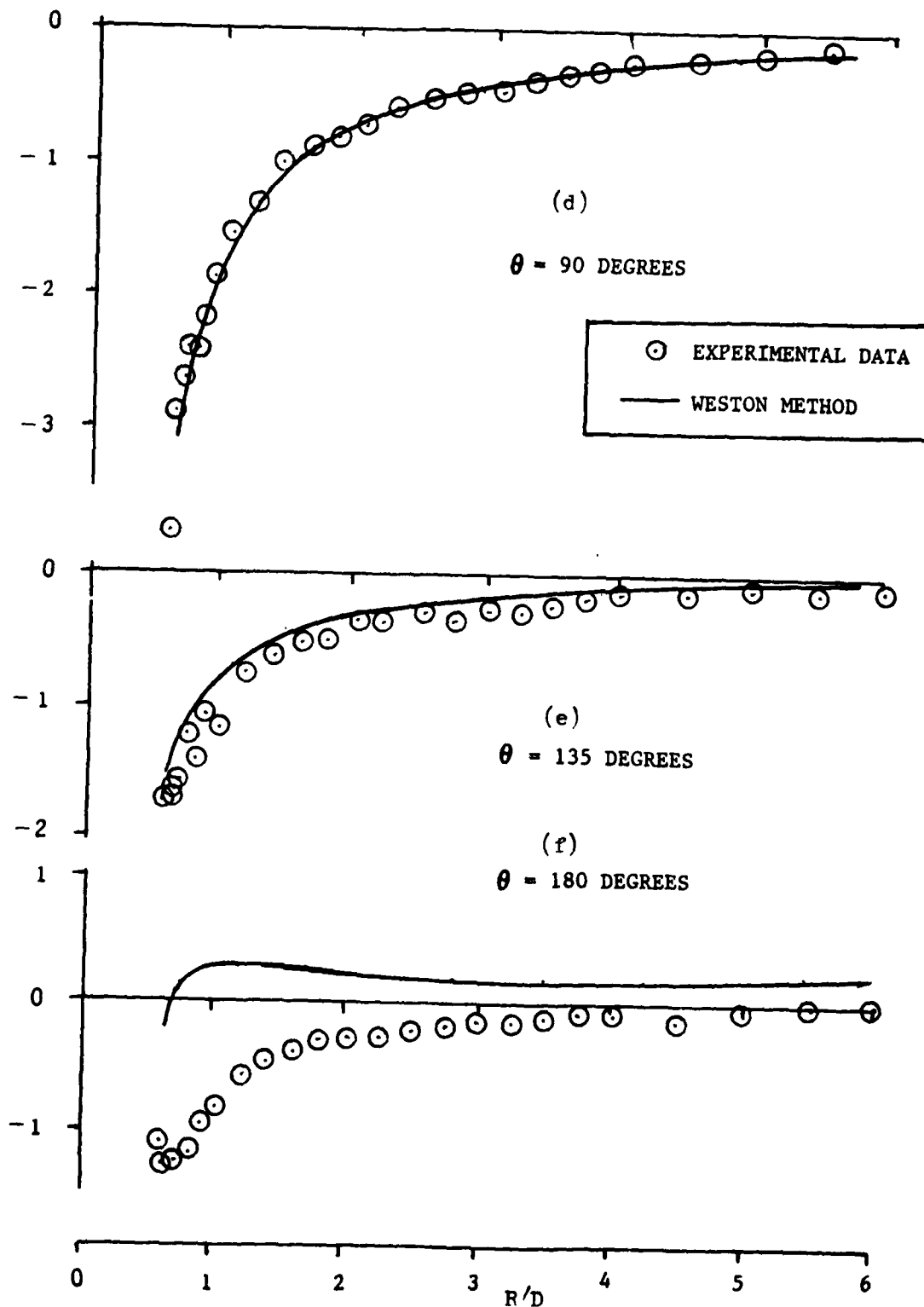


Figure 7-8. Comparison of Predicted Results from Vought/Wooler Jet Model to Experimental Data for the Configuration of Figure 7-3

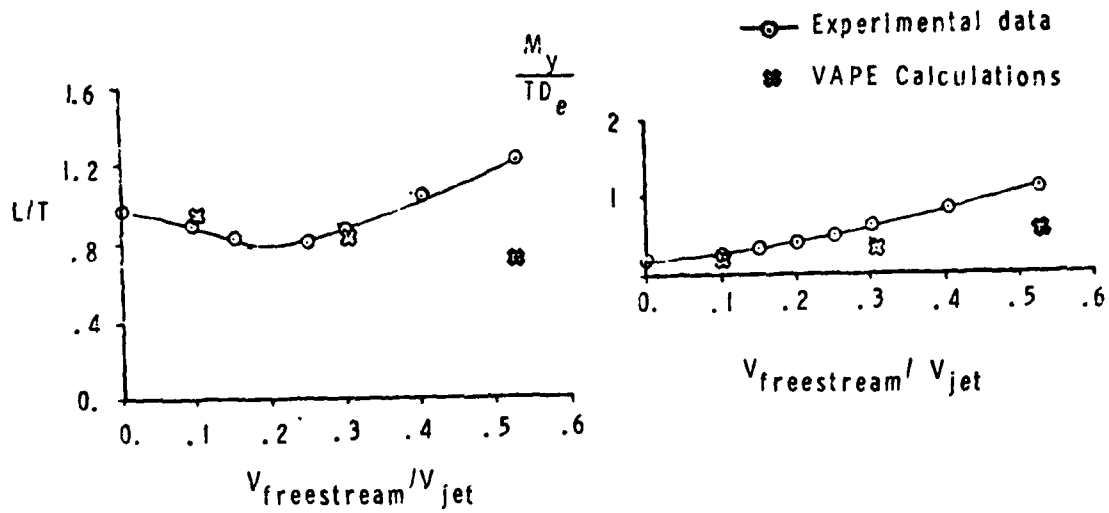


Figure 7-9. Comparison of Predicted Results from Vought/Weston Jet Model to Experimental Data for the Configuration of Figure 7-1.

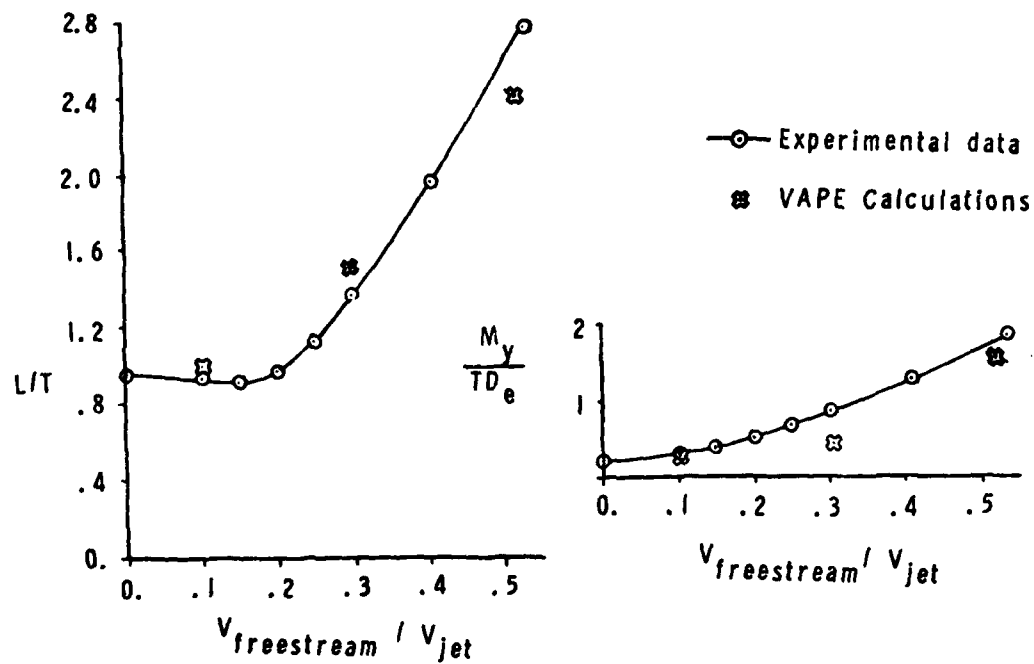


Figure 7-10. Comparison of Predicted Results from Vought/Weston Jet Model to Experimental Data for the Configuration of Figure 7-1.

### 7.3 VERIFICATION OF FORCE AND MOMENT METHOD

Direct comparison of predicted inlet force and moment data to experimental results is very difficult. Most data has been collected using an airplane or nacelle model where the aerodynamic and propulsion induced effects are included in the measured forces and moments. These effects are difficult, and at times impossible, to separate from the raw data in order to obtain the true inlet force and moments. Nevertheless, a predicted versus experimental data comparison on an order of magnitude basis is possible, showing that the calculated force and moment data trends are consistent with experimental data. Such a comparison is shown in Figure 7.11 where predicted ram moment arm is presented with experimental data from references 6.11 and 7.6. These data show that the ram moment arm is less than one diameter, and more importantly, reference 7.7 shows that the inlet contribution is small. References 6.11 and 7.6 contain data for tilt nacelle alone cases. Reference 6.11 suggests that the aerodynamic side force on the nacelle contributes significantly to the nacelle pitching moment. The side force will produce a moment that will add to the inlet effect and cause the moment arm to be greater. This could explain most of the difference between nacelle force and moment data and the predicted results. At this angle of attack (90 degrees), geometric differences and the effect of the exhaust plume are believed to be a second order effect.

In conclusion, the predicted force and moment data appears to compare reasonably well with experimental data for this particular case. Inlet effects contribute approximately half of the total nacelle pitching moment, the other half is largely a result of the side force on the nacelle. Geometric and exhaust plume effects are believed to be a second order effect although this hypothesis needs to be verified through further analysis and test.

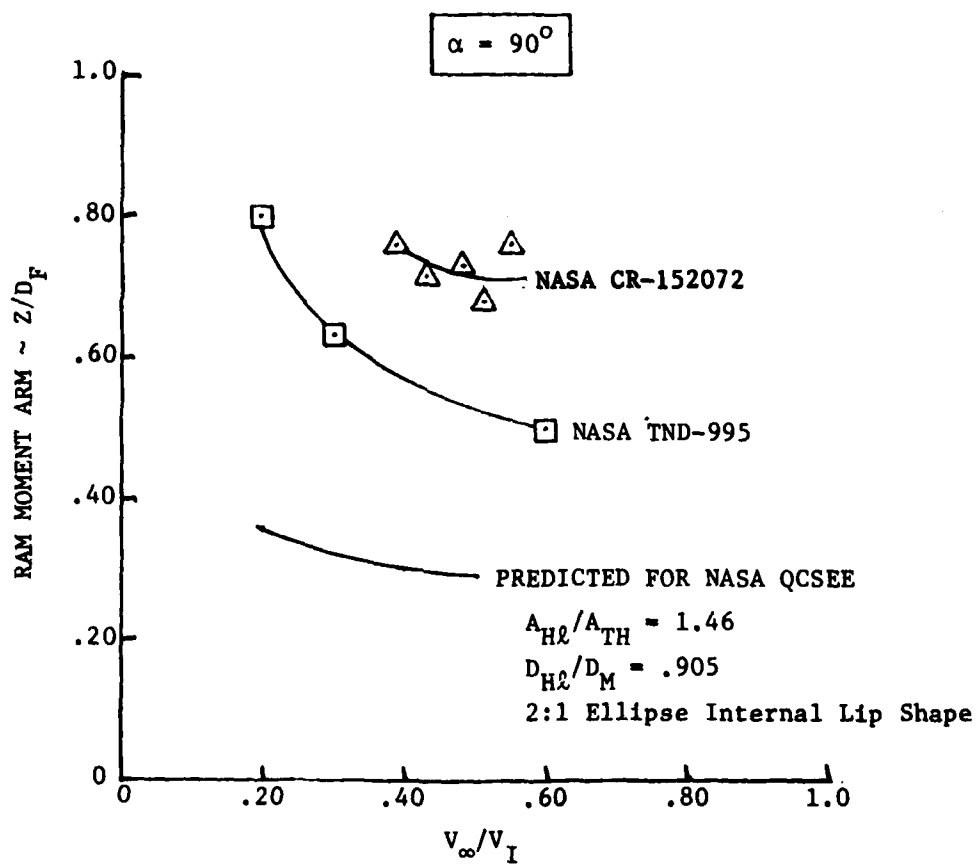


Figure 7-11. Comparison of Predicted Inlet Ram Moment Arm to Experimental Nacelle Data

## 8.0 CONCLUSIONS AND RECOMMENDATIONS

The VAPE program is one of the most comprehensive methods available for determining the propulsive induced effects on V/STOL aircraft. The VAPE program is capable of evaluating:

- o Effects of relative wind about an aircraft
  - From 85 KTS to  $M = .5$  approximately
- o Effects of propulsive lift jet entrainment and flow blockage
  - Jet velocity ratios -  $3 \leq R \leq 10$
  - Jet deflection angles -  $30^\circ \leq \delta_j \leq 105^\circ$
  - Multiple jets - linear superposition
  - Rectangular or circular jet exit
- o Effects of engine inlet suction on the aircraft flow field
  - Range of inlet angle of attack
  - Range of mass flow
  - Limited to axisymmetric inlets
  - Variable inlet velocity flow field calculated on inlet face for proper modeling of inlet
- o Determination of engine inlet forces and moments including inlet separation prediction capability
  - Laminar inlet separation
  - Turbulent diffuser separation
  - Forces and moments on inlet determined
  - Ram drag moment arm predicted

The VAPE program is a very powerful tool that combines the best techniques available for analyzing various parts of a V/STOL configuration into one unified computer program. In addition, since the code is modular in construction, new techniques can be added with a minimum of effort.

Additional work is needed in several areas to either improve the existing analytical methods or to include additional methods which would increase the programs usefulness.

The basic component of the program is currently the Hess three-dimensional potential flow method which is utilized due to its ability to analyze any arbitrary configuration. However, this method is also very

expensive in terms of computer costs and manpower required to develop the proper input modeling. These costs are acceptable when a very complicated configuration (see Figure 7.2) is to be analyzed. But, in preliminary design of a configuration, it is desirable to analyze various jet locations in order to optimize the jet induced effects. Therefore, it would be beneficial if a vortex lattice code were added to the VAPE program for performing this preliminary design task. Vortex lattice codes will not be as accurate as the Hess program, especially in the fuselage region, but they will give reasonable results at a small fraction of the cost associated with the Hess method. The inlet analysis module can be improved in several different ways to increase its capability as a subsonic inlet design tool. One improvement would be replacing the current axisymmetric Stockman routine with the new three-dimensional version that has recently been developed. Since several inlets for V/STOL application are asymmetric in order to optimize both cruise and V/TOL performance, reference 8.1, analysis with the current Stockman version in the combined routine is rather limited. The three-dimensional version would allow the entire inlet to be analyzed at once as opposed to solving the inlet in parts and attempting to superimpose the solutions.

Another improvement would be a better model of the flow after separation occurs. Presently, the displacement thickness is assumed constant following separation. This assumption allows more diffusion after predicted separation than has been found in applicable test data. Albers and Felderman, reference 8.2, recommend an extrapolation procedure that may be better than the current model.

Finally, the viscous routine neglects shock interactions. Since many of the high incidence angle cases contain regions of local supersonic flow, it is necessary to account for possible shock-boundary layer interactions in the calculations. Furthermore, the transition model does not predict separation bubbles that appear to be present in experimental data, especially small scale. However, it may be feasible to include the predictions or a separation bubble in an improved transition model. Additionally, in Stockman, the boundary layer solution is started at the inlet highlight instead of the stagnation point. The program should be modified to include the laminar flow characteristic in this region since it is important to the boundary layer values determined at the lip and in the diffuser.

Several improvements can be identified for the jet methods contained in VAPE. Most of these improvements depend on the acquisition of wind tunnel data for multiple jet cases. The data base for single jets from which the Weston model was developed is very comprehensive. However, no comparable data base exists for multiple jets, therefore, if the extension of the Weston method to multiple jets is to be made as effective as the single jet model, additional test data similar to that of reference 5.6 must be obtained.

In both the Weston method and the Wooler method additional test data is needed at lower and higher values of  $R$  to extend the methods applicability.

A wake effect model is needed in all of the jet methods to improve the calculations on surfaces aft of the jet. Again, the development of an effective model for the wake hinges on obtaining good applicable test data.

The rectangular jet model needs to be extended to application to multiple jets. This can only be done when appropriate test data is obtained.

In summary, there are several improvements which can be made to the analytical methods by the installation of improved methodology. However, improvements in the jet math models are almost completely dependent on the acquisition of appropriate wind tunnel test data.

## 9.0 REFERENCES

- 4.1 Hill, W.G. Jr., and Jenkins, R.C., "A Study of Upwash Impingement on the Vehicle for a Two Jet type A Design," paper presented at Navy V/STOL Aerodynamics Workshop, Monterrey, Calif., May 16-18, 1979. Proceedings soon to be published.
- 4.2 Hess, J.L., "The Problem of Three-Dimensional Lifting Potential Flow and its Solution by Means of Surface Singularity Distribution," Computer Methods in Applied Mechanics and Engineering, Vol. 4, 1974, North Holland Publishing Co.
- 4.3 Hess, J.L., "Calculation of Potential Flow About Arbitrary Three-Dimensional Lifting Bodies," Final Technical Report, McDonnell Douglas Report No. MDC 55679-01, (Oct. 1972), also AD755480.
- 4.4 Hess, J.L., "Numerical Solution of the Integral Equation for the Neumann Problem with Application to Aircraft and Ships," Douglas Aircraft Company Engineering Paper No. 5987 (Oct. 1971).
- 4.5 Hess, J.L., and Smith, A.M.O., "Calculation of Nonlifting Potential Flow About Arbitrary Three-Dimensional Bodies," Douglas Aircraft Company Report No. ES 40622 (March 1962). (An abbreviated version appeared in Journal of Ship Research, Vol. 8, No. 2 (September 1964).)
- 4.6 Rubbert, P.E. and Saaris, G.R., "Review and Evaluation of a Three-Dimensional Lifting Potential Flow Analysis Method for Arbitrary Configurations," AIAA Paper No. 72-188 (January 1972).
- 4.7 Labrujere, Th.E., Loeve, W. and Sloof, J.W., "An Approximate Method for the Calculation of the Pressure Distribution on Wing-Body Combinations at Subcritical Speeds," AGARD Conference Proceedings No. 71, Aerodynamic Interference (September 1970).
- 4.8 Kraus, W., "Das MBB-UFE Unterschall-Panelverfahren, Teil 2: Das Auftriebsbehaftete Verdrängungsproblem in Kompressibler Strömung," UFE 633-70 (1970).
- 4.9 Hess, J.L., "Calculation of Potential Flow About Arbitrary Three-Dimensional Lifting Bodies," Phase II, Final Report. McDonnell Douglas Report No. MDC J0971-01 (October 1970).
- 4.10 Hess, J.L., "Calculation of Potential Flow About Arbitrary Three-Dimensional Lifting Bodies," Phase I, Final Report. McDonnell Douglas Report No. MDC J0545 (December 1969).
- 5.1 Weston, Robert P., "A Description of the Vortex Pair Associated with a Jet in a Crossflow," presented at Navy Workshop on Prediction Methods for Jet V/STOL Propulsion Aerodynamics, Washington, D.C. (July 28-31, 1975).



- 5.2 Wooler, P.T., Kao, H.C., Schwendemann, M.F., Wasson, H.R., and Ziegler, H., "V/STOL Aircraft Aerodynamic Prediction Methods Investigation, Volume I. Theoretical Development of Prediction Methods," Air Force Flight Dynamics Laboratory, AFFDL-TR-72-26, Volume I (January 1972).
- 5.3 Wooler, P.T., Burghart, G.H. and Gallagher, J.T., "Pressure Distribution on a Rectangular Wing with a Jet Exhausting Normally into an Airstream," Journal of Aircraft, Vol. 4, No. 6, pp. 537-543 (Nov.-Dec. 1967).
- 5.4 Wu, J.C., McMahon, H.M., Mosher, D.K. and Wright, M.A., "Experimental and Analytical Investigations of Jets Exhausting into a Deflecting Stream," Journal of Aircraft, Vol. 7, No. 1, pp. 44-51 (Jan.-Feb. 1970).
- 5.5 Wooler, P.T. and Ziegler, H., "An Analytical Model for the Flow of Multiple Jets into an Arbitrary Directed Crossflow in Ghroud Effect," AIAA Paper 70-545 presented at the AIAA Atmospheric Flight Mechanics Conference, Tullahoma, Tenn. (1970).
- 5.6 Fearn, R. and Weston, R.P., "Vorticity Associated with a Jet in a Crossflow," AIAA Journal, Vol. 12, Number 12 (Dec. 1974).
- 5.7 Dietz, W.E., "A Method for Calculating the Induced Pressure Distribution Associated with a Jet in a Crossflow," Master's Thesis, University of Florida, Gainesville, Florida (1975).
- 5.8 Thames, F.C. and Weston, R.P., "Development of an Analytical Model to Predict Induced Effects on Aspect Ratio 4.0 Rectangular Nozzles in a Subsonic Crossflow," soon to be published NASA TM. Work performed for NASA LRC and NADC by Vought Corp.
- 5.9 Sellers, W.L., "A Model for the Vortex Pair Associated with a Jet in a Crossflow," Master's Thesis, University of Florida (1975).
- 5.10 Fearn, R.L., Krausche, D. and Weston, R.P., "A Round Jet in a Crossflow - The Influence of Jet Injection Angle on Vortex Properties," to be published by AIAA.
- 5.11 Albertson, M.L., et al, "Diffusion of Submerged Jets," ASCE Transactions, No. 2409 (December 1948).
- 5.12 Ricou, F.P. and Spaulding, D.B., "Measurements of Entrainment by Axisymmetrical Turbulent Jets," Journal of Fluid Mechanics, 11:21 (1961).
- 5.13 Saha, P., "Characteristics of a Round Turbulent Free Jet," Master's Thesis, University of Florida, Gainesville, Florida (1975).
- 5.14 Keffer, S.F., "The Physical Nature of the Subsonic Jet in a Cross-stream," NASA SP-218, (Sept. 1969).
- 5.15 Fearn, R., "Mass Entrainment of a Circular Jet in a Crossflow," NASA SP-218 (Sept. 1969).

- 5.16 Fricke, L.B., Wooler, P.T. and Ziegler, H., "A Wind Tunnel Investigation of Jets Exhausting into a Crossflow," Air Force Flight Dynamics Laboratory Technical Report, AFFDL-TR-70-154, Volumes I-IV (Dec. 1970).
- 5.17 Kotansky, D.R., Durando, J.A. and Bristol, D.R., "Multi-Jet Induced Forces and Moments on VTOL Aircraft Hovering In and Out of Ground Effect," Naval Air Development Center, Report No. NADC-77-229-30 (June 1977).
- 5.18 Siclari, M.J., Barche, J. and Migdal, D., "V/STOL Aircraft Prediction Technique Development for Jet-Induced Effects," Naval and Propulsion Test Center Report No. PDR-623-18 (April 1975).
- 5.19 Colin, P.E. and Olivari, D., "The Impingement of a Circular Jet Normal to a Flat Surface With and Without Crossflow," AD688953 (Jan. 1969).
- 6.1 Stockman, N.O., "Potential and Viscous Flow in VTOL, STOL, or CTOL Propulsion System Inlets," AIAA Paper No. 75-1186 (Sept. 1975).
- 6.2 Hess, J.L. and Smith, A.M.O., "Calculation of Potential Flow About Arbitrary Bodies," Progress in Aeronautical Science, Vol. 8, Pergamon Press (1967).
- 6.3 Albers, J.A. and Gregg, J.L., "A Computer Program to Calculate Laminar, Transitional and Turbulent Boundary Layers for Compressible Axisymmetric Flow," NASA TND-7521 (1974).
- 6.4 Lieblein, S. and Stockman, N.O., "Calculation Correction for Internal Flow Solutions," Journal of Aircraft, Vol. 9, No. 4 (April 1972).
- 6.5 Ybarra, A.H., Rhoades, W.W. and Stockman, N.O., "A Combined Potential and Viscous Flow Solution for V/STOL Engine Inlets," AIAA Paper No. 78-142 (Jan. 1978).
- 6.6 Miller, B.A., Dastol, B.J. and Wesoky, H.L., "Effect of Entry Lip Design on Aerodynamics and Acoustics of High Throat Mach Number Inlets for the Quiet, Clean, Short-Haul Experimental Engine," NASA TMX-3222 (1975).
- 6.7 Albers, J.A. and Felderman, E.J., "Boundary Layer Analysis of Subsonic Inlet Diffuser Geometries for Engine Nacelles," NASA TN-D-7520 (1974).
- 6.8 Burley, R.R., "Effect of Lip and Centerbody Geometry on Aerodynamic Performance of Inlets for Tilting-Nacelle VTOL Aircraft," NASA TM-79056 (Jan. 1979).
- 6.9 Luidens, R.W. and Abbott, J.M., "Incidence Angle Bounds for Lip Flow Separation of the 13.97-Centimeter Diameter Inlets," NASA TMX-3351 (Feb. 1976).
- 6.10 Albers, J.A., "Comparison of Predicted and Measured Low-Speed Performance of Two 51-Centimeter Diameter Inlets at Incidence Angle," NASA TMX-2937 (Nov. 1973).

- 6.11 Syberg, J., "Low Speed Test of a High Bypass Ratio Propulsion System with an Asymmetric Inlet Designed for a Tilt-Nacelle V/STOL Airplane," NASA CR-152072 (Jan. 1978).
- 6.12 Chou, D.C., Luidens, R.W. and Stockman, N.O., "Prediction of Laminar and turbulent Boundary Layer Flow Separation in V/STOL Engine Inlets," NASA TMX-73575 (Jan. 1977).
- 6.13 Mort, K.W., "Summary of Large Scale Tests of Ducted Fans," NASA SP116 (Apr. 1966)
- 7.1 Mineck, R.E. and Schwendemann, M.F., "Aerodynamic Characteristics of a Vectored-Thrust V/STOL Fighter in the Transition Speed Range," NASA TND-7191 (May 1973).
- 7.2 Sambucci, B.J., Aoyagi, K. and Rolls, L.J., "Wind Tunnel Investigation of a Large-Scale Model of a Lift/Cruise Fan V/STOL Aircraft," NASA TMX-73139 (May 1976).
- 7.3 Fearn, R.L. and Weston, R.P., "Induced Pressure Distribution of a Jet in a Crossflow," NASA TN-D-7916 (July 1975).
- 7.4 Fricke, L.B., Wooler, P.T. and Ziegler, H., "A Wind Tunnel Investigation of Jets Exhausting Into a Crossflow," Vol. , AFFDL-TR-70-154 (Dec. 1970).
- 7.5 Margason, R.J. and Fearn, R., "Jet-Wake Characteristics and Their Induced Aerodynamic Effects on V/STOL Aircraft in Transition Flight," NASA SP-218 (Sept. 1969).
- 7.6 Grundwald, K.J. and Gnoodson, K.W., "Aerodynamic Loads on an Isolated Shrouded Propellor Configuration for Angles of Attack From  $-10^{\circ}$  to  $110^{\circ}$ , NASA TND-995, (1962).
- 7.7 Kuhn, Richard E. and McKinney, M.D., "NASA Research on the Aerodynamics of Jet VTOL Engine Installations", Agardograph 103, (1965).
- 8.1 Luidens, R.W., Stockman, N.O. and Diedrick, J.H., "An Approach to Optimum Subsonic Inlet Design," NASA TM 79051 (March 1979).
- 8.2 Felderman, E.J. and Albers, J.A., "Comparison of Experimental and Theoretical Boundary Layer Separation for Inlets at Incidence Angle at Low-Speed Conditions," NASA TMX-3194 (Feb. 1975).

## 10.1 APPENDIX A - INLET SEPARATION CHARTS

A series of charts are presented in this appendix which permit the determination of the incidence angle for inlet lip separation. These charts are intended for initial preliminary design when exercise of the VAPE program would be premature.

The use of these charts is explained in the following discussion.

- (1) Select flight condition,  $M_\infty$ , and inlet geometry
- (2) Calculate desired inlet throat Mach number
- (3) Charts A-1 through A-3 or A-4 are then used to obtain the angle of incidence for lower lip inlet separation for the throat Mach number from (2) and the  $A_{HL}/A_{TH}$  from (1).
- (4) Chart A-5 is then used to find the incremental effect of varying inlet diameter ratio.
- (5) Chart A-6 is then used to find the incremental effect of varying the internal lip shape.
- (6) Chart A-7 is then used to find the incremental effect of varying the model scale of the configuration for diffuser separation effects.
- (7) If the model scale is such that the fan diameter is less than 6 inches, then chart A-8 is used to find a possible correction to be used for laminar separation location.

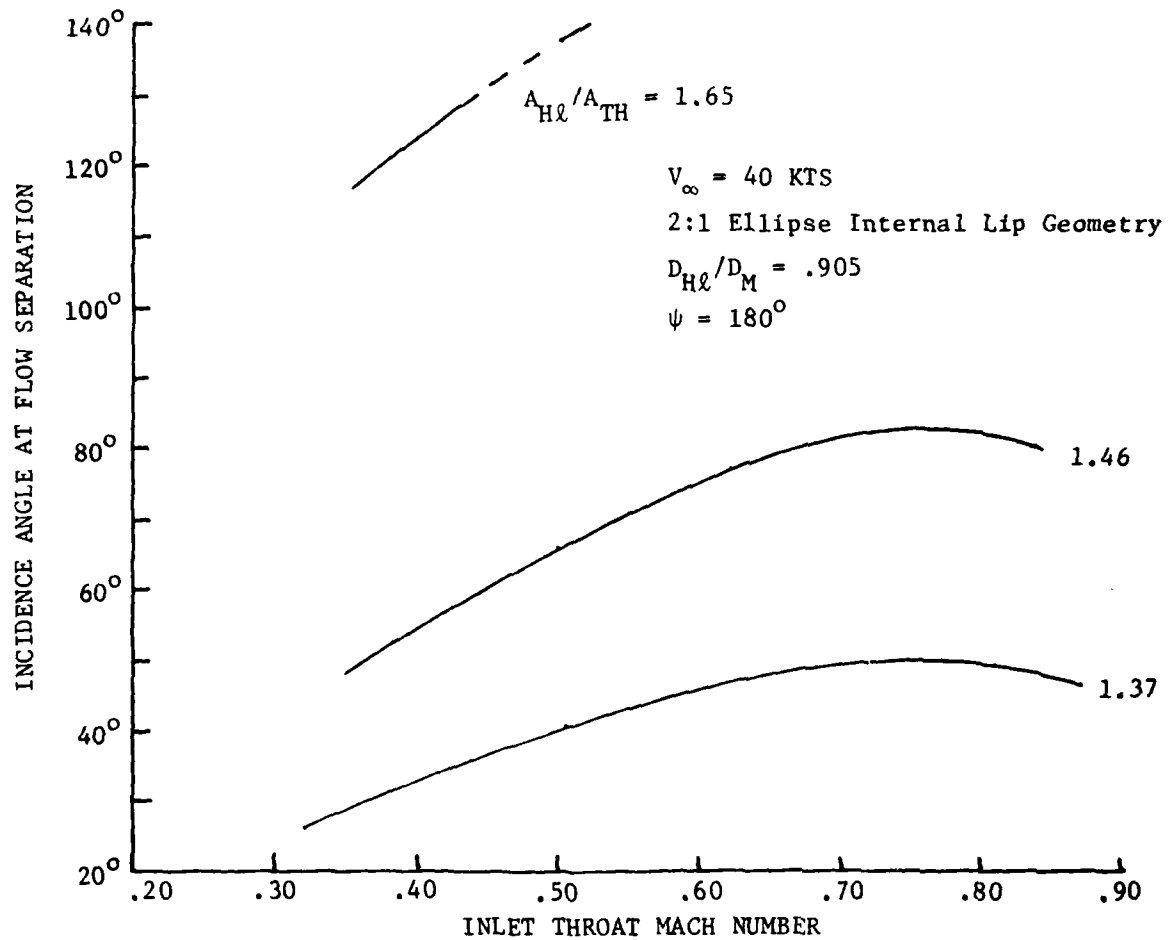


Figure A-1. Effect of Forward Speed and Inlet Contraction Ratio on Inlet Separation,  $V_{\infty} = 40 \text{ KTS}$

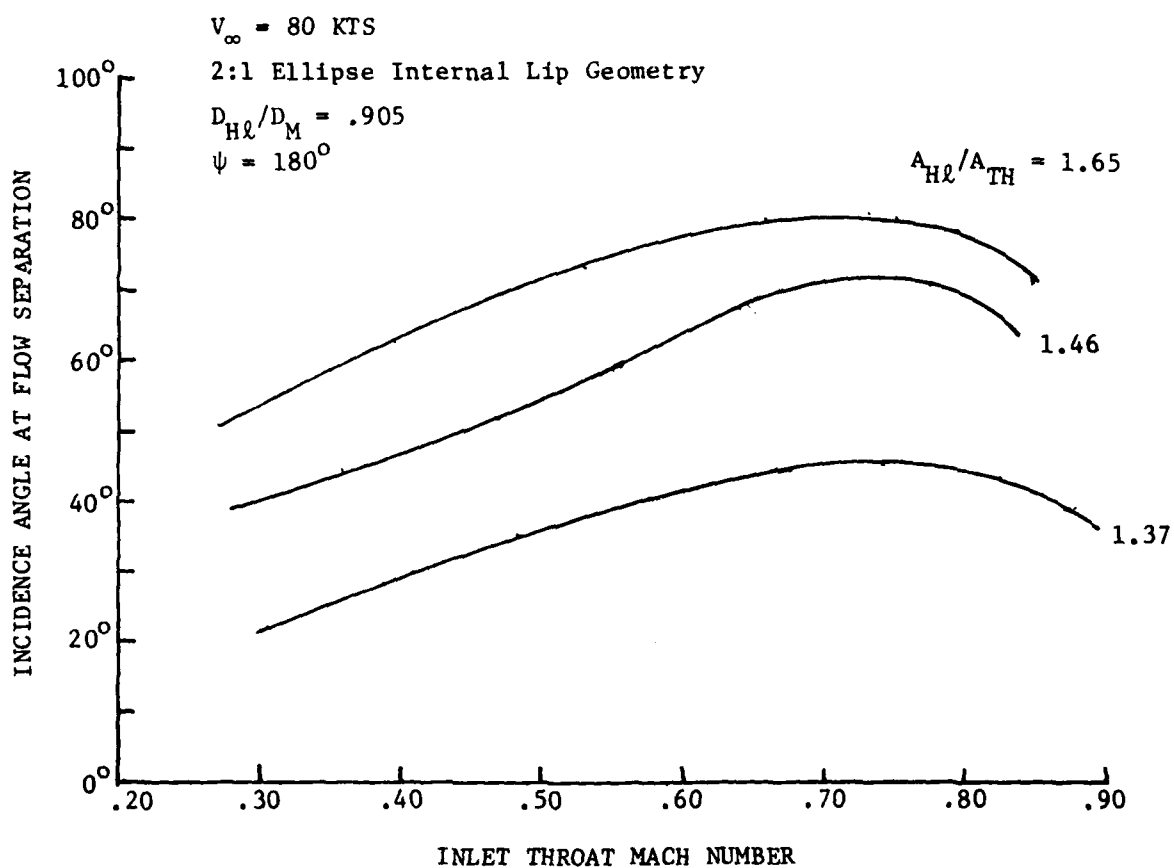


Figure A-2. Effect of Forward Speed and Inlet Contraction Ratio on Inlet Separation,  $V_{\infty} = 80$  KTS

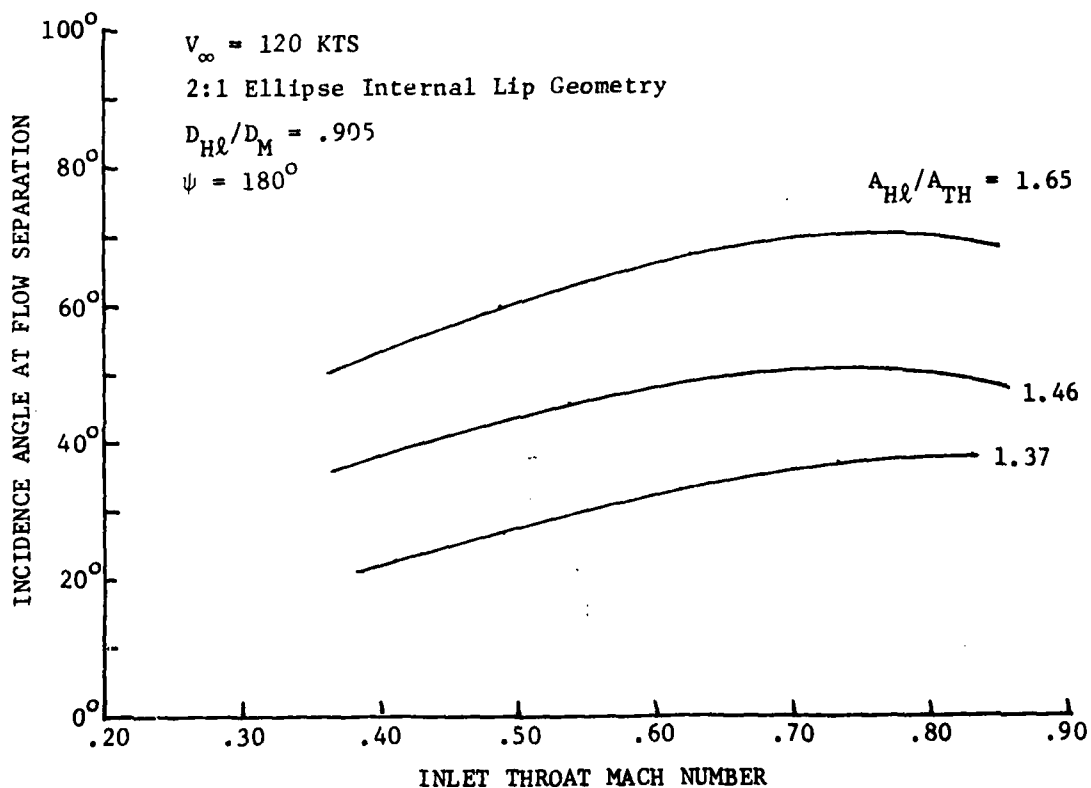


Figure A-3. Effect of Forward Speed and Inlet Contraction Ratio on Inlet Separation,  $V_{\infty} = 120$  KTS

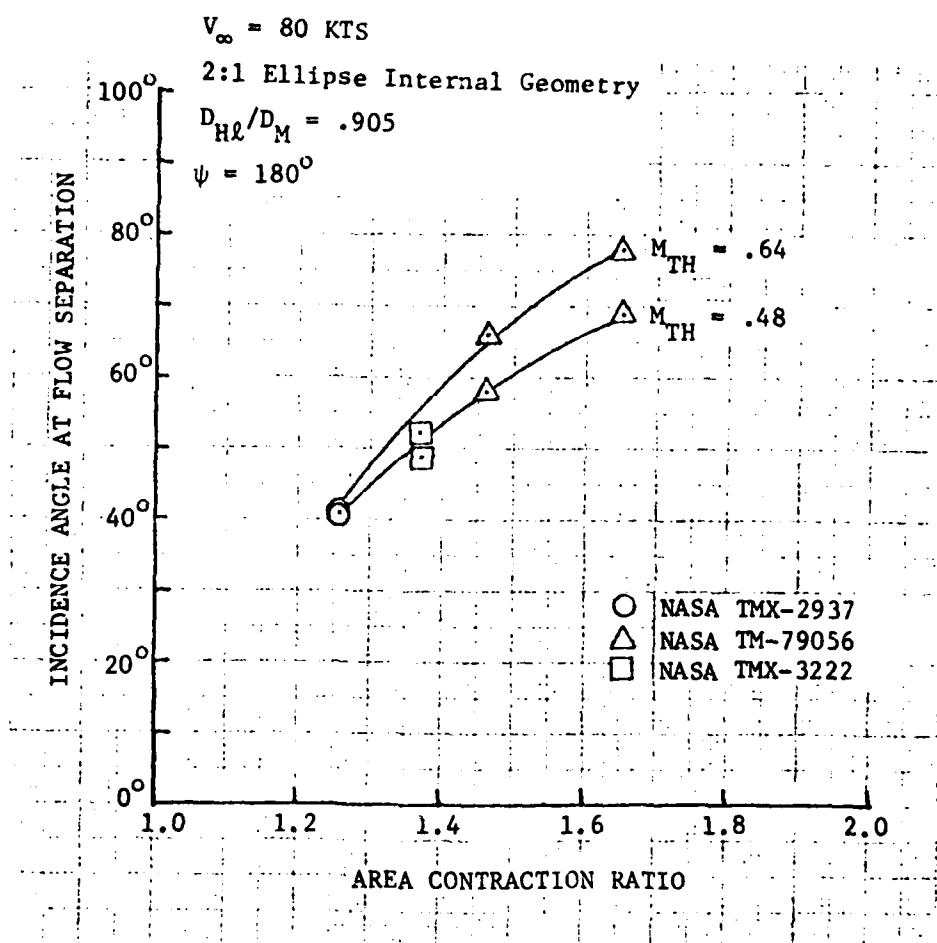


Figure A-4. Effect of Area Contraction Ratio and Throat Mach Number on Inlet Separation



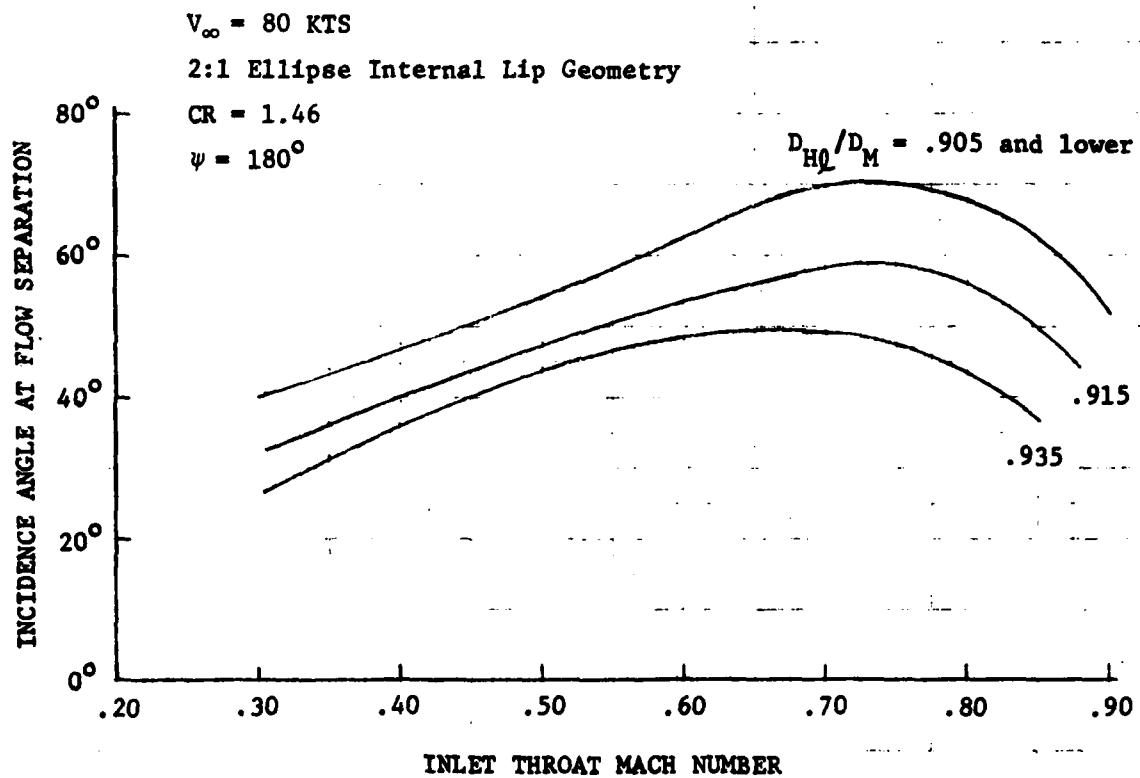


Figure A-5. Effect of Diameter Ratio on Inlet Separation.

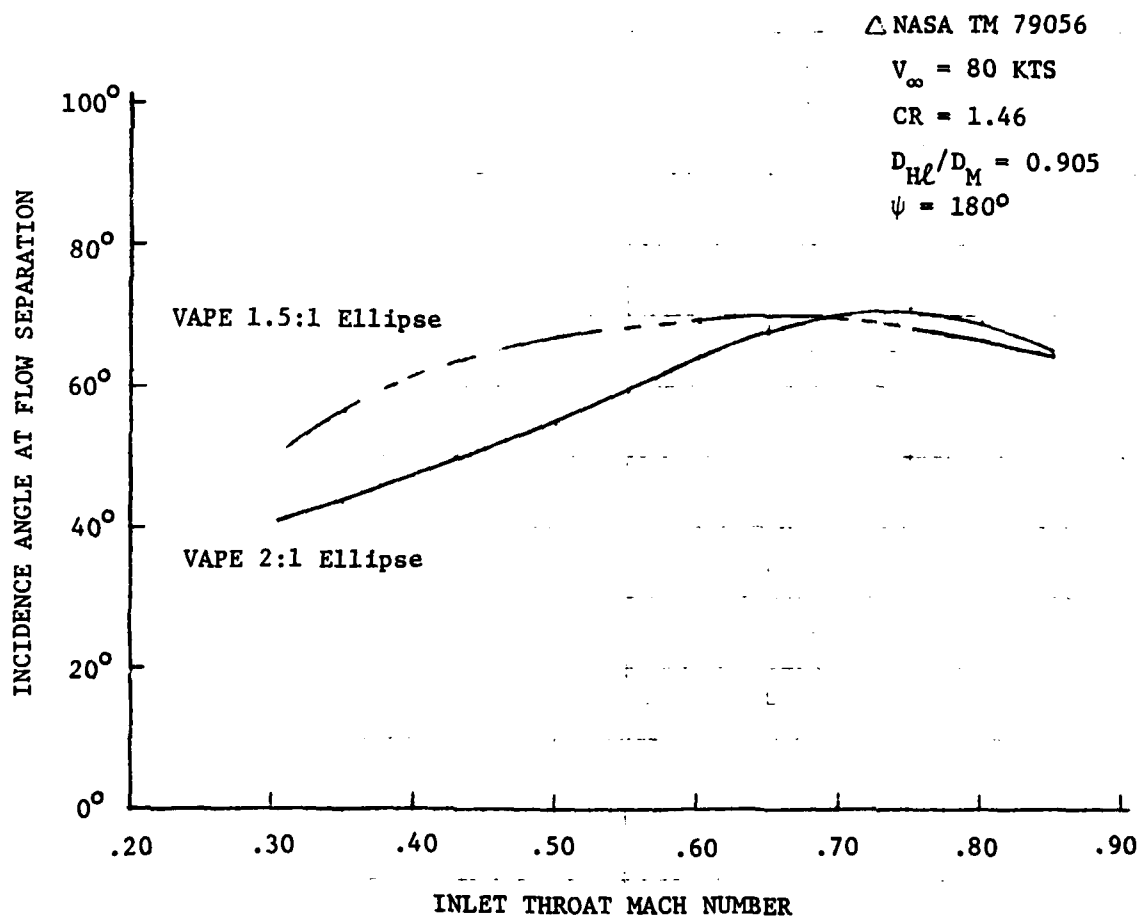


Figure A-6. Effect of Internal Lip Shape on Inlet Separation

$$D_{HL}/D_M = .905$$

$$A_{HL}/A_{TH} = 1.46$$

$$V_\infty = 40 \text{ KTS}$$

2:1 Ellipse Internal Lip Shape

$$\psi = 180^\circ$$

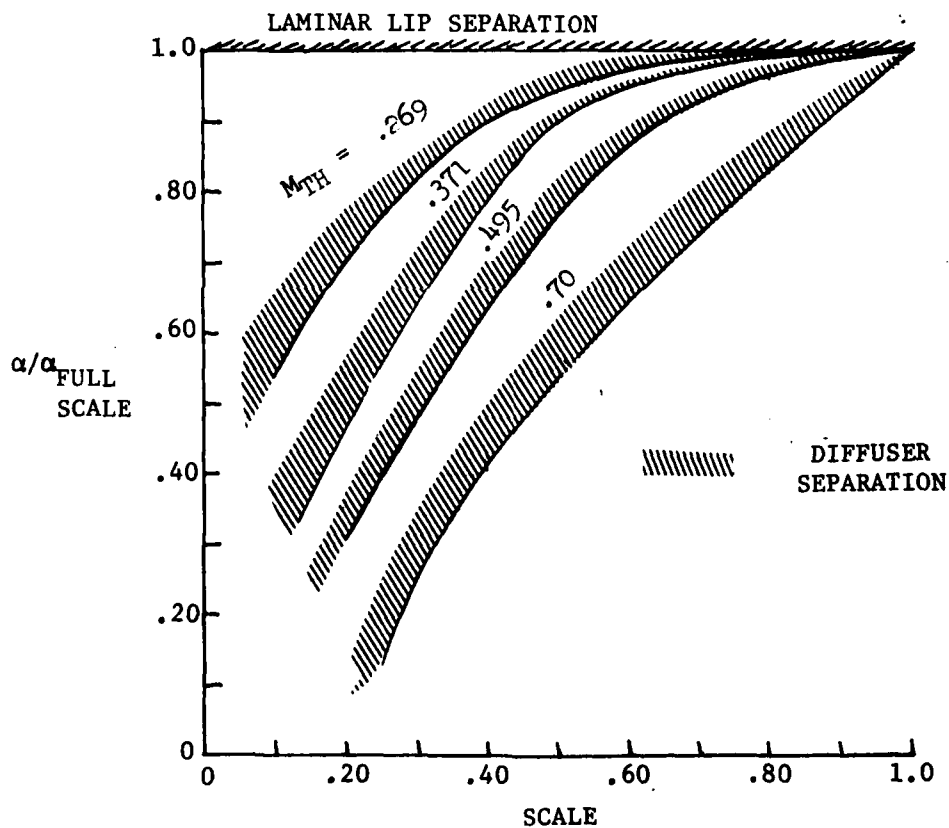
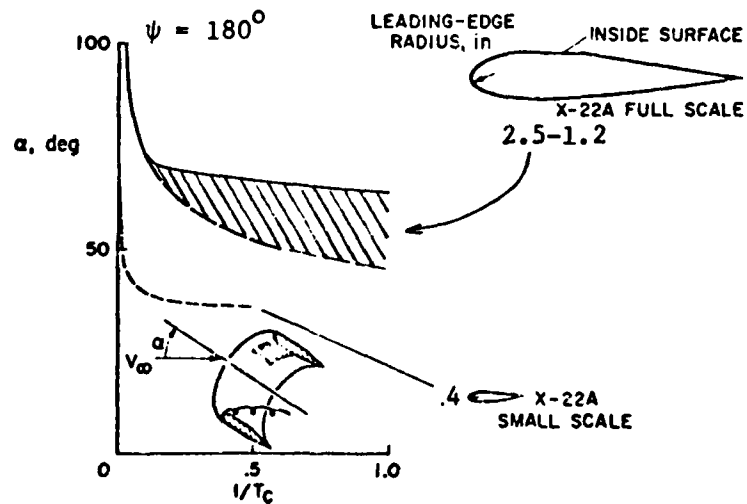


Figure A-7. Effect of Model Scale on Inlet Separation

INLET ANGLE OF ATTACK AT WHICH INNER  
LIP STALL OCCURS



(FROM NASA SP-116)

A-8. Effect of Model Scale on Angle of Attack  
for Laminar Lip Separation

## 10.2 APPENDIX B - RAM DRAG CHARTS

A series of charts are presented in this Appendix which permits the determination of the forces and moments acting on a V/STOL or conventional inlet. These charts are intended for preliminary design where exercise of the VAPE program would be premature.

The first figure, B-1, presents the axis systems used in these charts.

The use of the force and moment charts are described below.

- (1) Determine  $V / V_I$  where  $V_I$  = fan face velocity
- (2) Figures B-2 through B-4 are used to obtain the lift force, streamwise force and ram moment arm respectively.
- (3) Figure B-5 is used to obtain an incremental effect due to forward speed.
- (4) Figures B-7 and B-8 are used to obtain the effect of lip thickness on the inlet forces and moments. Figure B-6 indicates the amount of lip thickness variation represented in Figures B-7 and B-8.

Note: The force and moments are nondimensionalized by freestream and the capture area (area of the highlight).

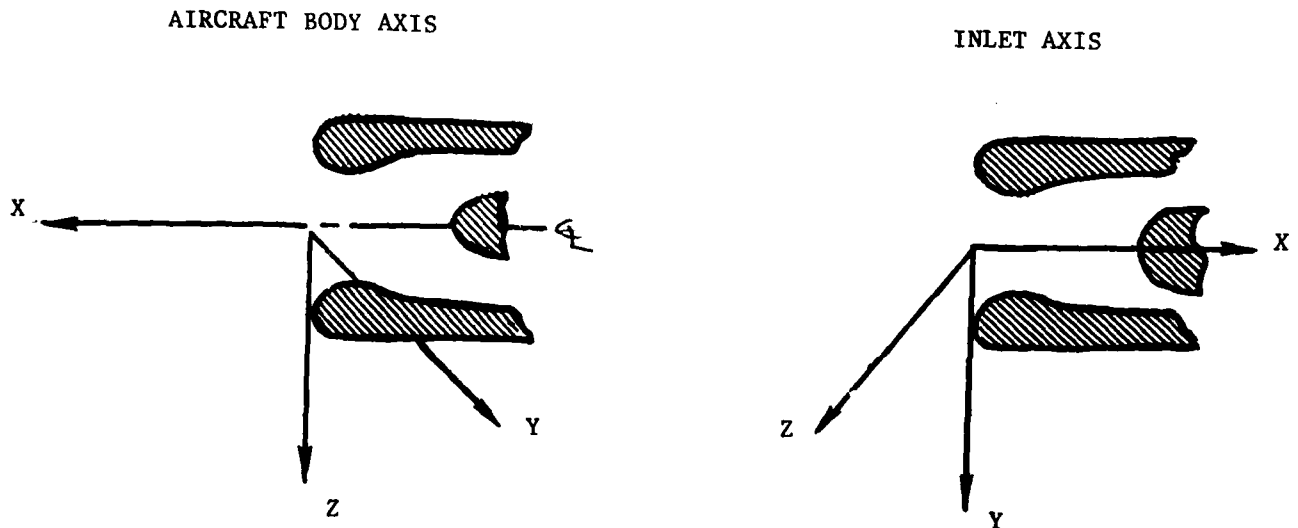


Figure B-1. Coordinate Axis Definition

46.10

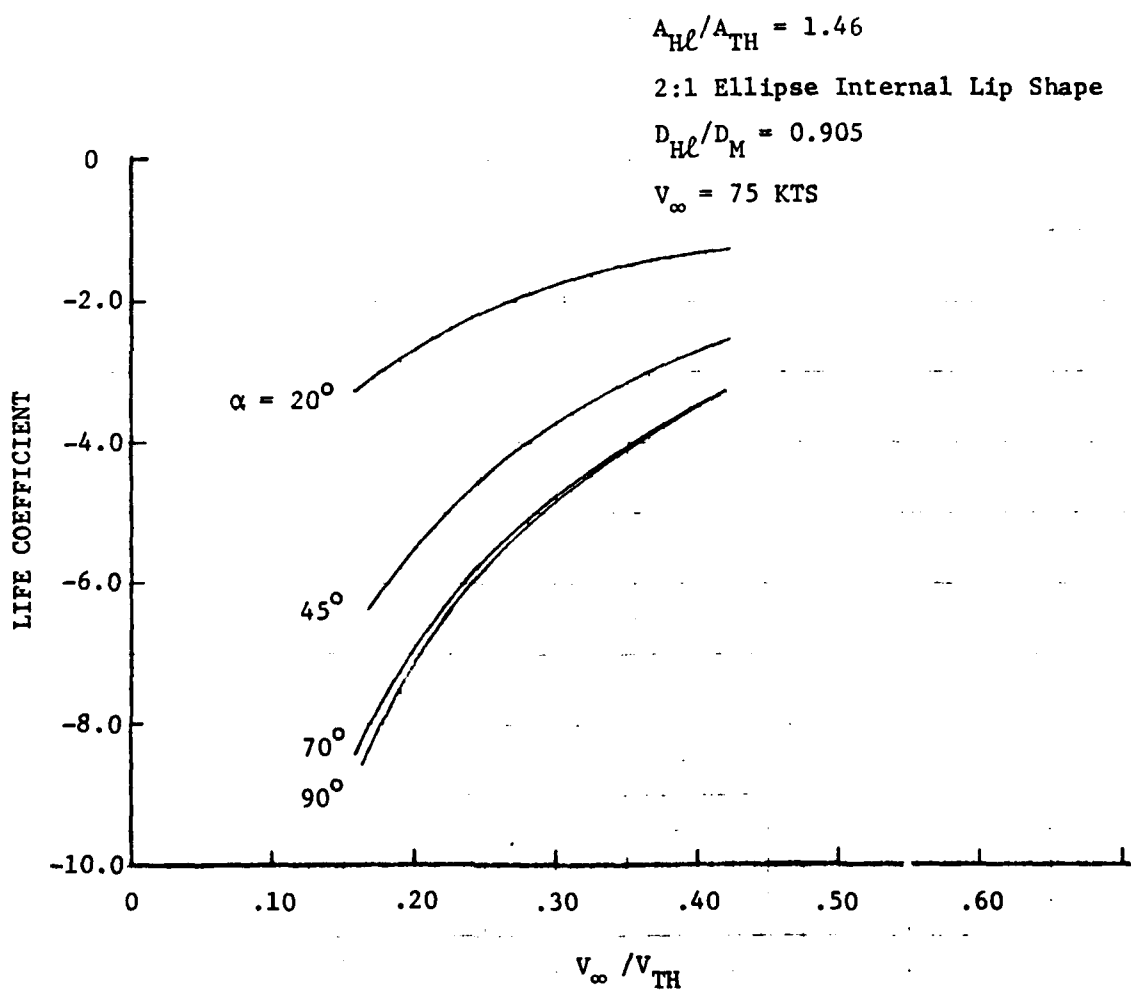


Figure B-2. Effect of Velocity Ratio on Inlet Lift

$$A_{HL}/A_{TH} = 1.46$$

2:1 Ellipse Internal Lip Shape

$$D_{HL}/D_M = 0.905$$

$$V_\infty = 75 \text{ KTS}$$

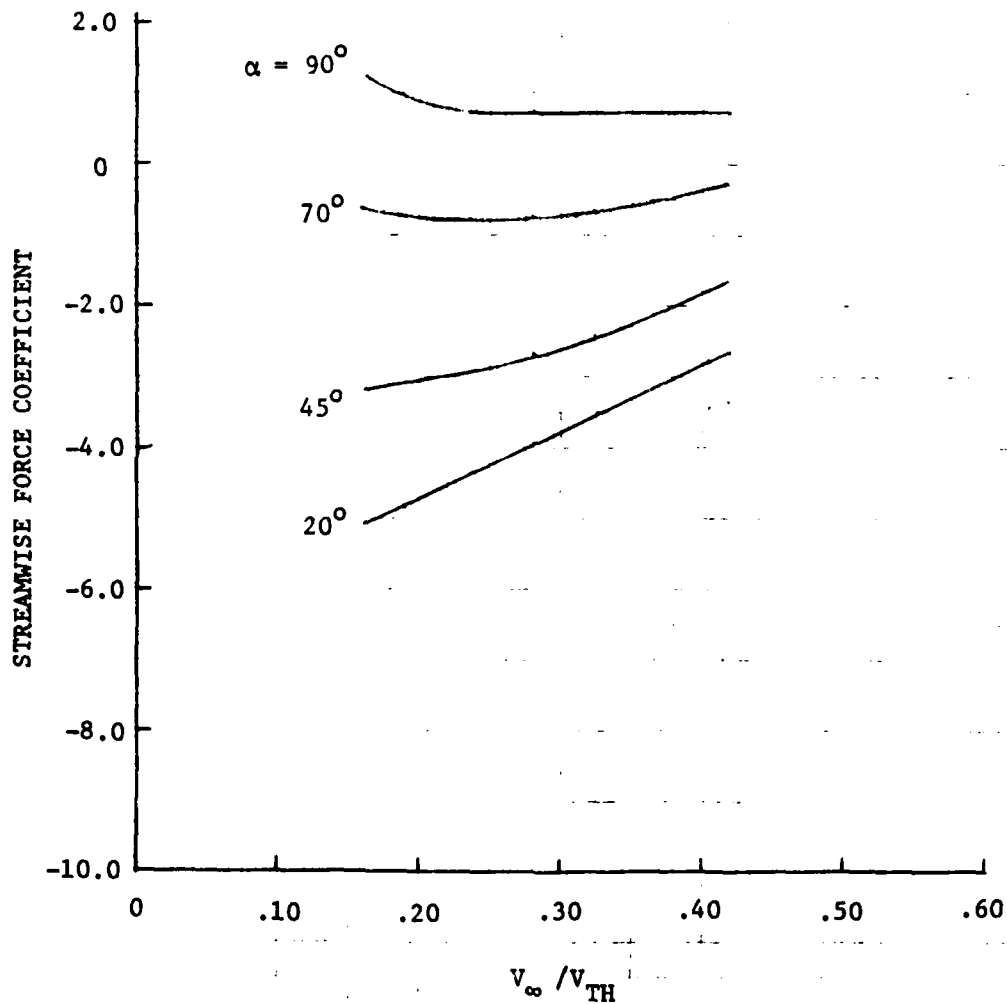


Figure B-3. Effect of Velocity Ratio on Inlet Streamwise Force

461510

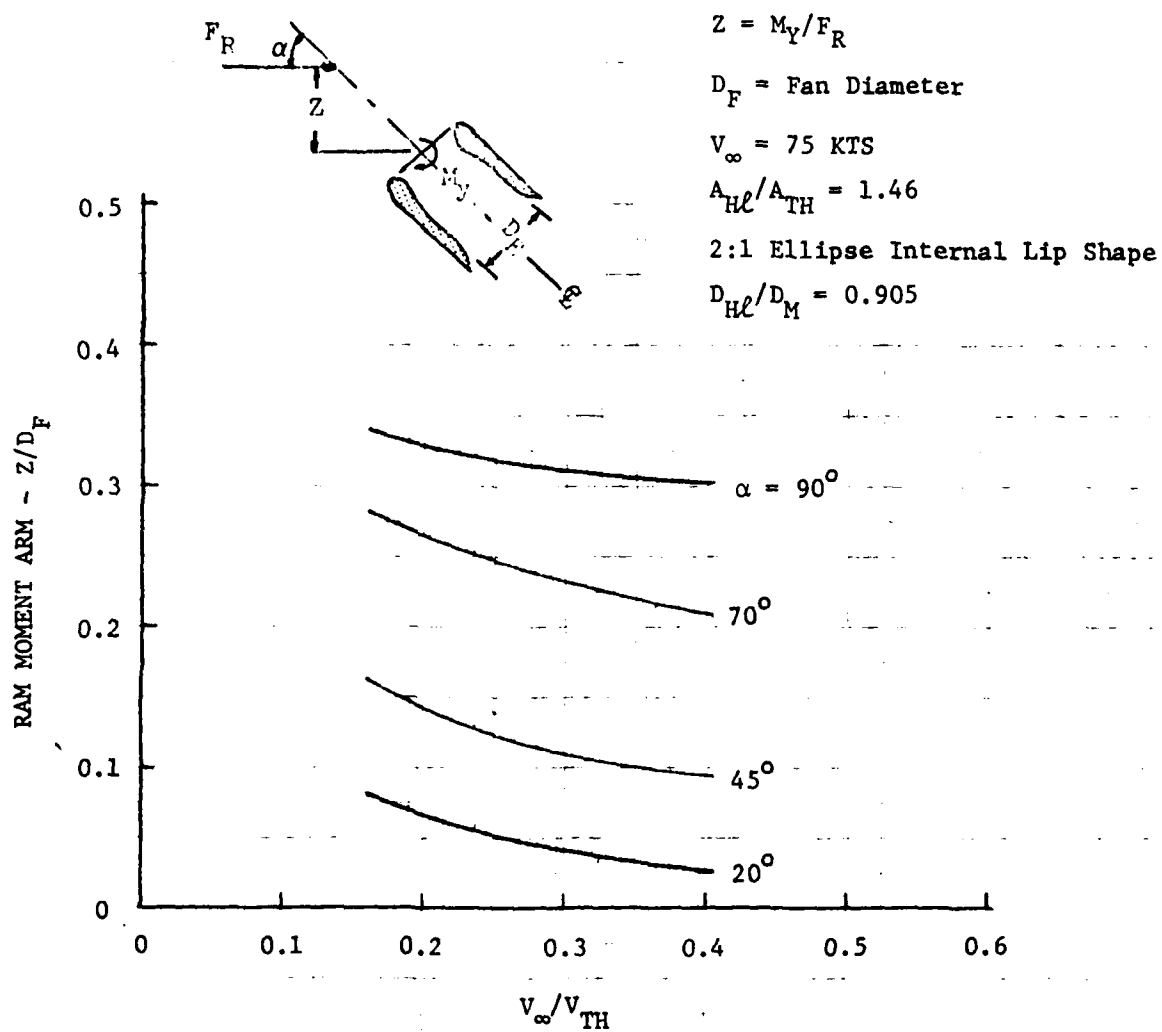


Figure B-4. Effect of Velocity Ratio on Inlet Moment Arm



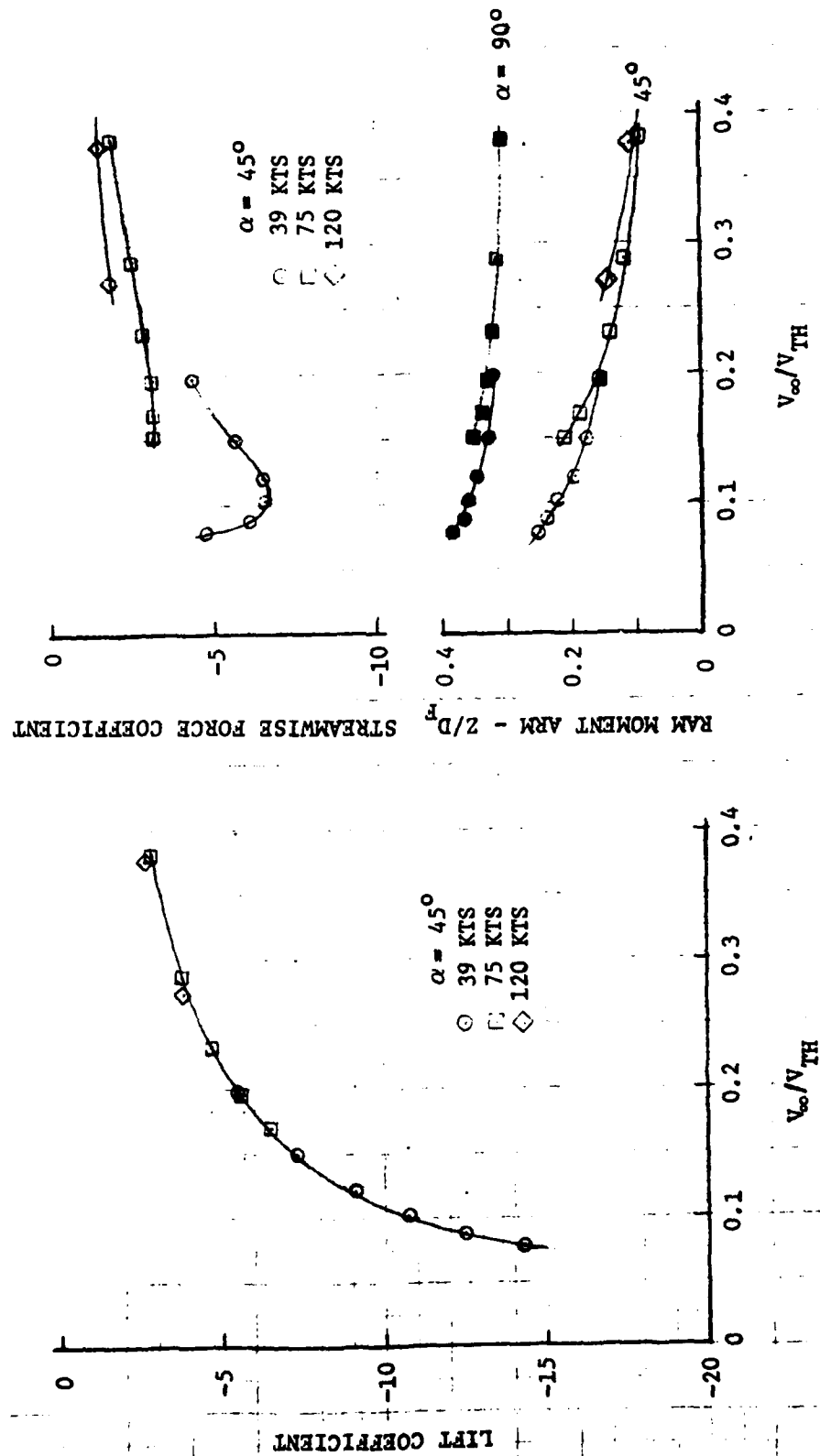


Figure B-5. Effect of Freestream Velocity on Inlet Forces and Moments

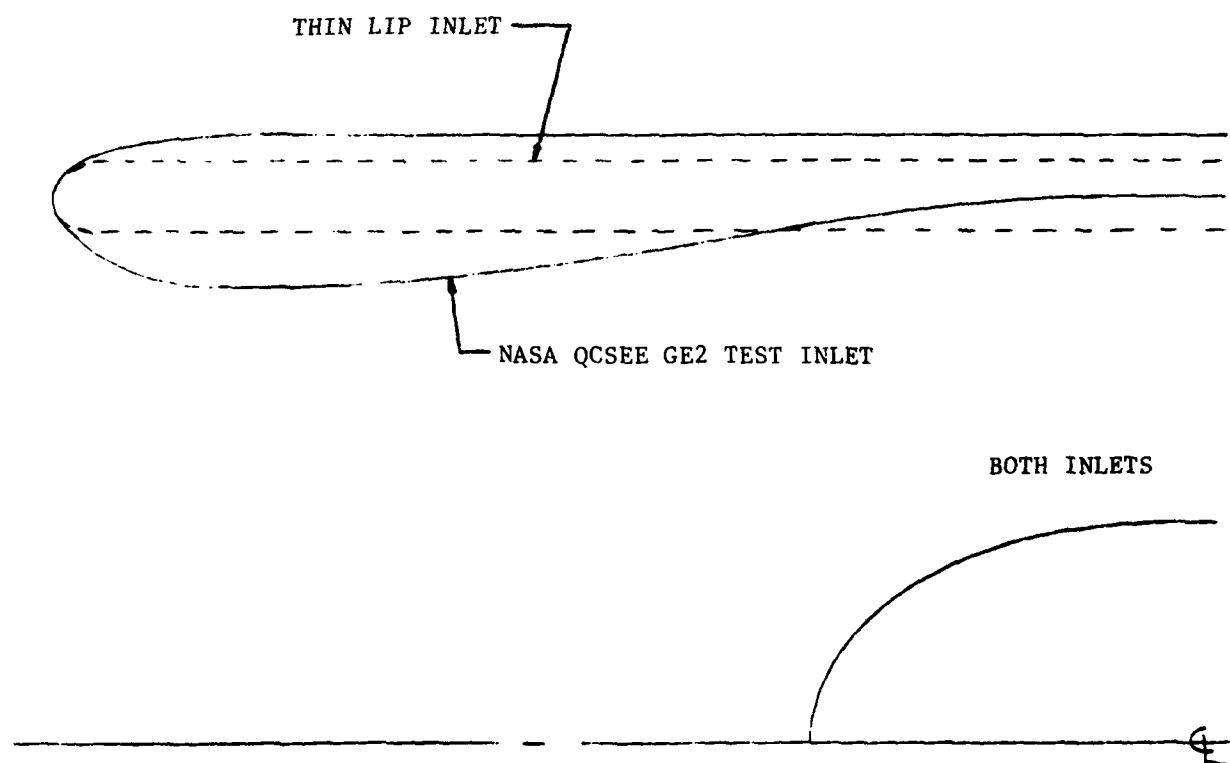


Figure B-6. Comparison of NASA QCSEE GE2 Inlet Geometry to a Thin Lip Inlet Geometry

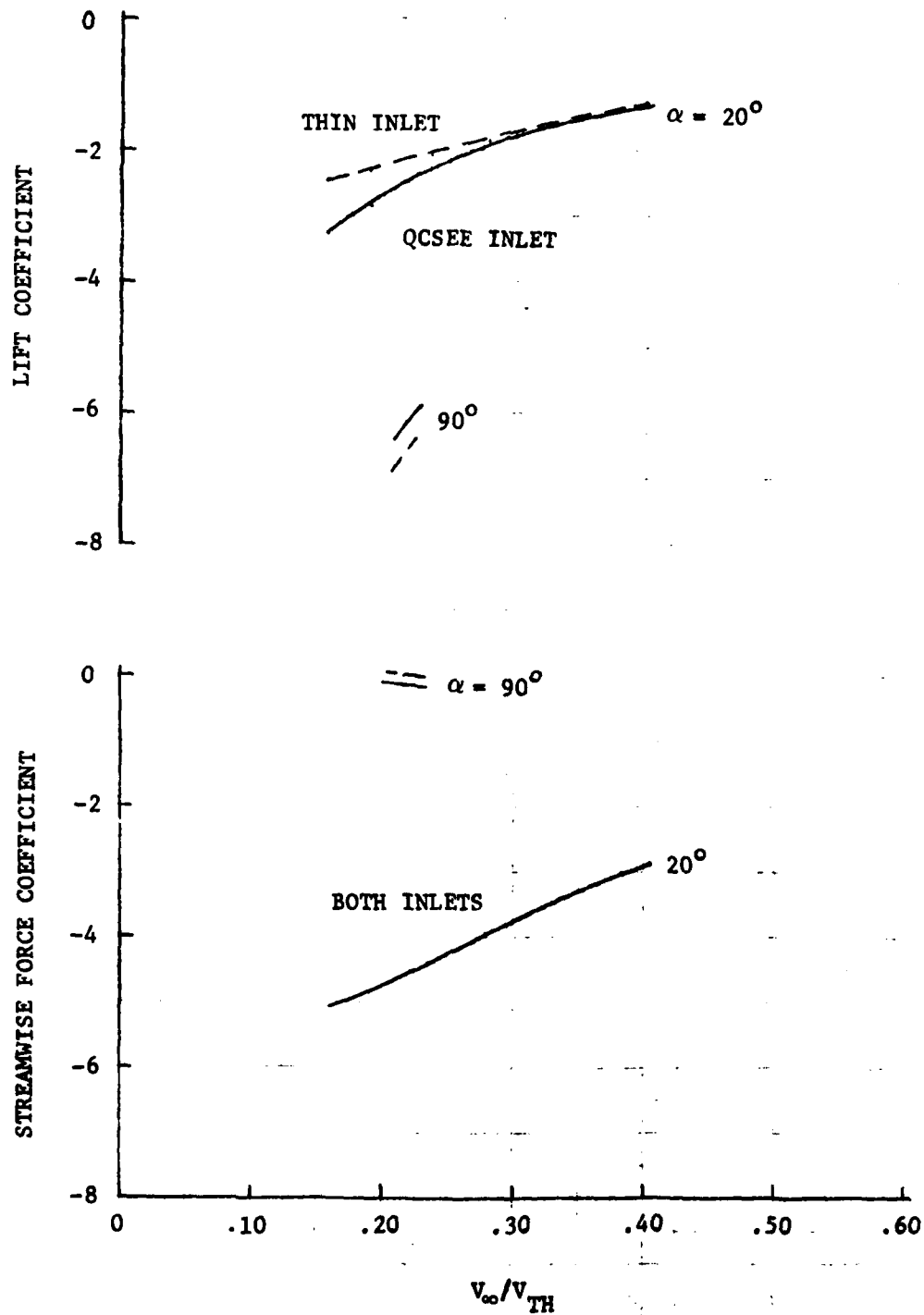


Figure B-7. Effect of Lip Shape on Inlet Force Components

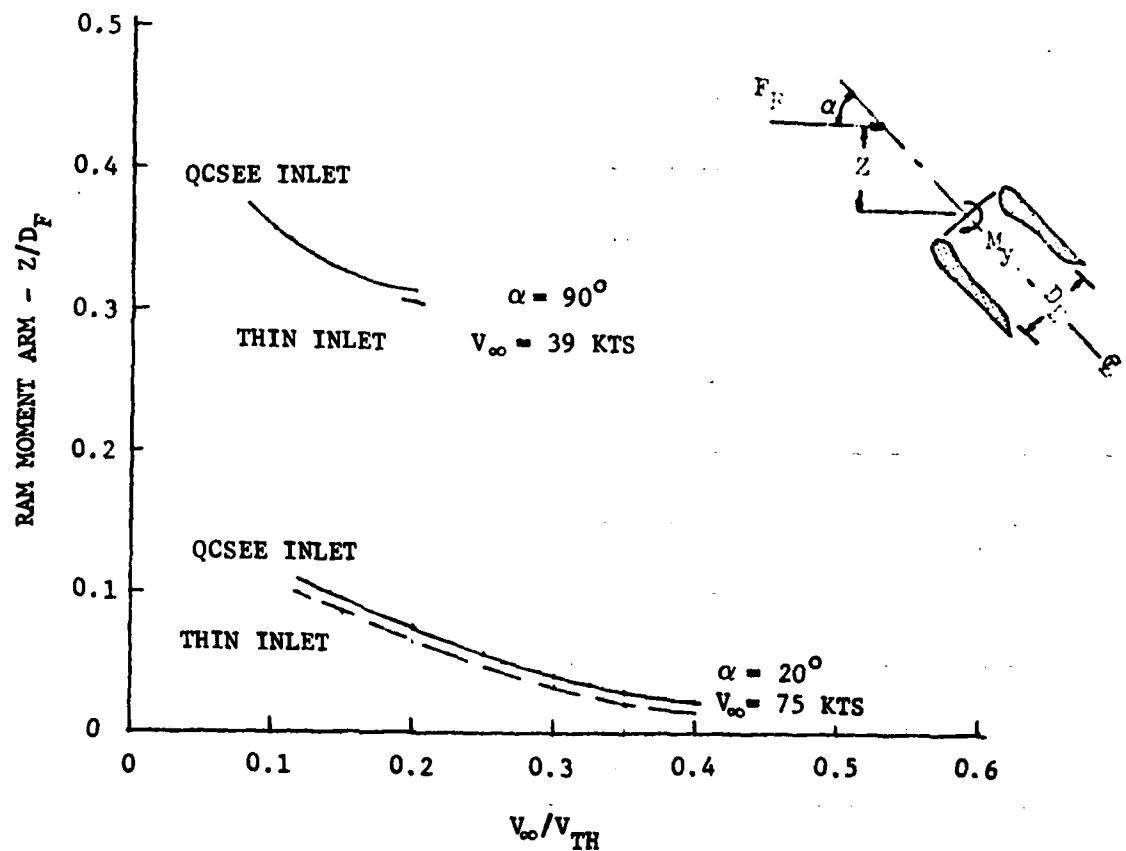


Figure B-8. Effect of Lip Shape on Inlet Ram Moment Arm.

## 10.3 APPENDIX C - SCOOP INLET EXPERIMENTAL DATA

The scoop inlet, Figure C-1, has been studied and tested as a candidate inlet for V/STOL aircraft due to its superior aerodynamic and acoustic performance during approach and takeoff.

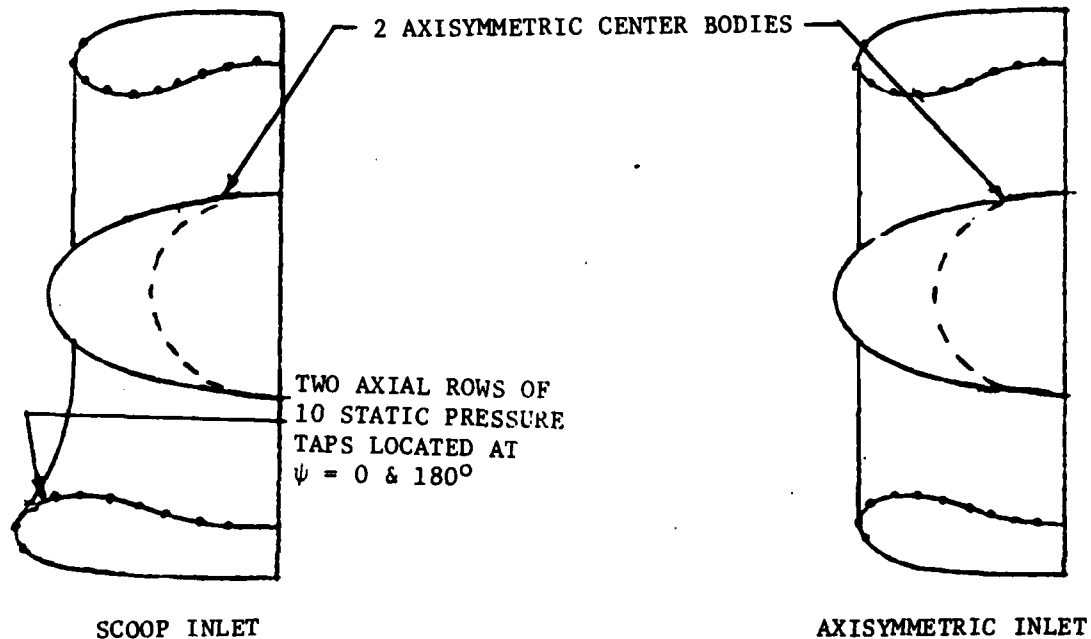


Figure C-1. Schematic of Scoop and Axisymmetric Inlet Configuration

During the Type "A" V/STOL studies, Vought and NASA Lewis Research Center tested two 12-inch inlet models in the 9 foot by 15 foot low speed wind tunnel at NASA Lewis. Over 500 data points were recorded for evaluation of the two Vought models. Test conditions simulated inlet operating conditions from static through transitional flight.

Table C-1 presents a data summary of the tests run at NASA Lewis. The results showed that the extended lower lip (scoop) inlet design had superior angle of attack performance during transition. At 80 KTS, for example, the scoop inlet could be pitched to over 61 degrees before any inlet separation could be observed, while the axisymmetric inlet separated at 42°. A comparison of scoop inlet to axisymmetric inlet performance at 0 and 80 KTS is presented in Figure A.2.

Although the angle of attack performance is better for the scoop inlet, Table C-2 shows that for this particular design, distortion level is higher and the inlet recovery is lower than found on the axisymmetric inlet. A

recovery level of 0.995 and distortion level of 0.005 were recorded at static conditions as compared to a recovery level of 0.983 and distortion level of 0.20 for the scoop inlet.

Figures C-3 through C-6 show inlet separation boundaries for the two inlets with two centerbody configurations at 35, 50, 80, and 120 KTS. In all cases tested, the effect of centerbody length and shape was of secondary effect. In addition, these tests indicated that the axisymmetric inlet was considerably better in crosswind than the scoop inlet, (90 degrees without internal flow separation as opposed to 25 degrees crosswind capability at 35 KTS).

FLIGHT CONDITION	SCOOP 2.0:1 C/B	SCOOP 1.5:1 C/B	AXI 2.0:1 C/B	AXI 1.5:1 C/B
Static, $M_T = .5$	① ② .983/.20	.980/.20	.995/.005	.995/.005
$V_0 = 35$ Kts, $M_T = .5$	.999/.12 123° ③	.992/.14 110°	.996/.005 90°	.995/.005 86°
$V_0 = 50$ Kts, $M_T = .5$	No Data	75.5°	47°	No Data
$V_0 = 80$ Kts, $M_T = .5$	.995/.015 61.5°	.995/.022 56°	.996/.005 42.5°	.995/.005 42.5°
$V_0 = 120$ Kts, $M_T = .5$	.996/.005 43.5°	.995/.006 40°	.996/.002 35°	.996/.006 34°
$V_0 = 140$ Kts, $M_T = .5$	No Data	No Data	No Data	.996/.006 31.5°
$V_0 = 35$ Kts, $M_T = .5$ Cross Wind	.986/.215 25° ④	No Data	.996/.005 90°	.995/.005 86°

- ① Total pressure recovery:  $\alpha \psi = 0$  degrees    ③ Inlet  $\alpha$  at Separation:  $\psi = 0$  degrees  
 ② Total pressure distortion:  $\alpha \psi = 0$  degrees    ④ Inlet  $\psi$  at separation:  $\alpha = 0$  degrees

Table C-1 Data Summary Tandem Fan Front Inlet  
 NASA LEWIS Test, 9' X 15' tunnel

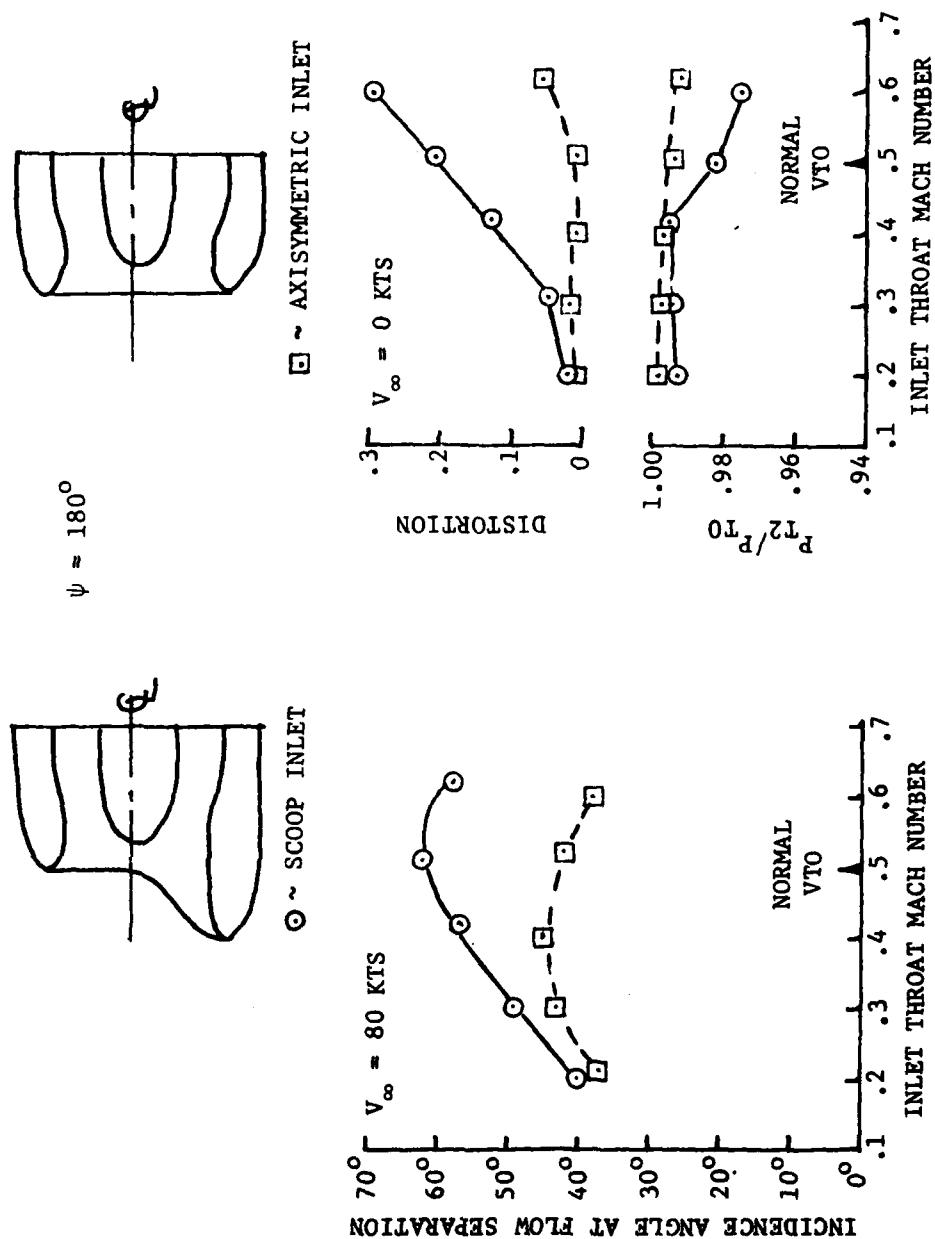


Figure C-2. Front Inlet Test Results



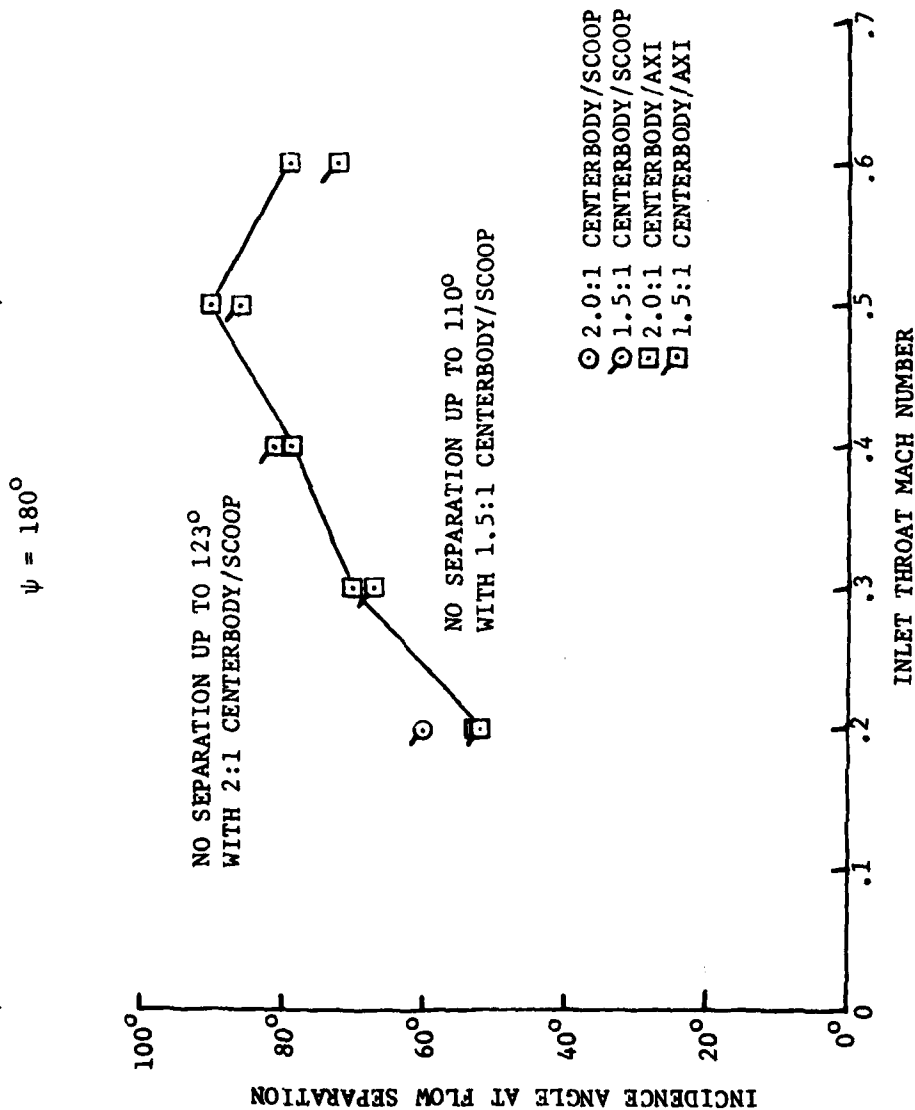
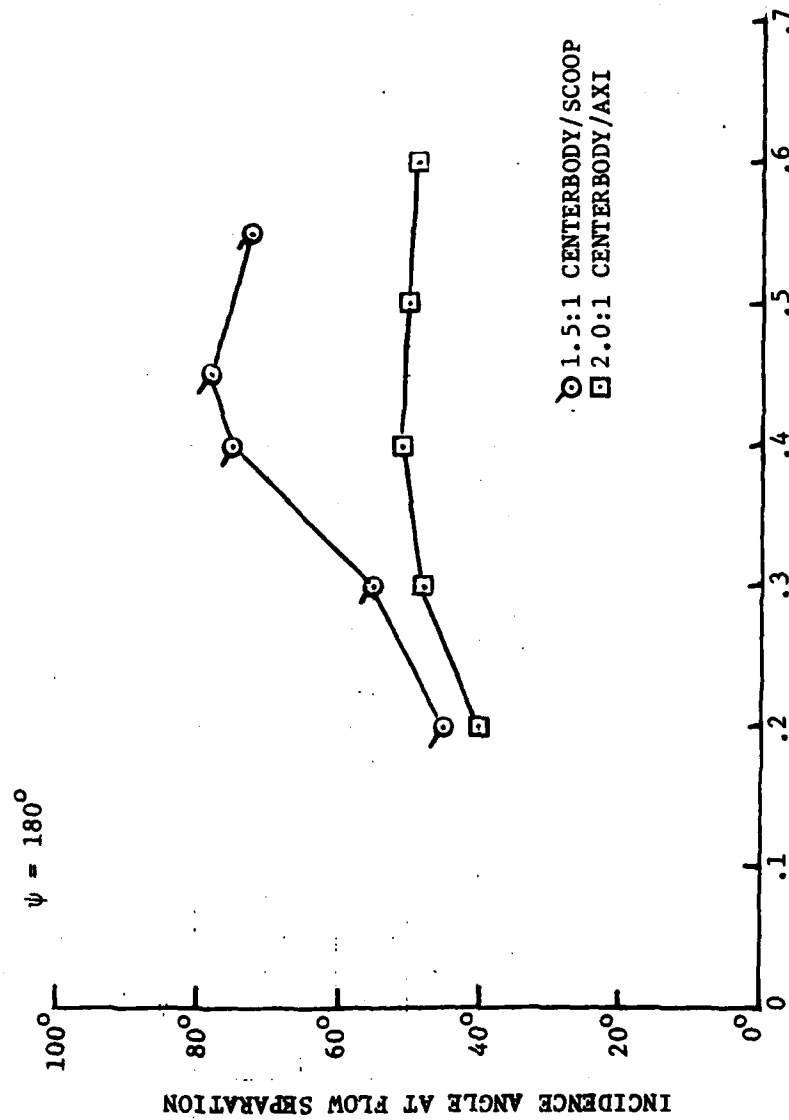


Figure C-3. Comparison of Axisymmetric Inlet and Scoop Inlet Separation Boundaries at 35 Knots



INLET THROAT MACH NUMBER  
 Figure C-4 Comparison of Axisymmetric Inlet and Scoop Inlet Separation Boundaries at 50 Knots

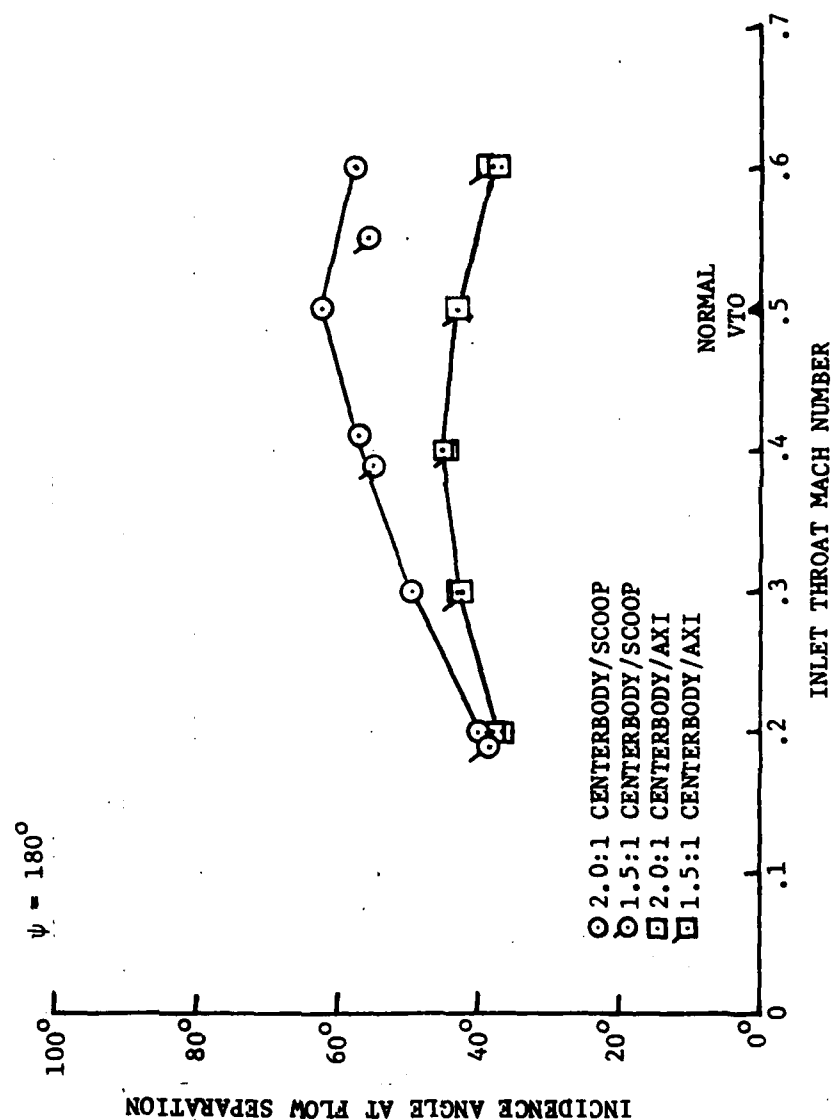


Figure C-5 Comparison of Axisymmetric Inlet and Scoop Inlet Separation Boundaries at 80 Knots

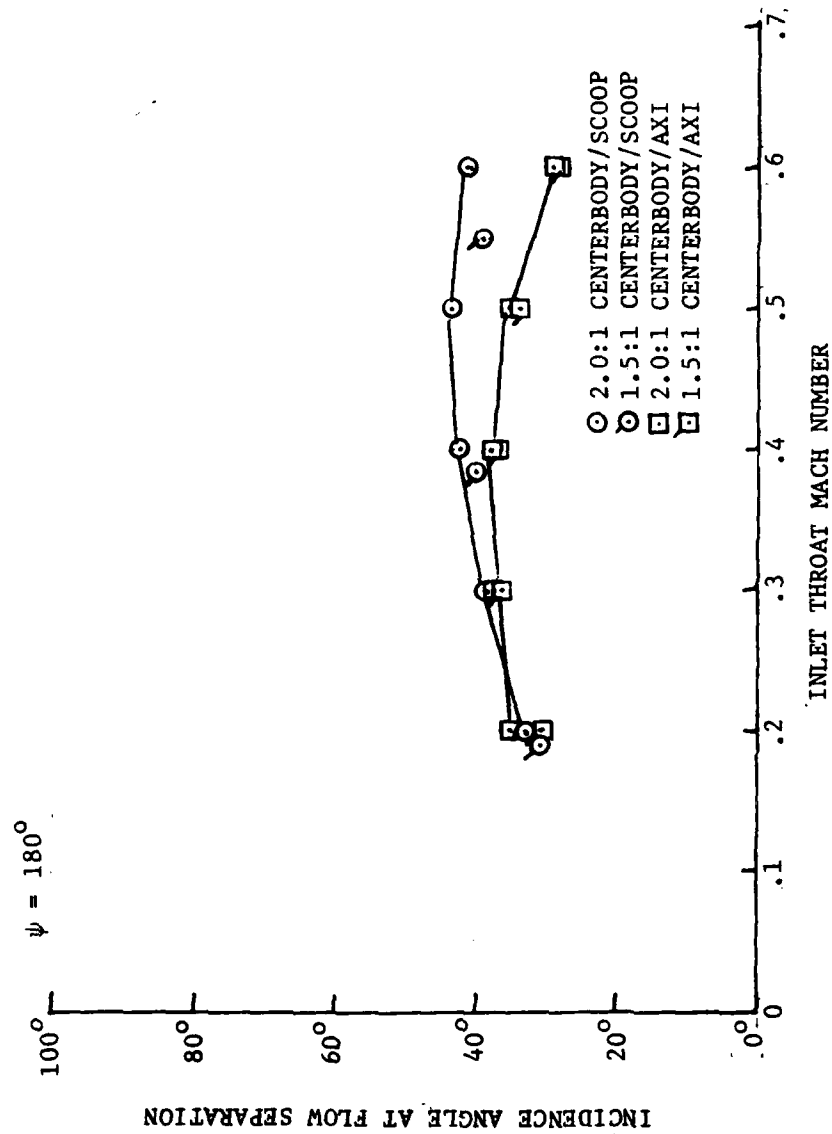


Figure C-6 Comparison of Axisymmetric Inlet and Scoop Inlet Separation Boundaries at 120 Knots

DISTRIBUTION LIST

Commander  
Naval Weapons Center  
China Lake, CA 93555

Commanding Officer  
Naval Air Propulsion Center  
Trenton, NJ 08628

Commander  
Naval Air Test Center  
Patuxent River, MD 20670

Commander  
David Taylor Naval Ship Research  
& Development Center  
Bethesda, MD 20034

Chief  
Office of Naval Research  
800 N. Quincy Street  
Arlington, VA 22217

Institute of Defense Analysis  
400 Army Navy Drive  
Arlington, VA 22202  
Attn: J. Attinello

Director  
National Aeronautics & Space  
Administration  
Ames Research Center  
Moffett Field, CA 94035  
Attn: D. Hickey

Director  
National Aeronautics & Space  
Administration  
Flight Research Center  
Edwards Air Force Base, CA 93523

National Aeronautics & Space  
Administration  
Langley Research Center  
Hampton, VA 23365

Director  
National Aeronautics & Space  
Administration  
Lewis Research Center  
21000 Brooke Park Road  
Cleveland, OH 44135

Director  
Air Force Flight Dynamics Laboratory  
(ASD/ENFDH)  
Wright-Patterson Air Force Base  
Dayton, OH 45433

Commander  
Air Force Aeronautical Systems  
Division  
Wright-Patterson Air Force Base  
Dayton, OH 45433

Superintendent  
Naval Postgraduate School  
Monterey, CA 93940

Commanding Officer  
Army Aviation Systems Test Activity  
Edwards Air Force Base, CA 93523

Commanding General  
Army Aviation Systems Command  
St. Louis, MO 63102

Commander  
Naval Air Systems Command (AIR-954)  
Department of the Navy  
Washington, DC 20361

7 copies: (2) for retention  
(2) for AIR-320D  
(1) for AIR-5301  
(1) for PMA-257  
(1) for AIR-03PA)

DISTRIBUTION LIST (CONTINUED)

General Dynamics  
Convair Division  
P.O. Box 80986  
San Diego, CA 92138

McDonnell-Douglas Corporation  
P.O. Box 516  
St. Louis, MD 63166

Lockheed-California Company  
P.O. Box 551  
Burbank, CA 91503

The Boeing Company  
Seattle, WA 98101

LTV Aerospace Corporation  
Dallas, TX 75221

Rockwell International  
Columbus, OH 43216

General Dynamics  
P.O. Box 748  
FortWorth, TX 76101

Commander  
Air Force Flight Test Center  
Edwards Air Force Base, CA 93523

Administrator  
Defense Documentation Center for  
Scientific & Technical Information  
(DDC)  
Building #5, Cameron Station  
Alexandria, VA 22314  
(12 copies)

Office of Naval Research  
800 N. Quincy Street  
Arlington, VA 22214  
Attn: Dr. R. Whitehead

Commander  
Naval Air Development Center  
Warminster, PA 18974  
13 Copies: (3) for Code 813  
(10) for Code 6053  
Attn: C. Henderson

McDonnell-Douglas Corporation  
3855 Lakewood Boulevard  
Long Beach, CA 90808

Pratt & Whitney Aircraft Division  
Division of United Aircraft  
Corporation  
East Hartford, CT 06108

Northrop Corporation  
Hawthorne, CA 90250

Lockheed-Georgia Company  
Marietta, GA 30061

Grumman Aerospace Corporation  
Bethpage, Long Island, NY 11714

Rockwell International  
Los Angeles, CA 90053

Fairchild-Republic Corporation  
Farmingdale, Long Island, NY 11735

Royal Aeronautical Establishment  
Bedford, England  
Attn: A. Woodfield

General Dynamics Corporation  
Ft. Worth, TX 76108

Hughes Aircraft Company  
Culver City, CA 90230

DISTRIBUTION LIST (CONTINUED)

A. L. Byrnes  
Lockheed-California Company  
Burbank, CA 91520

W. G. Hill, Jr.  
Research Department, A-08-35  
Grumman Aerospace Corporation  
Bethpage, NY 11714

R. J. Kita  
Grumman Aerospace Corporation  
Bethpage, NY 11714

D. Koenig  
Mail Stop 247-1  
NASA Ames Research Center  
Moffett Field, CA 94035

D. R. Kotansky  
Section Chief, Aerodynamics  
McDonnell Douglas Corporation  
McDonnell Aircraft Company  
P.O. Box 516  
St. Louis, MO 63166

P. T. Wooler  
Aerosciences Research  
Department 3811, Zone 82  
Northrop Corporation, Aircraft  
Group  
3901 W. Broadway  
Hawthorne, CA 90250

R. Whitehead  
Office of Naval Research  
Department of the Navy  
800 N. Quincey Street  
Arlington, VA 22217

E. D. Spong  
Branch Chief, Propulsion  
Dept. 343, Bldg. 32/2  
McDonnell Aircraft Company  
P.O. Box 516  
St. Louis, MO 63166

J. W. Paulson, Jr.  
Mail Stop 286  
NASA Langley Research Center  
Hampton, VA 23665

S. Perkins  
Nielsen Engineering & Research Inc.  
510 Clyde Avenue  
Mountain View, CA 94043

R. Perkins  
Deputy Chief V/STOL Project Office  
Naval Air Systems Command  
Washington, DC 20361

M. F. Platzer  
Code 67P1  
Department of Aeronautics  
Naval Postgraduate School  
Monterey, CA 93940

D. B. Schoelerman  
Vought Corporation  
P.O. Box 5907  
Dallas, TX 75222

C. J. Martin  
David W. Taylor Naval Ship Research  
and Development Center  
Bethesda, MD 20014